Univerzita Karlova v Praze

1. lékařská fakulta

Studijní program: Lékařská biofyzika

Mgr. Dita Wagnerová

Korelace mezi kvantitativními in vivo MR parametry v různých tkáních (MR spektroskopické zobrazování, MR difúzometrie, MR relaxometrie aj.)

Correlation between Quantitative MR Parameters in Various Tissues In Vivo (MR Spectroscopic Imaging, MR Diffusometry, MR Relaxometry)

Disertační práce

Školitel: Ing. Milan Hájek, DrSc.

Praha, 2012

Charles University in Prague

The First Faculty of Medicine

Study Programme: Medical Biophysics

Mgr. Dita Wagnerová

Correlation between Quantitative MR Parameters in Various Tissues In Vivo (MR Spectroscopic Imaging, MR Diffusometry, MR Relaxometry)

Korelace mezi kvantitativními in vivo MR parametry v různých tkáních (MR spektroskopické zobrazování, MR difúzometrie, MR relaxometrie aj.)

Doctoral Thesis

Thesis Supervisor: Ing. Milan Hájek, DrSc.

Prague, 2012

Prohlášení:

Prohlašuji, že jsem závěrečnou práci zpracovala samostatně a že jsem řádně uvedla a citovala všechny použité prameny a literaturu. Současně prohlašuji, že práce nebyla využita k získání jiného nebo stejného titulu.

Nesouhlasím s trvalým uložením elektronické verze mé práce v databázi systému meziuniverzitního projektu Theses.cz za účelem soustavné kontroly podobnosti kvalifikačních prací.

V Praze, 20.12. 2012

Dita Wagnerová

Identifikační záznam:

WAGNEROVÁ, DITA. *Korelace mezi kvantitativními in vivo MR parametry v různých tkáních (MR spektroskopické zobrazování, MR difúzometrie, MR relaxometrie aj.). [Correlation between in vivo quantitative MR parameters in various tissues (MR spectroscopic imaging, MR diffusometry, MR relaxometry)]*. Praha, 2012. 96 s., 3 příl. Dizertační práce. Univerzita Karlova v Praze, 1. lékařská fakulta, Institut klinické a experimentální medicíny. Vedoucí práce Hájek, Milan.

Abstrakt

Koregistrace MR spektroskopických (SI), difúzních (DTI) a relaxačních obrazů a jejich následné korelace založené na kvantitativním zpracování obrazu bod po bodu mají potenciál rozlišit patologické stavy a zdravou tkáň, a pomoci tak stanovit rozsah patologie. Použití této metody v klinické praxi bylo vyzkoušeno u pacientů s tumorem mozku a s temporální epilepsií (TLE).

30 pacientů s nově diagnostikovanou lézí, 22 pacientů s léčeným tumorem (diagnóza stanovena na základě histologie či radiologickým sledováním), 20 pacientů s TLE a 59 zdravých dobrovolníků bylo vyšetřeno v magnetickém poli 3T. Vyšetřovací protokol obsahoval T2-vážené MR obrazy, SI, DTI a T2 relaxometrii. Korelace byly analyzovány programem CORIMA umožňující automatickou identifikaci oblasti zdravé tkáně dle kontrolních dat.

Mozkové léze: Specifické tvary korelací metabolitů, MD a T2 relaxačních časů (T2) byly nalezeny pro danou lokalizaci léze i pro daný typ tumoru. Tyto korelace vznikají v důsledku zastoupení různých typů tkání ve zkoumané oblasti. Korelační grafy rekurentních tumorů vykazovaly charakteristiku stejnou jako u tumorů neléčených, ale se změněnými hodnotami parametrů vlivem terapie. Metabolické hodnoty nekorelovaly s MD nebo T2 v případě radiační nekrózy.

TLE: V hipokampu v předozadním směru se MR parametry měnily postupně u všech subjektů, nicméně směrnice závislosti u pacientů statisticky významně překračovala hodnoty naměřené u kontrol.

Pro diferenciaci tkáně jsou vhodné korelace mezi následujícími parametry: MD, T2, cholin, kreatin, N-acetylaspartát, inositol, laktát, makromolekuly, lipidy a jejich poměry.

Kvantitativní zpracování různých MR obrazů umožňuje komplexně popsat vysoce heterogenní tkáň v patologii a jejím okolí a určit důležité parametry pro tkáňovou diferenciaci a stanovení rozsahu patologie.

Klíčová slova

1H MR spektroskopické zobrazování, MR difúzometrie, MR relaxometrie, Korelace, Tumor, Temporální epilepsie

Abstract

Coregistration of MR spectroscopic (SI), diffusion (DTI), relaxation images and their subsequent correlations based on pixel-by-pixel quantitative analysis have the potential to distinguish between pathological states and healthy tissue and therefore can help assessing brain pathology extent. Patients with brain tumours and temporal lobe epilepsy (TLE) were involved in the study to validate the use of this method in clinical practice.

30 patients with a new diagnosed brain lesion, 22 patients with a treated tumour (diagnosis assessed by histology or by radiological follow-up), 20 TLE patients and 59 healthy subjects were examined on a 3T system. The measurement protocol consisted of T2-weighted MR images, SI, DTI and T2 relaxometry. Correlations were analysed with the CORIMA programme with automatic identification of pixels in the normal tissue according to control data.

Brain lesions: Specific correlation patterns between metabolites, MD and T2 relaxation times (T2) were found for a given lesion localisation and tumour type. The patterns depend on different tissue states involved in the examined area. Recurrent tumours exhibited the same patterns as untreated ones but with changed parameter values caused by therapy. Metabolic values did not correlate with MD and T2 in radiation necrosis.

TLE: MR parameters gradually changed in anteroposterior direction of HC in all subjects; however, slopes in patients significantly exceeded those in controls.

Correlations of the following MR parameters are suitable for tissue differentiation: MD, T2, choline, N-acetylaspartate, creatine, inositol, lactate, macromolecules, lipids and their ratios.

A quantitative analysis of different MR methods is able to describe the complexity of a highly heterogeneous tissue in the pathology and its vicinity and determine crucial parameters for tissue differentiation and lesion extension.

Keywords

1H MR spectroscopic imaging, MR diffusometry, MR relaxometry, Correlations, Tumour, Temporal lobe epilepsy

The doctoral thesis was prepared at the Department of Diagnostic and Interventional Radiology in Institute for Clinical and Experimental Medicine in Prague as a part of a doctoral study of the Medical Biophysics study programme at the First Faculty of Medicine of Charles University in Prague.

Mgr. Dita Wagnerová

MR Unit
Department of Diagnostic and Interventional Radiology
Institute for Clinical and Experimental Medicine

Vídeňská 1958/9
14021 Prague 4
Czech Republic

E-mail: diwa@medicon.cz, wagnerova.dita@centrum.cz

Study Programme Board: 11 – Medical Biophysics
Thesis Supervisor: Ing. Milan Hájek, DrSc.

Prague, December 20, 2012

Acknowledgement

I am very thankful to my advisor Dr. Milan Hájek for his helpful advice and support in various aspects throughout my entire PhD study.
I would especially like to thank Dr. Filip Jírů and Dr. Vít Herynek for their tireless help, patience, friendships, optimism and the constant supply of biscuits during my whole study.
Also, many thanks to my co-workers Dr. Monika Dezortová, Dr. Antonín Škoch, Dr. Ibrahim Ibrahim, Dr. Daniel Jirák, Dr. Martin Burian and Jaroslav Tintěra for their inspiring advice and technical support.
I would also like to thank Dr. Bernardo Celda Muňoz, Dr. Luis Martí-Bonmatí and Dr. Milan Hájek for giving me the opportunity of the research fellowships in Valencia. Addditionally, many thanks to Dr. Ángel Alberich-Bayarri, Dr. Gracián García Martí, Dr. Roberto Sanz Requena, Dr. M.Beatriz Martínez-Granados and Dr. Eva Piñero for their friendships enabling me to discover beauties of the spanish language and culture.
Last, but not least, I would like to thank my parents and friends for their encouragement and overall support in various aspects.

These studies were supported by the grant projects VZ MZ0IKEM2005, MSMTCR LC554, the EC FP6 project Angiotargeting (504743), IGA MZCR NS/9654-4, MSM0021620849, IGA MZCR NS 9915-4/2008, VZ MZ0FNM2005-6504 and by the grant project (Ministry of Health, Czech Republic) for development of research organization 00023001 (IKEM, Prague, Czech Republic) – Institutional support.

Contents

List of Abbreviations

ADC, apparent diffusion coefficient;

Cho, choline-containing compounds;

CPMG, Carr-Purcell-Meiboom-Gill sequence;

Cr, total creatine;

CSA, chemical shift artefact;

CSF, cerebrospinal fluid;

DTI, diffusion tensor imaging;

EEG, electroencephalography;

EZ, epileptogenic zone;

FA, fractional anisotropy;

FCD, focal cortical dysplasia;

FDG-PET, 2-fluorodeoxy-D-glucose positron emission tomography;

FOV, field of view;

GABA, γ-aminobutyric acid;

GM, gray matter;

HC, hippocampus;

HS, hippocampal sclerosis;

Ins, myo-inositol;

MCD, malformation of cortical development;

MD, mean diffusivity;

MPRAGE, magnetization prepared rapid acquired gradient echo;

MR, magnetic resonance;

MRI, magnetic resonance imaging;

MRS, magnetic resonance spectroscopy;

MRSI, SI, 1H MR spectroscopic imaging;

MTLE, mesial temporal lobe epilepsy;

NA, number of acquisition;

NAA, N-acetylaspartate;

PRESS, point resolved spectroscopy;

ROI, region of interest;

SNR, signal-to-noise ratio

ST, slice thickness;

SVS, single voxel spectroscopy;

T1W, T1-weighted image;

T2W, T2-weighted image;

T1, T1 relaxation time;

T2, T2 relaxation time;

TE, echo time;

TLE, temporal lobe epilepsy;

TR, repetition time;

VOI, volume of interest;

WM, white matter;

1 Introduction

Progress in computer technology progress has enabled the significant development of new diagnostic methods in medicine over the last few decades. Magnetic resonance techniques, originaly introduced in chemistry and physics, have become major non-invasive tools for the examination of human soft tissues. Conventional magnetic resonance imaging (MRI), together with contrast MRI (MRI after application of contrast agent), are now essential in the study of diseases of central nervous system (CNS) and the musculoskeletal system. MRI enables the description of tissue structure and integrity by using the natural presence of water molecules in human tissue. Different reaction to an external magnetic field provides a unique discrimination of tissue and pathology with no radiation risk. However, MRI by itself is unable to study biochemical and functional features of the examined tissue. This deficiency has led to innovations and the development of more sophisticated in vivo MR methods such as proton MR spectroscopic imaging (1H MRSI or SI), diffusion and perfusion imaging, MR relaxometry or functional MRI [1]. Although image contrast in MRI is based on T1 and T2 relaxation times (T1, T2 resp.) of the examined tissue, only MR relaxometry allows the calculation of their exact values. T2 relaxation times increase with a higher concentration of the free intracellular water in brain tissue. This quantitative MR method is therefore useful in neurology for objective assessment of tissue abnormalities. MRSI, based on the same physical phenomena as MRI, provides information about metabolic profile of tissues in vivo. Pathologic tissue shows changed metabolism reflected in altered metabolic concentrations which can be determined from in vivo MR spectra. Despite time constraints and the low sensitivity of the method due to low concentrations of metabolites observed in the tissues, 1H MRSI plays an important role in neurology and neurooncology for its ability to differentiate various lesion types and to assess the extent of the pathology in question. The tissue microstructure and molecular dynamics of water in the tissue can be visualised by diffusion-weighted imaging (DWI) and diffusion tensor imaging (DTI). Diffusion measurements are based on changes in the image contrast depending on the diffusion of water molecules in the tissue. Water diffusion in regions of high cellularity is restricted, while the movement of water molecules in low cellularity areas can be almost unrestricted. Diffusion imaging has been widely used in clinical practice to distinguish a tumour from bacterial abscess, to increase the specificity of lymphoma detection or to diagnose an acute

ischemia. At present, it is common to use qualitative description of radiological images in clinical practice; however, it has been shown [2, 3, 4, 5] that a quantitative analysis of different diagnostic methods provides more precise information about the nature and extent of the pathology in various diseases (differential diagnosis of human brain tumour and radiation necrosis, epileptic and neurodegenerative disorders, etc.). The knowledge of structural, biochemical and functional information from an array of available methods is crucial for optimal therapy planning and for the improvement of patient prognosis.

This thesis aims to present a new approach in the quantitative analysis of various MR methods using semiautomatic software CORIMA and its use in the examination of patients suffering from brain tumours and patients with drug-resistant temporal lobe epilepsy. Although these two diseases are not related from an etiology point of view, in both cases the only available treatment is neurosurgical resection of the pathology in question. For that reason, complex information describing nature and extent of pathology is crucial.

The thesis is divided into theoretical, experimental, results, discussion and conclusions sections. The theoretical background of the above mentioned MR methods as well as a description of the examined diseases are briefly reviewed in the theoretical section. The information about examined subjects, examination protocols and used data processing software are described in the experimental part. Imporatnt results, discussion and conclusions of original works are presented in the corresponding sections. A detailed description of the studies can be found in individual published papers attached in the Appendix.

2 Aims of the Thesis

The aim of this thesis was to develop a methodology combining standard MR imaging, MR spectroscopic imaging, diffusion tensor imaging and T1 and T2 MR relaxometry for evaluation of the spatial distribution of pathology in patients suffering from brain tumours and drug-resistant temporal lobe epilepsy (TLE) acquired using a 3T MR scanner. Each studied MR parameter represents distinct phenomena and consequently each method can reveal the differences in pathology extent. Therefore, the common quantitative evaluation of different MR methods has the potential to increase the specificity of diagnosing the pathological state of the tissue and consequently can help to improve the outcome of patients.

Several particular aspects of the use of a combination of different MR methods have been addressed:

1. Development of software enabling pixel-by-pixel image analysis and automatic visualisation of mutual relationships (correlations) between individual quantitative MR parameters.
2. The use of the correlations for tissue differentiation in patients with different types of newly diagnosed brain lesions, demonstration of their potential use in the clinical routine and its comparison with histopathological findings provided by frame-based image-guided stereotactic biopsy.
3. The use of the combination of different methods for differential diagnosis between tumour recurrence and radiation necrosis in irradiated patients after lesions resection and its benefit in neurooncological practice.
4. The use of correlations between individual quantitative MR parameters to assess hippocampal involvement in patients with drug-resistant temporal lobe epilepsy and its comparison with standard clinical diagnostic protocols.

3 Theoretical Part

The theoretical background of 1H MR spectroscopic imaging, MR diffusion and relaxation measurements, and MR features of tumour, suspected tumour recurrence after radio/chemotherapy and temporal lobe epilepsy are briefly reviewed in this section. Detailed information about the used MR techniques and the examined pathologies can be found in given references.

3.1 1H MR Spectroscopic Imaging

1H MR spectroscopic imaging has found its application in medicine in diagnosing various types of diseases such as epilepsy or oncological, neurodegenerative and hepatic diseases. Despite time constraints and the low sensitivity of the method due to low concentrations of metabolites observed in the tissue, the increasing presence of MRSI in standard presurgical protocols illustrates its increasing practical significance.

3.1.1 Basic Principles of MR Spectroscopic Imaging

Both MRSI and single voxel spectroscopy (SVS) enable to non-invasively provide information about the biochemical state of a tissue by measurements of metabolite signals in vivo in a defined region. However, only MRSI can encode spatial distribution of metabolites in the examined tissue and thus localise a pathology. Spectra from several voxels at different locations, instead of one in case of SVS, can be measured during a single measurement [6].In vivo 1H MR spectroscopy (MRS) is mainly based on slightly different precession frequencies of protons located in different parts of molecules caused by changes in the local magnetic field $\mathbf{B_0}$ due to electrons in chemical bonds. The frequency shift of each metabolite is related to the defined standard (to be magnetic field independent) and it is called the “chemical shift”. As information about chemical shifts of individual metabolites present in the signal in each voxel has to be preserved, the classical frequency encoding known from conventional MR imaging cannot be applied. Instead, phase encoding is used in MRSI sequences to obtain information about the spatial distribution of signals.

1D, 2D or 3D MRSI can be differentiated; therefore, a sequence design depends on dimensional resolution. The main scheme of 2D Point Resolved Spectroscopy - Chemical

Shift Imaging sequence (2D PRESS-CSI) is shown in Figure 3.1. In the case of 1D MRSI measured by the PRESS-CSI sequence, three selective radiofrequency pulses (rf pulses) applied simultaneously with magnetic field gradients in three orthogonal directions are used for an excitation of a rectangular region of interest. After the excitation by the first 90° pulse, transversal magnetisation is produced within a slice perpendicular to the **z** axis [7]. The dephased magnetisation is refocused by the first 180° pulse at time TE1/2. The spin echo occuring at the echo time TE1 is not evaluated. Instead, dephased magnetisation is again refocused by the second 180° pulse at the time TE1+TE2/2 to give an echo at the time TE1+TE2, when the data acquisition starts. Following the excitation pulse, a phase-encoding gradient *G* along the **x** axis is switched on for the time τ [8]. During this time, the precession frequency ω of all spins along the **x** axis is modified according to

$$\omega(x) = \gamma x G, \tag{3.1}$$

resulting in spacially distributed phase shift $\phi(x)$ at the end of the phase encoding

$$\phi(x) = -\gamma x G \tau, \tag{3.2}$$

where γ represents the gyromagnetic ratio and x represents spin positions along the **x** axis, with respect to the gradient isocenter at x=0.

The whole sequence is repeated N times with repetition time TR, while the gradient strength G is equidistantly changed in each sequence repetition. Denoting variable k_l for each gradient strength G_l of the l-th phase-encoding step

$$k_l = \frac{\gamma}{2\pi} G_l \tau = \frac{\gamma}{2\pi} l \Delta G \tau, \qquad l = -N/2 ... N/2 - 1 \tag{3.3}$$

the spatially dependent phase shift $\phi_l(x)$ corresponding to l-th phase encoding step equals

$$\phi_l(x) = -2\pi k_l x. \tag{3.4}$$

Measured signal $S(t, k_l)$ is then function of k_l

$$S(t, k_l) = \int_{sample} s(t, x) e^{-i 2\pi k_l x} dx, \tag{3.5}$$

where s(t,x) represents all elementary signals distributed along the **x** axis.

The measured signal $S(t,k_l)$ is the continuous Fourier transform (*FT*) of the signals $s(t,x)$ from elementary volumes. The positions of N voxels along the **x** axis can then be reconstructed by the inverse discrete Fourier transform (DTF^{-1}) [6]. Measured time domain signal $S(t,x)$ is often transformed to frequency domain signal $S(\omega,x)$ using the *FT* in time domain,

$$S(\omega, x) = \int_t S(t, x)dt, \tag{3.6}$$

which enables visual data interpretation. This $S(\omega,x)$ dependence is called a spectrum.

In the case of 2D PRESS-CSI, resp. 3D PRESS-CSI, two, resp. three orthogonal phase-encoding gradients are applied during each sequence repetition (see gradient lines G_x a G_y in 2D case depicted in Fig. 3.1). The number of phase-encoding gradient steps and their value ΔG correspond to number and size of each element of a matrix (obtained after the spatial reconstruction) and therefore influence the spatial resolution. The size of the matrix, called a spectroscopic grid, corresponds to the field of view (*FOV*) of the MRSI experiment. Details are described in [6, 8].

In reality, additional pulses for outer volume suppression [8, 9, 10] and for water signal suppression [11] are applied before the PRESS-CSI sequence.

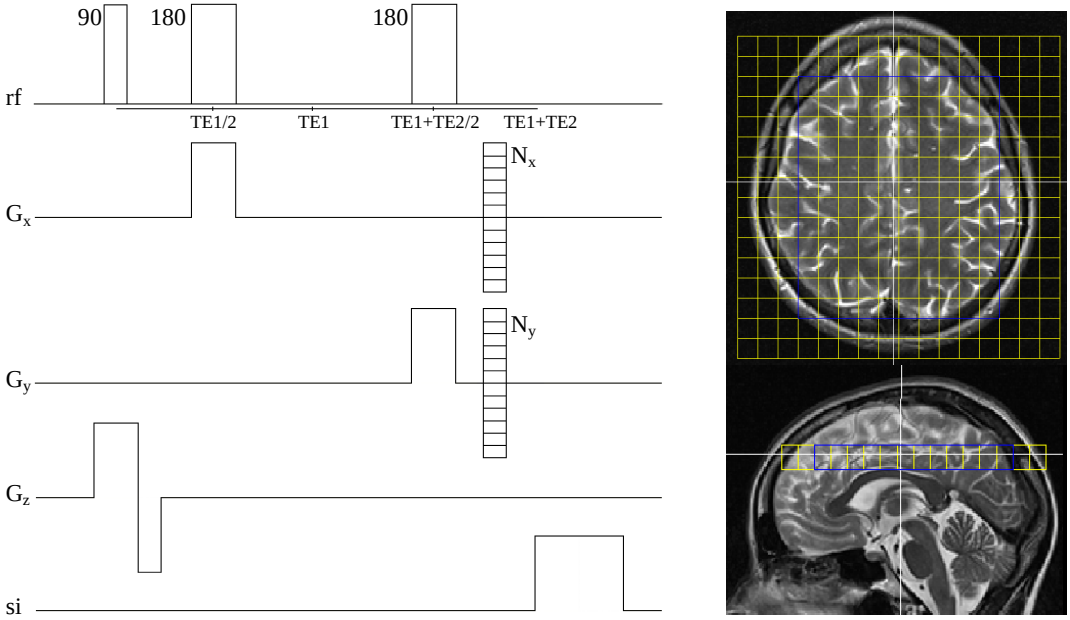

(a) (b)

Figure 3.1 a) The scheme of the 2D PRESS-CSI sequence and b) the size and the position of the pre-selected volume (highlighted in blue color) with respect to the spectroscopic grid (yellow) shown in transversal and sagittal plane.
90, 90-degree radiofrequency pulse; 180, 180-degree radiofrequency pulse; rf, radiofrequency channel; G_x, G_y, G_z, channels of magnetic field gradients switch on in **x**, **y**, **z** direction; si, measured signal.

3.1.2 Data Processing

The quality of data measured in *in vivo* MRS is often insufficient due to a number of limitations such as low metabolite concentrations, restricted measurement time resulting in a low signal-to-noise ratio (SNR) and poor magnetic homogeneity of magnetic field. However, there is a variety of methods called pre- and post-processing techniques allowing for the enhancement of the measured signal after measurement [12].

SI data preprocessing involves especially zero filling, spectroscopic grid shifting and k-space filtering. Zero filling consisting in appending of zeros to the acquired data S(t,$\mathbf{k_{l,m}}$) in k-space before FT is used to artificialy increase the number of measured voxels and therefore to achieve better resolution of spectroscopic images. Zero filling is just an interpolation method and does not change either point spread function (PSF) resulting from discrete FT [8, 13] or the spatial resolution of SI data. The possibility to shift spectroscopic grid stems from the properties of FT [13] and is very useful for minimalisation of partial volume effect (PVE) [8] and for the localisation of pathology in the voxel center. The aim of the k-space filtering is a minimalisation of PSF influence and therefore minimalises the influence of signal from the surrounding voxels to the measured signal. The filtering is based on the multiplication of acquired data with a symmetric function, i.e. filter, for example a Hamming function *w(l)* (in the case of 1D) [8] which has a maximum in the k-space center and decreases slightly to the margins

$$w(l) = 0.54 + 0.46\cos\frac{\pi l}{2l_{\max}}, \tag{3.7}$$

where l scans N sampling values and $l_{max}=N_{max}$.

The elementary signal in each voxel in the case of 2D SI is then reconstructed using DTF^{-1}

$$S(t,x,y) = \frac{1}{N_x}\frac{1}{N_y}\sum_{l,m} S(t,k_l,k_m)w(k_l)w(k_m)e^{2\pi i(k_l x + k_m y)}, \tag{3.8}$$

where N_x resp. N_y is a number of magnetic field gradients along **x** axis, resp. **y** axis, $w(k_l)$, resp. $w(k_m)$ is a filtering Hamming function along **x** axis, resp. **y** axis and k_l is a l-th step of phase-encoding along **x** axis, resp. m-th step along **y** axis.

To quantify spectra in each voxel, the spectra have to be analysed using some processing program. LCModel is the most commonly used commercial software for in vivo data processing in the frequency domain [14]. As LCModel does not provide any graphical interface required for comprehensive MRSI data processing, other dedicated software such as jSIPRO [15] is used for processing of huge amount of spectra. jSIPRO is a graphical

interface that makes use of the LCModel for spectra fitting and allows user friendly pre-processing and post-processing of SI data.

LCModel is based on a decomposition of measured *in vivo* spectra to spectra of individual metabolites either measured previously *in vitro* or simulated using quantum-mechanical simulations (see Fig. 3.2). This set of metabolites forms the so-called "basic set" for signal fitting. Detailed information is described in [6]. The metabolite concetrations are in LCModel calculated along with errors of estimate that are derived from Cramer-Rao bounds.

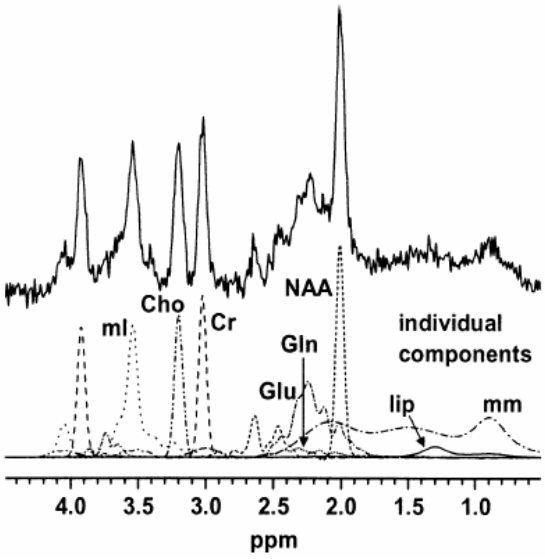

(a)

Concentration table: Ratio to: Cr+PCr

Metabolite	Conc.	Error	Ratio
N-acetyl as...	6.751	5	1.147
NAA+NAAG	7.544	3	1.282
Creatine	1.182	23	0.201
Cr+PCr	5.884	3	1
Creatine -Cr...	0.0	999	0
GPC+PCh	1.469	4	0.25
Glu+Gln	5.804	9	0.986
Inositol	5.479	5	0.931
Scyllo Inositol	0.237	22	0.04
Lactate	0.409	36	0.07
Taurin	1.715	25	0.291
GABA	0.627	47	0.107
GPC	1.469	4	0.25
PCh	0.0	999	0
PCr	4.702	8	0.799
NAAG	0.793	27	0.135
Glc	0.0	999	0
Glu	5.804	9	0.986
Gln	0.0	999	0
Asp	2.913	15	0.495

(b)

Figure 3.2 a) Decomposition of the measured spectra (top) to individual metabolite signals in the basic set (bottom). The figure adapted from [14]. b) The table of calculated metabolite concentrations, their errors and matabolite ratios to total creatine.
mI, myo-inositol; Cho, glycerophosphocholine; Cr, creatine; Glu, glutamate; Gln, glutamine; NAA, N-acetylaspartate; lip, lipids; mm, macromolecules.

3.1.3 Calculation of Absolute Metabolite Concentration

An assessment of absolute metabolite concentrations from fitted spectra is based on an assumption of the direct proportionality between the metabolite concentration and the detected signal. Basic information about concentrations C_{st} of calibrated standards measured from volume V_{st} is therefore possible to use for calculation of metabolite concentrations C_{met} measured from volume V_{met}.

Concentration C_{met} is calculated from the equation

$$\frac{S_{met}}{N_{met}V_{met}C_{met}} = \frac{S_{st}}{N_{st}V_{st}C_{st}}, \tag{3.9}$$

where S_{met} is the signal of the calculated metabolite, S_{st} is the signal of the calibration standard with known concentration C_{st} and N_{met} and N_{st} are numbers of protons contributing to the signal.

It should be noted that signals S_{met} and S_{st} do not generally represent the raw measured signal, but the measured signal modified by several additional corrections.

$$S^{cor}(l,m) = \frac{S(l,m)}{f_1 \cdot f_2 \cdots f_n}, \tag{3.10}$$

where $S(l,m)$ represents the measured signal, $S^{cor}(l,m)$ the corrected signal at the given position in the spectroscopic grid and f_i represent correction factors for individual corrections. These corrections depend on the measurement sequence in question and comprise PVE correction, correction for relaxation times, the receiver gain, the coil loading, excitation and reception profile, etc. More details can be found in [6].

3.1.4 Metabolic Profile of Healthy Human Brain

A 1H MR metabolic profile of the human brain is understood a qualitative and quantitative description of all 1H MR spectra of the human brain. The normal human metabolic profile contains a set of all measured spectra from healthy controls (Figure 3.3).

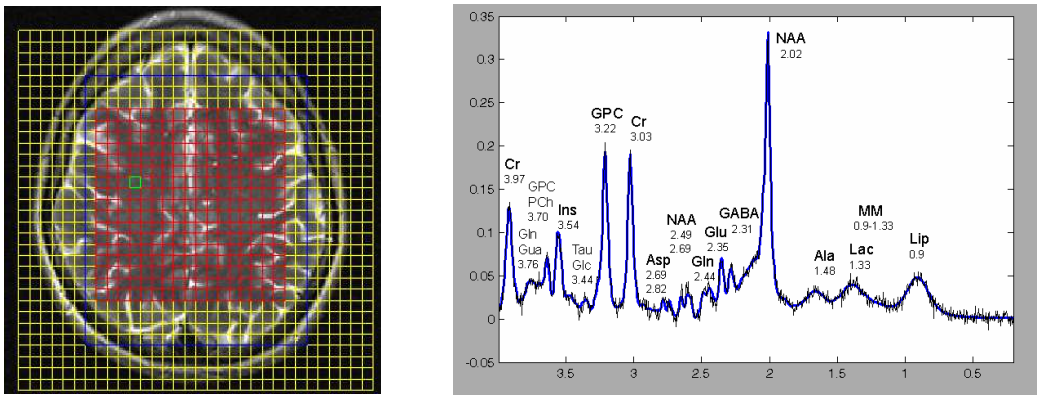

(a) (b)

Figure 3.3 a) The position of the spectroscopic grid (yellow) on the MR image with highlighted excitation VOI (blue) and calculated region of interest (red). b) The spectrum corresponding to highlighted green voxel in the spectroscopic grid. The black line represents a phased spectrum, the blue one fitted spectrum. PRESS-CSI sequence (Point Resolved Spectroscopy - Chemical Shift Imaging), time echo TE=30ms, repetition time TR=1510ms, number of acquisition NA=4. Spectra fitted by LCModel program. The chemical shift of each metabolite is stated in the corresponding signal.

Ala, alanine; Asp, aspartate, Cr, creatine and phosphocreatine; GABA, γ-butyric acid; Glc, glucose; Gln, glutamine; GPC, glycerophosphocholine; Glu, glutamate; Gua, guanidinoacetate; Ins, myo-inositol; Lac, lactate; Lip, lipids; MM, macromolecules; NAA, N-acetylaspartate; PCho, phosphocholine; Tau, taurine.

The most important metabolites studied using 1H MR spectroscopy are N-acetylaspartate together with N-acetylaspartylglutamate (NAA), creatine and phosphocreatine (Cr), choline-containing compounds (Cho; glycerophosphocholine together with phosphocholine and phosphatidylcholine), glutamine (Gln), glutamate (Glu), myo-inositol (Ins), lactate (Lac), lipids (Lip), macromolecules (MM), alanine (Ala), aspartate (Asp), γ-butyric acid (GABA), glucose (Glc), guanidinoacetate (Gua) and taurine (Tau). The structural chemical formulas of selected metabolites can be found in [16].

The highest signal in the healthy brain corresponds to methyl group of NAA, which is considered as a neuronal marker. Its decrease in lesions is a result of demyelinisation and subsequent neuronal dysfunction. Cho is a basic precursor of membrane synthesis. Increased Cho concentration has been attributed to the acceleration of membrane metabolism in actively proliferating tumour cells and to increased cell density [17, 18]. The Cr compounds represent an energetic supply for biological processes. Their increase has been attributed to the reactive astrogliosis. Ins as a osmolyte plays an important role in the regulation of calcium ions and therefore may be elevated due to inflammatory processes. Ins is also a precursor in lipid metabolism, so it may be increased in low grade gliomas due to increased cellular proliferation. Lac is a product of anaerobic glycolysis and is increased in necrotic tissue. Detailed information can be found in [16, 19].

A metabolic profile of the human brain can be easily studied with jSIPRO program. It enables to display a spectrum in each voxel of the spectroscopic grid separately (Fig. 3.3) or maps of selected metabolite within the measured VOI (Fig. 3.4). Displayed maps are scaled according to calculated concentrations. Voxels with the low spectra quality can be discarded from the analysis [15] based on the calculated Cramer-Rao bounds (Fig. 3.4).

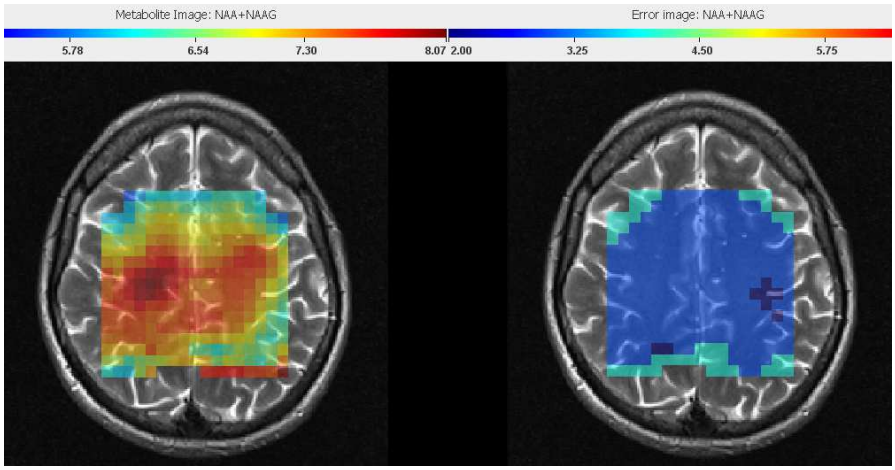

Figure 3.4 The metabolic and error image of N-acetylaspartate displayed using jSIPRO program. Voxels with Cramer-Rao bounds upon 4% are disabled in the images.

3.2 MR Diffusion Imaging

MR diffusion-weighted imaging and diffusion tensor imaging have found application especially in diagnosing diseases of the central nervous system as oncological, neurodegenerative, demyelinisation diseases and hyperacute ischemia. Diffusion imaging provides a unique method for assessing the integrity of the neuronal tissue and the orientation of neuronal fibers [20] and therefore plays an important role in presurgical planning.

3.2.1 Basic Principles of Diffusion Measurements

MR diffusion imaging is based on the measurement of changes of the MR signal in the presence of bipolar magnetic field gradients caused by molecular diffusion [21]. Molecular diffusion is related to random translational motion of molecules (Brownian motion) resulting from their thermal energy. The process of diffusion in the case of isotropic diffusion is described by Fick's first law, which relates a concentration gradient ∇u to a flux j (a flow across a unit area) [22]

$$j = -d\nabla u, \tag{3.11}$$

where d is a diffusion coefficient.

Both the most important and abundant molecule in biological tissues is the water molecule. Its diffusion motion is influenced by physical-chemical properties of intracelular space and by interactions with the underlying tissue microstructure, as intra and extracelular compartments, cell membranes, neuronal fibers, macromolecules, etc. Diffusion motion in biological tissues is therefore restricted more in one direction than in the others and become anisotropic (see Figure 3.5a). In this case, the diffussion cannot be fully described by the scalar diffussion coefficient d but only using the diffussion tensor $\boldsymbol{D}$. By application of magnetic field gradients in several different directions and the measurement of signal changes driven by diffusion in each of this direction, it is possible to reconstruct the corresponding diffusion tensor

$$D = \begin{pmatrix} D_{xx} & D_{xy} & D_{xz} \\ D_{yx} & D_{yy} & D_{yz} \\ D_{zx} & D_{zy} & D_{zz} \end{pmatrix}, \tag{3.12}$$

which is used in diffusion tensor imaging. The eigenvalues of the diffusion tensor represent the diffusion coefficients in the principal directions of diffusion [22]. The major eigenvector gives the direction of the greatest diffusion. The diffusion in each pixel is

therefore characterised by eigenvectors and its eigenvalues (see Figure 3.5b). Detailed information about DTI is described in [22, 23].

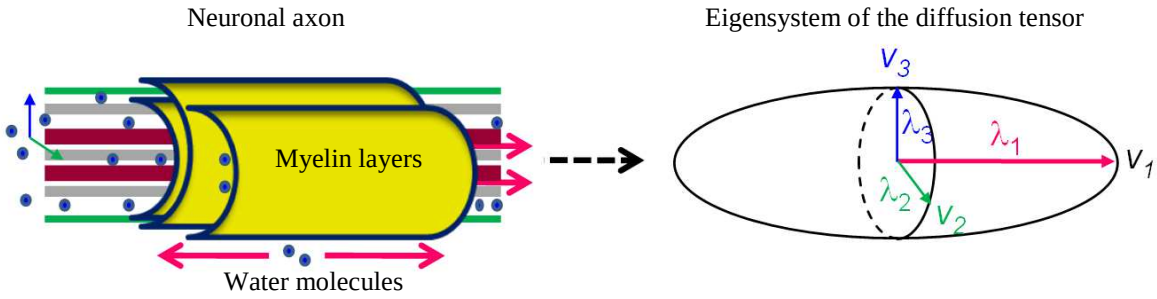

Figure 3.5 a) An idealised diagram showing the effect of axons on water diffusion and b) a diagram showing eigensystem of the diffusion tensor. Adapted from [23].
The major eigenvector v1 gives the direction of greatest diffusion (red arrows), it is not likely to be parallel to either tract. Water diffusion in other directions v2, v3 (blue, green arrows) is more restricted.

Besides the diffussion tensor, the mean diffusivity (MD) or the apparent diffusion coefficient (ADC) are used to show an average difusivity in each voxel regardless the difusion direction

$$MD = \frac{1}{3}\left(D_{xx} + D_{yy} + D_{zz}\right). \tag{3.13}$$

Introduction of more general diffusion coefficients (MD and ADC) better reflect biological conditions because other mechanisms also influence molecular diffusion (different cell compartments in one measured voxel, molecule motion driven by active transport, permeability membrane changes, concentration gradient flow, etc.) [23, 24, 25].

Sequences for diffusion imaging are constructed to sensitise the acquired image to the diffusion in a particular direction using magnetic field gradients (see Figure 3.6). Sequences containing pulsed gradients only in one direction are used for diffusion-weighted imaging (DWI), while DTI requires gradual measurement of diffusion images with different pulsed gradient orientations (used for the calculation of diffusion tensor) [26]. The degree of diffusion sensitisation (*b* value) is determined by the duration (δ) and the strength (height) of sensiting pulse-gradients (G), as well as the time interval between two pulsed gradients (Δ)

$$b = \gamma^2 G^2 \delta^2 (\Delta - \delta/3), \tag{3.14}$$

where γ is the gyromagnetic ratio. Thus, the diffusion sensitisation can be increased by using stronger and longer pulsed gradients or by increasing the time between the pulsed gradients [27]. The principles of the diffusion imaging can be demonstrated on the spin echo sequence with diffussion gradients. The signal in the spin echo can be fully recovered only if all excited spins sense the same magnetic field before and after the application of 180° rf pulse. In each image, wherever molecules diffuse in the direction of interest during imaging, the signal is lost as the spin phases are not fully refocused anymore (see Figure 3.6). The signal decrease S_b is described by the Stejskal-Tanner eguation [21, 27]

$$S_b = S_0 e^{-bMD}, \tag{3.15}$$

where S_0 is the signal intensity at a *b value* of 0; or by the natural logarithm

$$Ln(S/S_0) = -bMD. \tag{3.16}$$

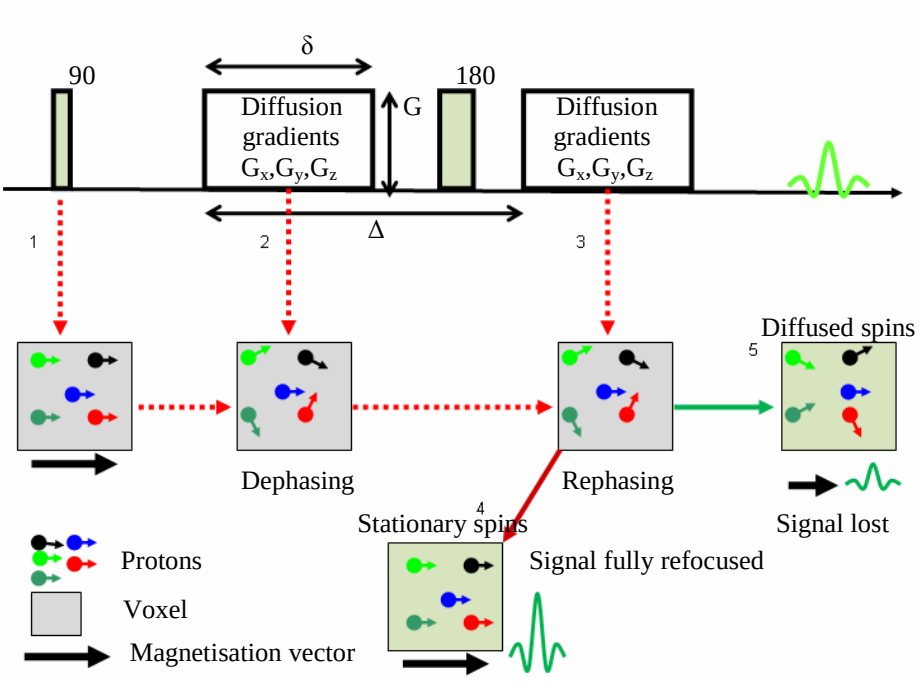

Figure 3.6 The graphical illustration of the Stejskal-Tanner pulsed bipolar gradient scheme used for diffusion measurements. It consists of standard spin echo sequence (90° and 180° rf pulses) and bipolar pulsed gradients in three directions. Adapted from [23].
Degree of diffusion sensitisation (b value) is determined by duration (δ) and strength (height) of sensiting pulsed gradients (G), and time interval between two pulsed gradients (Δ).
Magnetisation in a transversal plane (get after application of 90° rf pulse (1)) is lost due to spin dephasing caused by application of diffusion gradient (2). Only stationary spins are fully rephased (4) after application of 180° rf pulse and second diffusion gradient (3). Spin phases of molecules diffused in the directions of applied magnetic field gradients are not fully refocused and the signal is decreased (5).

As apparent from eq. 3.16, the acquisition of two diffusion-weighted images with different b values (commonly 50 and 1000 s/mm^2) while keeping the TE fixed allows for the determination of MD value for each image voxel as the coefficient of proportionality between two known parameters. Assigning a gray scale to the range of calculated MD values in all measured pixels constitutes an MD map (see Figure 3.7).

The measurments of diffusion images are mainly performed using echo planar imaging (EPI) sequences that allow the acquisition of the diffusion data in a relatively short time. In this case, multiple gradient echoes are generated in the EPI readout [28] that is added to the above mentioned Stejskal-Tanner sequence.

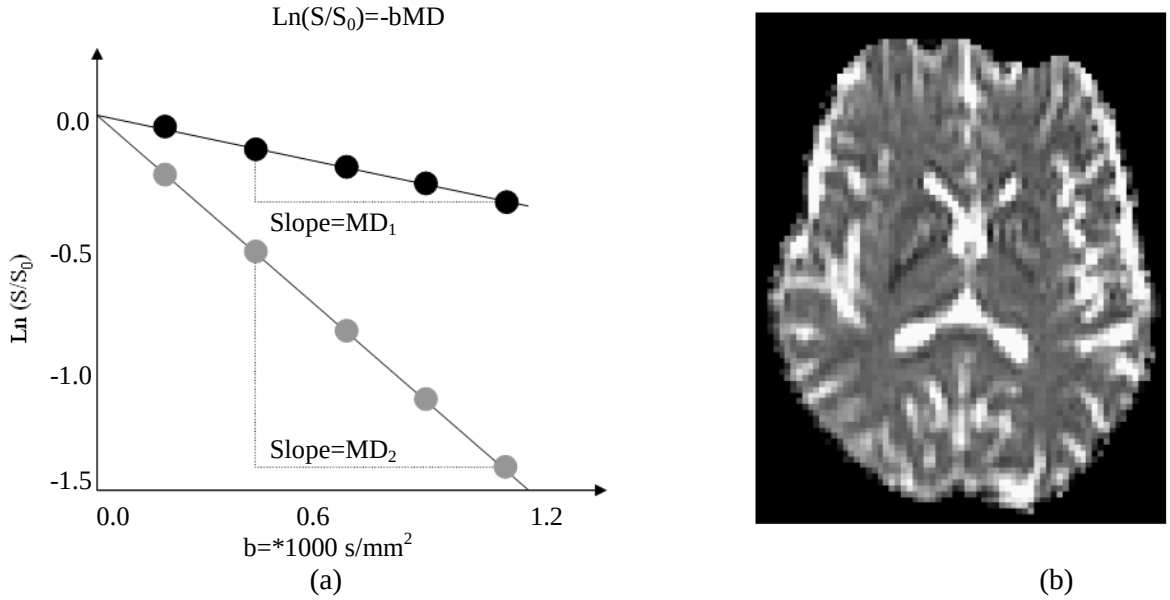

Figure 3.7 a) A graph of natural logarithm of signal intensity and b) the calculated map of mean diffusivity.
Natural logarithm of signal intensity from diffusion-weighted images with different degrees of diffusion weighting (b value) allows determination of mean diffusivity based on linear fit of data points. Absolute value of slope of plotted line, and thus mean diffusivity (MD), is greater for MD_1 (for example cerebrospinal fluid - white pixels on MD map) than for MD_2 (gray matter - dark gray pixels on MD map).

3.2.2 Data Processing and Calculation of Diffusion Maps

The diffusion data are often influenced by various artefacts as the inherent sensitivity of EPI sequences to motion and eddy current artefacts results in distortions in diffusion images. However, there is a variety of methods called post-processing techniques which allow data corrections and the enhancement of the measured signal after measurement [29,

30]. FSL [31] is one of the most commonly used free software tools for diffusion data processing. The FSL program assists in performing eddy current and motion corrections according to the reference image (commonly measured with b=0) and to average the data from each acquisition. Brain extraction with the FSL BET tool with selected fractional intensity threshold facilitates masking out the undesired data outside the brain. Diffusion tensor and parameters derived from it as MD and fractional anisotropy (FA) can be calculated in each voxel from brain-extracted data using the FSL DTIfit tool. An example of MD map calculated using FSL is shown in Figure 3.7b.

3.3 T1 and T2 MR Relaxometry

MR relaxometry is a quantitative MR method for objective assessment of the tissue signal abnormalities. Although especially conventional MRI based on relaxation mechanisms is widely used for examinations of pathologies, relaxometry measurements have also found application in medicine as they are capable to describe molecular dynamics of water in a biological tissue.

3.3.1 Basic Principles of Relaxation Measurements

Relaxation measurements are based on differences in rates of relaxation mechanisms in different biological environments. T1 and T2 relaxation times are phenomenologically introduced parameters [32] characterising the rate of the relaxation mechanism used by a biological system to return from a thermal non-equilibrium state to equilibrium after some perturbation is applied. The longitudinal relaxation time T1, also known as spin-lattice relaxation time, characterises the return of the magnetisation component in the direction of the external magnetic field to the equilibrium state [33]. This relaxation is caused by interactions (energy exchange) between the spin system and the molecular surroundings. The transverse relaxation time T2, also known as spin-spin relaxation time, characterises the rate at which the transverse component of the magnetisation decays to zero, and influences the line width of the signal in the MR spectrum. Disappareance of transverse magnetisation is a result of dephasing of the spins which is caused by small differences in spin precession frequencies since different chemical environment slightly changes local magnetic field. This relaxation is therefore caused by fluctuating magnetic fields at the sites of the nuclear spins caused by thermal motion of the molecules [32]. Similar to

diffusion measurements, the most appropriate molecule for studying relaxations of the biological tissue is the water molecule.

Modified spin echo sequences, such as the Carr-Purcell-Meiboom-Gill (CPMG) multiecho sequence, are often used for measurement of T2 relaxation times. Its basic concept is shown in Figure 3.8a. It contains one 90° rf pulse followed by a series of 180° rf pulses. Denoting τ time between the first 90° rf pulse and the first 180° rf pulse, the time difference between an excitation 90° rf pulse and the first echo is TE=2τ. Provided the 180° rf pulses are equidistant at times τ, 3τ, 5τ, etc., echoes (and corresponding T2-weighted images) are measured in times 2τ, 4τ, 6τ, etc. Under the assumption of a single exponencial dependence, the T2-weighted signal S_k in each pixel is given by [34]

$$S_k = N(T_1)e^{-kT_E/T_2}, \tag{3.17}$$

where k is the echo number and $N(T_1)$ is a T1-weighted proton density.

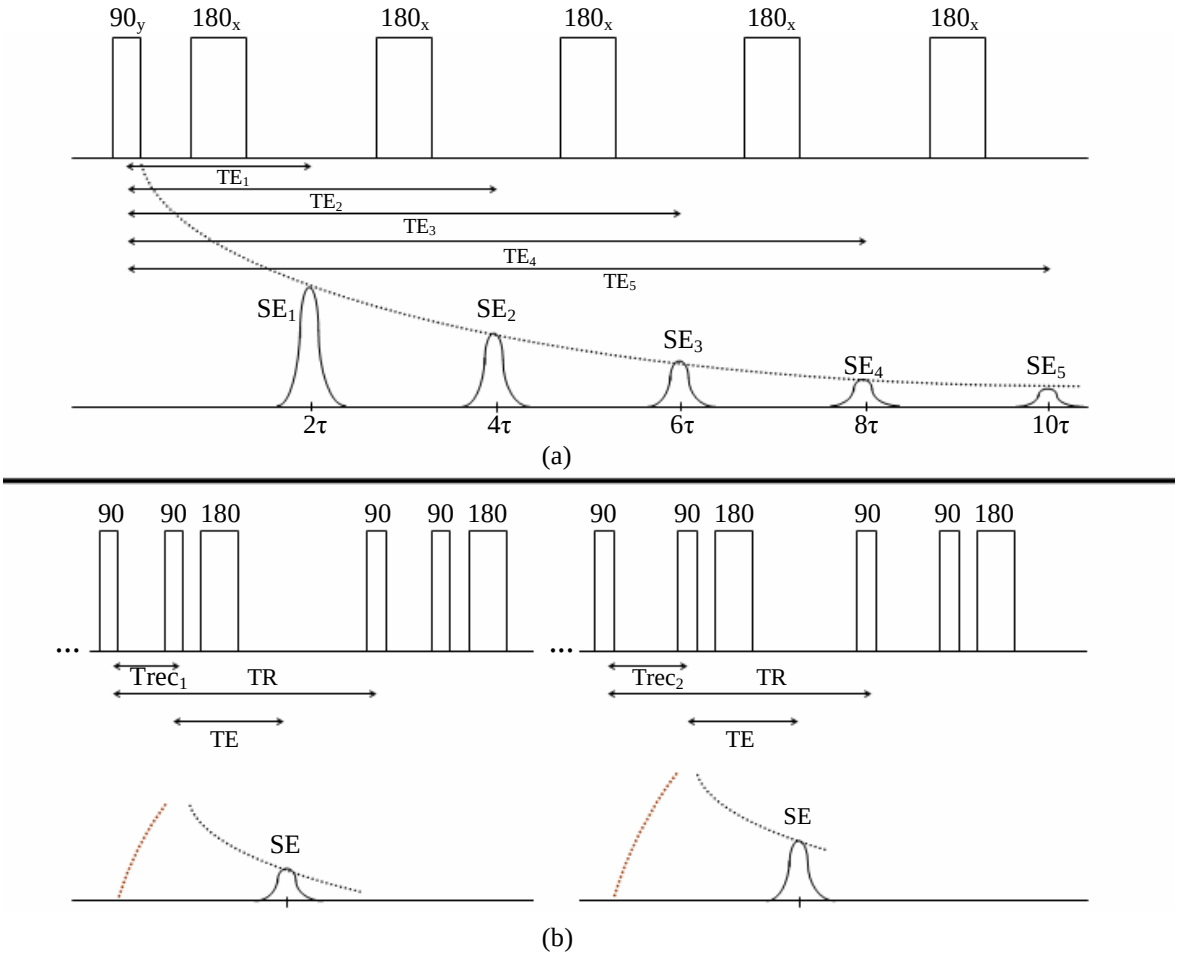

Figure 3.8 a) The scheme of CPMG multiecho sequence used for measurement of T2 relaxation times and b) the scheme of basic spin echo sequence used for measurement of T1 relaxation times.

a) CPMG sequence consists of one 90° rf pulse followed by a series of 180° rf pulses. The phase of the 90° rf pulse is shifted by 90° relative to the phase of the 180° rf pulses. Denoting τ time between 90° and first 180° rf pulses, the echo time TE_1 of the first spin echo SE_1 is 2τ. Second 180° rf pulse is applied 2τ after the first one, so the second spin echo SE_2 occurs at time 4τ, which is also echo time TE_2 of the second echo. $TE_3=6\tau$, $TE_4=8\tau$ and $TE_5=10\tau$ are the echo times of the third (SE_3), fourth (SE_4) and fifth (SE_5) spin echoes, respectively. The black dotted line shows signal exponential decay.
b) Saturation recovery spin echo sequence for T1 measurements consists of a non-selective 90° rf pulse followed by a selective 90° rf pulse and a non-selective 180° rf pulse. Note that longitudinal magnetisation (shown as a red dotted line) is not fully recovered yet when the second 90° rf pulse is applied, resulting in formation of T1-weighted spin echo. Therefore, selected Trec determines T1 weighting. Echo time TE is chosen as short as possible to minimalise the influence of T2 relaxation (shown by the black dotted line).

The phase of the 90° rf pulse is shifted by 90° relative to the phase of the first 180° rf pulse [33]. The successive pulses are coherent. This makes possible elimination of the cumulative error resulting from imperfect 180° flip angles. Magnetic field gradients for spatial resolution are applied together with rf pulses. Additionaly, gradient pulses (spoilers) on both sides of each 180° rf pulse are often applied to dephase unwanted FID (free induction decay), preventing it from interfering with the echoes. More details and the scheme of the whole sequence can be found in [34].

Images acquired with different TE values provide a set of data from which *T2* and $N(T_1)$ can be calculated as the best fit to the equation 3.17.

A saturation recovery spin echo sequence is one of the modified spin echo sequences used for measurement of T1 relaxation times. It consists of a non-selective 90° rf pulse followed by a selective 90° rf pulse and a non-selective 180° rf pulse (see Figure 3.8.b). The first 90° rf pulse saturates (zeros) the longitudinal magnetisation, which then recovers during the time interval Trec. After this time, the standard spin echo is acquired. As the longitudinal magnetisation is not fully recovered when the second 90° rf pulse is applied, the signal of the spin echo is T1-weighted [34]

$$S = N(T_2)(1-e^{-Trec/T_1}), \tag{3.18}$$

where $N(T_2)$ is a T2-weighted proton density.

The echo time TE is chosen as short as possible to minimalise the influence of T2 relaxation. Magnetic field gradients for for spatial resolution are applied together with rf pulses. More details and the scheme of the saturation recovery spin echo sequence can be found in [34].

In practice, a simplified sequence which utilises saturation from previous scans is used to shorten the acquisition time. Then the recovery time corresponds to repetition time TR.

Images acquired with different TR values provide a set of data from which *T1* and $N(T_2)$ can be calculated as the best fit to the equation 3.18.

3.3.2 Data Processing and Calculation of Relaxation Maps

Relaxation images represent a set of data for calculation of corresponding relaxation times. The relaxation series can be evaluated and relaxation maps calculated by the ViDi programme written in Matlab [35]. Evaluation is based on three-parameter fitting of the relaxation curve in each image pixel using a Marquardt-Levenberg algorithm. T2 values are calculated according to the equation $I = A*exp(- TE/T2) + B$ and T1 values according to $I = A*(1-exp(-TR/T1))+ B$. The software also aids in the elimination of data from pixels with a low signal-to-noise ratio and distant echoes if their intensity reaches the noise level (in the case of T2). In the case of T2 relaxation, it is also useful to omit the first echo before evaluation to minimise the error caused by imperfect pulses (the CPMG sequence compensates the cumulative error caused by imperfect pulses by a phase shift of the refocusing pulses; however, it cannot compensate the first echo) [35].
The example of a T2 relaxation map calculated using ViDi is shown in Figure 3.9b.

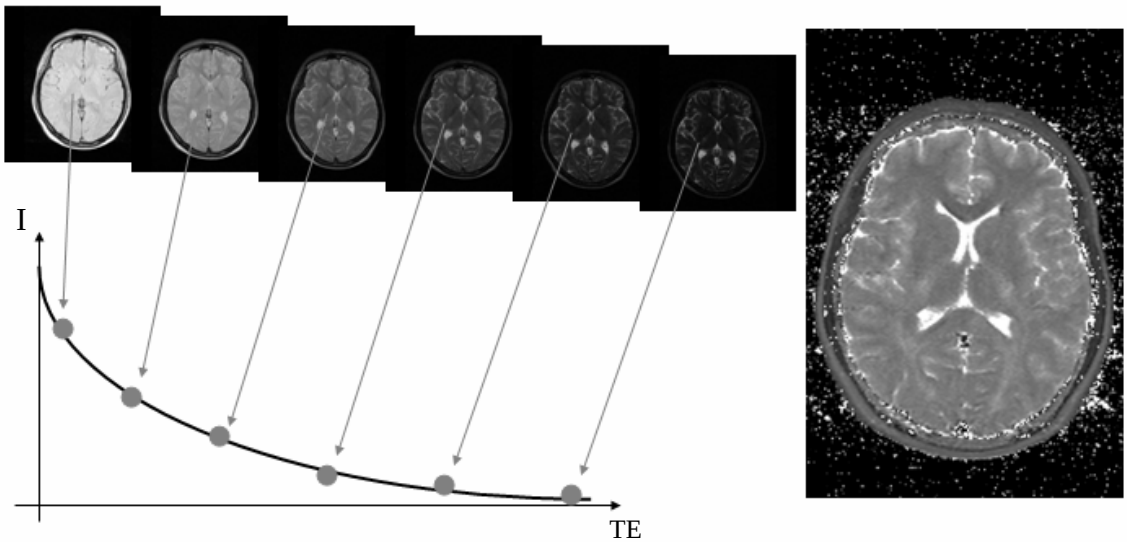

Figure 3.9 a) The exponential decay of intensities in T2 relaxation images according to echo time and b) calculated T2 relaxation map.
T2 relaxation time in each pixel is calculated according to an equation $I = A*exp(- TE/T2)+B$.
I, signal intensity; TE, echo time; T2, T2 relaxation time; A,B, fitting parameters.

3.4 Examined Pathologies and their MR Features

The pathologies examined in the study, their structural and metabolic features and related manifestation in the 3T magnetic field are briefly described in this section. More detailed information can be found in the cited references.

3.4.1 Human Brain Tumours

Primary brain tumours represent a signifiant medical, social and economic problem. Incidence of the disease is estimated at 25 per 100,000 of the adult population. The rate is even higher in developed countries. Approximately one third are malignant tumours, the rest are benign ones [36].

The most frequent human brain tumours are gliomas. From a histological point of view, gliomas are a heterogeneous group of tumours. A glioma can show several regions with different cell density, metabolism and structure of the tissue, like tumour-infiltrated brain tissue, necrotic regions, oedematous brain tissue and regions with a high density of tumour cells [37]. Because of the infiltrative nature of gliomas, treatment success is very poor [38]. For this reason, the correct diagnosis and the exact localisation of the tumour are crucial.

Magnetic resonance imaging is a method of first choice in diagnosing brain tumours. Nevertheles, a lack of specificity (60%) in distinguishing tumour types, their grades and tumour recurrence from a radiation and/or chemotherapy injuries is a major drawback. On the other hand, several MRI methods can be used for quantitative description of tumours to improve the outcome with a MR examination of patients.

Proton magnetic resonance spectroscopy non-invasively provides information on spatial distribution of metabolic changes in human brain tumours. Specific metabolic features of tissue changes have been found, however, no metabolic change represents a unique pattern of a particular type of tumour, especially due to the spatial heterogeneity of the tumour. Therefore, the MR spectroscopic imaging, either 2D or 3D, enabling the measurement of spacially resolved spectra has recently been widely used. Primary tumours are characterised by a decreased concentration of NAA, decreased Cr and elevated Cho. The low-grade gliomas also exhibit elevated Ins concentration. Decreased NAA, Cho, Cr and Ins and elevated concentration of Lac and Lip are features of necrosis [39, 40, 41, 42, 43, 44]. A peritumoural oedema is characterised by a lower concentration of all metabolites, without any change of NAA/Cho compared to healthy tissue [39, 45, 46]. These MRS findings have been confirmed by histopathologic data provided by target biopsies [47, 48,

49]. Detailed information about MRS features of selected tumour types can be found in [19, 50] and a graphical summary in Table 3.1. Examples of spectral differences are shown in Figure 3.10. Spatial spectral differences and spatial metabolic profiles (metabolic maps) of Cho, Cho/NAA, NAA and Cho/Cr are shown in Figure 3.11.

	NAA	Cho	Cr	Ins+Gly	Lac	Glu+Gln	Ala	MM	Lip
AS GII,III	↓	↑↑	↔	↑↑	↑	↔	↔	↑	↔
AS GIV	↓↓	↓	↔↓	↑	↑	↔	↔	↑	↔
LYM	↓↓	↑	↓↓	↔	↔↑	↔	↔	↑	↑↑
MET	↓↓	↑	↓	↔	↑	↔	↔	↔	↑
MEN	↓↓	↑↑	↓↓↓	↔	↑	↑↑	↑	↔	↓
GBM	↓↓↓	↑↑ , ↓↓(n)	↓↓↓	↔↑	↑↑(n)	↔	↔	↑	↑↑
GC	↓	↑	↑↑	↑↑	↔	↔	↔	↔	↔
ZAN, INF	↓↓	↑	↓	↔	↔	↔	↔	↔	↔

Table 3.1 Metabolic changes in different types of lesions.
AS, astrocytoma; G, tumour grade; LYM, lymphoma; MET, metastasis; MEN, meningeoma; GBM, glioblastoma multiforme; GC, gliomathosis cerebri; ZAN, INF, inflammation; NAA, N-acetylaspartate; cho, choline-containing compounds; Cr, creatine and phosphocreatine; Ins+Gly, sum of myo-inositol and glycine; Lac, lactate; Glu+Gln, sum of glutamate and glutamine; Ala, alanine; MM, macromolecules; Lip, lipids; ↑↑↑, significant increase; ↑↑, moderate increase; ↑, slight increase; ↔, no change; ↓, slight decrease; ↓↓, moderate decrease; ↓↓↓, significant decrease, almost vanished; (n), necrotic tissue occured in a measured area.

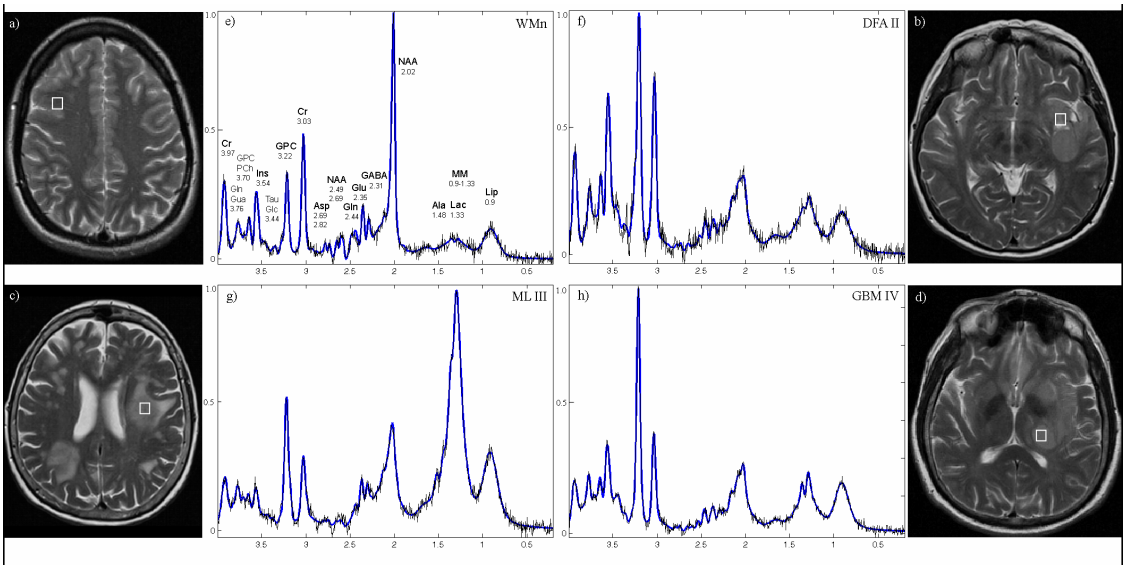

Figure 3.10 Experimental and fitted (blue line) 1H MRS spectra from white matter of centrum semiovale of a healthy control (e) and of different tumour types (f-h) and corresponding transversal MR images (a-d) with highlighted spectroscopic voxels at 3T. Adapted from [19].

PRESS-CSI sequence (Point Resolved Spectroscopy - Chemical Shift Imaging), time echo TE=30ms, repetition time TR=1510ms, number of acquisition NA=4. Spectroscopic voxels in lesions correspond to the stereotactic biopsy localisation. The signal intensities scaled to the highest signal in the spectrum. Spectra calculated by LCModel program. The chemical shift of each metabolite stated in the healthy spectrum (e).
WMn, normal white matter; DFA II, diffusion fibrilar astrocytoma grade II; ML III, malignant lymphoma grade III; GBM IV, glioblastoma multiforme grade IV; Ala, alanine; Asp, aspartate, Cr, creatine and phosphocreatine; GABA, γ-butyric acid; Glc, glucose; Gln, glutamine; GPC, glycerophosphocholine; Glu, glutamate; Gua, guanidinoacetate; Ins, myo-inositol; Lac, lactate; Lip, lipids; MM, macromolecules; NAA, N-acetylaspartate; PCho, phosphocholine; Tau, taurine.

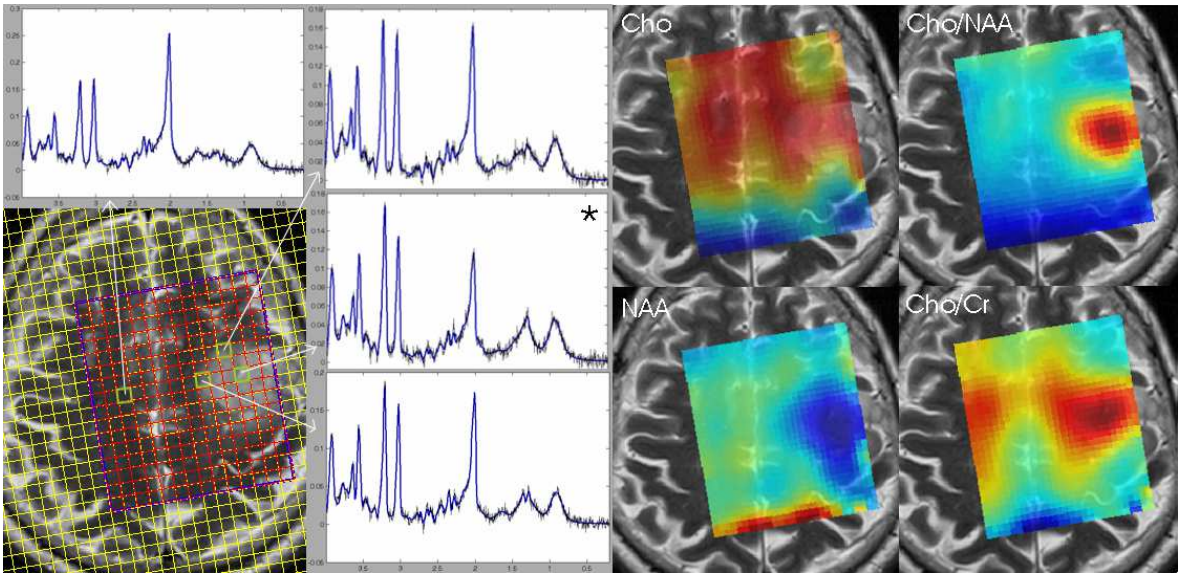

Figure 3.11 1H MRS spectra and metabolic maps in a patient with Oligodendroglioma grade II at 3T. Adapted from [19].
PRESS-CSI sequence (Point Resolved Spectroscopy - Chemical Shift Imaging), time echo TE=30ms, repetition time TR=1510ms, number of acquisition NA=4. The spectrum marked by star corresponds to the stereotactic biopsy localisation, the other spectra from different part of the lesion and from the healthy white matter (top left). Metabolic maps of choline-containing compounds (Cho), N-acetylaspartate (NAA), Cho/NAA ratio and ratio of Cho and total creatine (Cho/Cr) are visible in the right part of the figure.

Another method playing an important role in tumour diagnosis is MR diffusion-weighted imaging. DWI has been widely used in clinical practice to distinguish a tumour from a bacterial abscess, to increase the specificity of lymphoma detection or to diagnose an acute ischemia. A fractional anisotropy or mean diffusivity calculated from diffusion tensor imaging are rarely used in the clinical routine. Based on the diffusion of water molecules, this method provides information about the structure of the tumour on the microscopic level. Regions of low cellularity related to high extracellular space (cyst, necrosis, oedema) exhibit high MD, while those of high cellularity (low extracellular space) low MD [51, 52].

The differences in mean diffusivity between differrent tissue types are schematically shown in Figure 3.12.

Changes in T2 relaxation times reflect the structural changes in pathologic tissue. T2 values increase with a higher concentration of the intracellular free water in the brain tissue [53]. Different T2 values differ in different tumour types [43]; however, neither quantitative T2 relaxometry itself has potential to distinguished one to the other as T2 values differ also within one pathology. The differences between differrent tissue types are schematically shown in Figure 3.13.

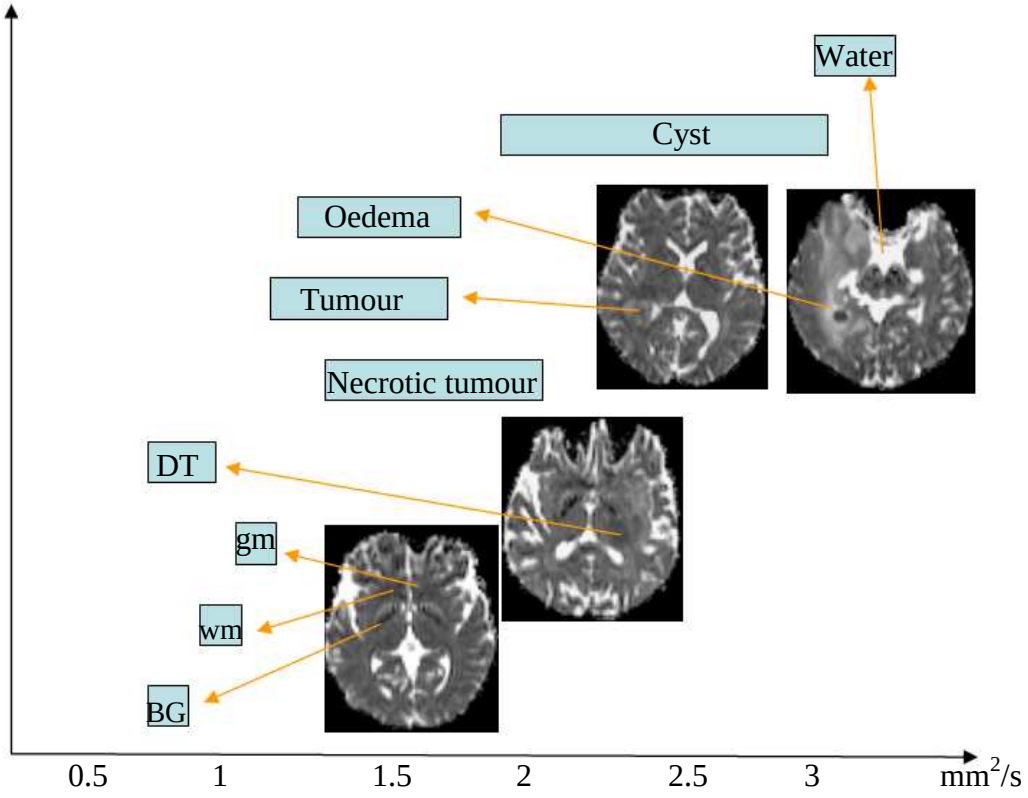

Figure 3.12 Mean diffusivity range for some common brain lesions and normal neuronal tissue. DT, dense tumour; gm, normal gray matter; wm, normal white matter; BG, basal ganglia.

A combination of different diagnostic methods may provide more precise information of the nature and extent of a pathology in patients with intracranial tumours. In particular, the conjunction of MRSI, DWI, perfusion (rCBV, relative cerebral blood volume) and T1 or T2 relaxation measurements (T1, T2, resp.) is very promising, since they provide complementary pieces of information: MRS reveals metabolic changes in the tissue,

whereas diffusion, perfusion and relaxation reflect the tissue structure. Coregistration of metabolic, diffusion, perfusion and relaxation images and their subsequent correlations based on multivoxel methods are primary used to assess the tumour extent [2, 3, 4, 19, 54, 55], as they have a potential to distinguish pathological states (tumour, oedema, oedema infiltrated by tumour, oedema, necrosis) and healthy tissue. A significant correlation on a pixel-by-pixel basis between Cho and MD measured at 1.5 T has been found in patients with high grade glioma (HGG) and has enabled the semiautomatic determination of the extent of tumour infiltration in individual patients [2]. However, the results with respect of patients with low grade glioma (LGG) have been ambiguous: both positive and inverse Cho-MD correlations have been reported [2, 3, 56]. Combination with single voxel methods are mainly used for detection of tumour recurrence or for tumour grading prognosis [57, 58, 59].

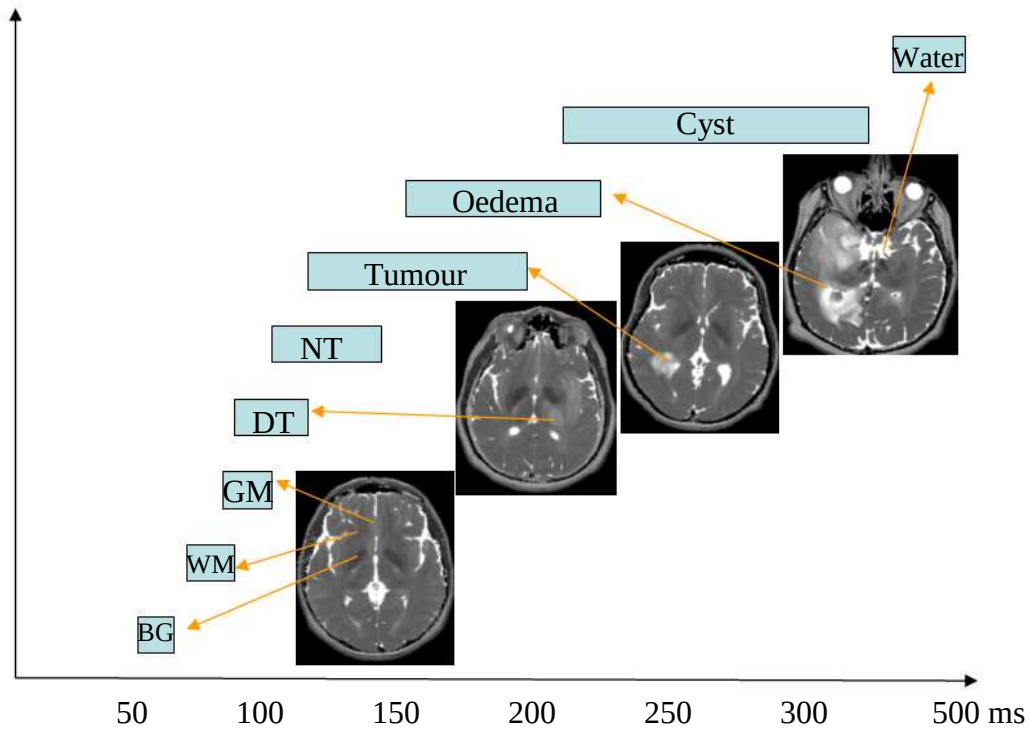

Figure 3.13 Water T2 relaxation times for some common brain lesions and normal neuronal tissue. NT, necrotic tumour; DT, dense tumour; GM, gray matter; WM, normal white matter; BG, basal ganglia.

3.4.2 Tumour Recurrence and Radiation Necrosis

Determination of an effective therapeutic protocol mainly in the case of malignant tumours is one of the most important challenges of clinical medicine. Standard treatment proposed in 2005 by European Organization for Research and Treatment of Cancer (EORTC) contains both radical surgical tumour resection followed by radiation therapy (RT; 60 Gy in 30 doses) and concomitant chemotherapy by temozolomid (TMZ; 75 mg/m2 during 42 days) followed by maintenance TMZ (150 -200 mg/m2 in a 5/28 schedule) for six additional cycles [60]. This therapeutic protocol verifiably leads to the prolongation of the life span of patients with a glioblastoma; however, in patients with a high grade tumour nevertheless reaches on average only 15 months (20% up to 2 years).

Incidence of radiation necrosis when only focal radiotherapy was used was estimated to 3-24%. However, the inclusion of adjuvant chemotherapy (chemoterapy after radiotherapy) into the standard treatment protocol caused an increase of the therapy-induced lesions up to three times compared to the protocol with radiotherapy only [61].Post-radiation changes and radiation necrosis may occur between 3 months and 2 years after radiotherapy termination. Histology changes often resemble necrotic changes (i.e., cellular necrosis, endothelial apoptosis, increased vascular permeability, oedema, gliosis) [62].

MRI often does not enable differential diagnosis of brain lesions, even with a contrast agent (see Figure 3.14). A typical example is a differential diagnosis between a recurrence of a viable tumour and a reaction to radio/chemotherapy. In both cases, the blood brain barrier is disrupted and the tissue is penetrated by the contrast agent which is manifested by signal enhancement on post-contrast T1-weighted MR images. Nevertheless, the therapy is in these cases different. A recurrent tumour required continuation of chemotherapy or another resection, a radiation necrosis is treated conservatively using steroids and its progression is monitored by routine MRI. Therefore, the correct diagnosis is a key factor for therapy determination and for improvement of the patients' prognosis [63].

Special attention has to be paid to the tissue treated by radiation or chemotherapy which exhibits different spectral and structural patterns compared to new diagnosed tumours. NAA corresponding to neuronal activity is not a specific marker for differentiation between tumour and radiation-induced lesions, as radio/chemotherapy destroyes viable neuronal cells, which also leads to decrease of NAA concentration. High Cho signal is a marker of progressing disease (see Figure 3.14), whereas normal or decreased values may

indicate therapy induced changes [55]. Several studies have revealed diagnostic potential of Cho/Cr and Lac+Lip/Cr ratios in differentiation between radiation necrosis and tumour recurrence [64, 65, 66, 67, 68]. Some studies [55, 69, 70] mentioned low ADC values and higher FA in the case of recurrent tumours compared to radionecrosis, whereas other studies presented inverse results [71].

Results of studies [64, 72] attempting to determine border values of ratios Cho/Cr, Cho/NAA, NAA/Cr for differentiation of viable tumour tissue and radiation necrosis are not consistent, mainly because they were not sufficiently supported by histopathology. A substantial problem is also low spatial resolution of MRS in heterogeneous lesions, which may be improved by 3D spectroscopic imaging.

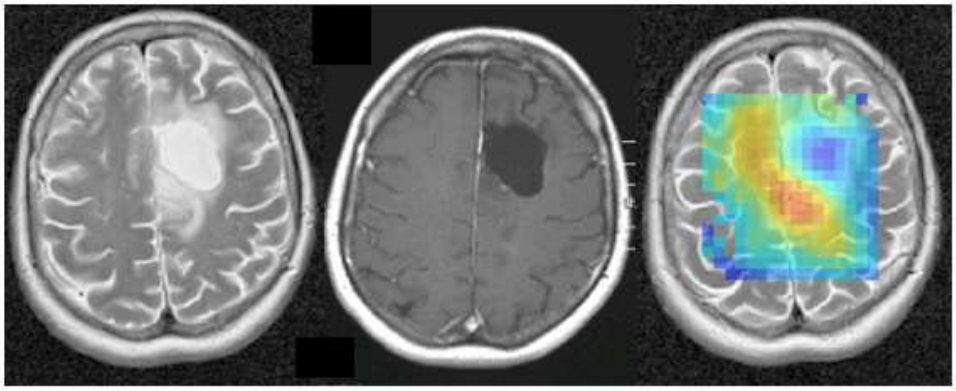

T2w MRI Contrast-enhanced T1w MRI Cho map

Figure 3.14 T2-weighted and contrast-enhanced T1-weighted MR image and the metabolic map in a patient with suspected tumour recurrence. The patient with oligoastrocytoma grade II was treated by subtotal tumour resection.
T2w, T2-weighted image; T1w, T1-weighted image; Cho, choline-containing compounds.

3.4.3 Temporal Lobe Epilepsy

Temporal lobe epilepsy (TLE) is surgically-remediable drug-resistant focal epilepsy. The most common subtype of TLE is a syndrome of mesial temporal lobe epilepsy (MTLE) where epileptic seizures originate from the mesial structures, particularly from the hippocampus (HC), parahippocampal gyrus and amygdala. Their electroencephalographic (EEG) data are characterised by the temporal or anterotemporal interictal spikes and rhythmic ictal pattern [73]. Symptomatic TLE is aetiologically divided into (1) MTLE associated with hippocampal sclerosis (HS), (2) lesional TLE caused by different structural lesions, and (3) cryptogenic TLE of unknown aetiology [74]. Whereas tumours and

malformations of cortical development are a more common cause of TLE in children, HS is the most common histological abnormality found in adult patients [75]. HS is characterised by hippocampal and extrahippocampal atrophy with neuronal cell loss and astrogliosis in HC and in the surrounding regions [76, 77, 78]. The epilepsy surgery offers the chance of a seizure-free outcome in the refractory TLE patients [79].

Magnetic resonance techniques, mainly MRI and MRS, are broadly used for localising the epileptogenic zone in different types of TLE and for the comprehension of the epileptogenesis mechanisms [80]. While the qualitative MRI reveals abnormal signal intensity on the T2-weighted images and structural changes on the high-resolution T1-weighted images in patients with MTLE-HS, the visual binary paradigm breaks down in the assessment of the disease extension, in the presence of the symmetric bilateral disease or in non-lesional cases (see Figure 3.15). A more accurate quantitative analysis can help in these cases.

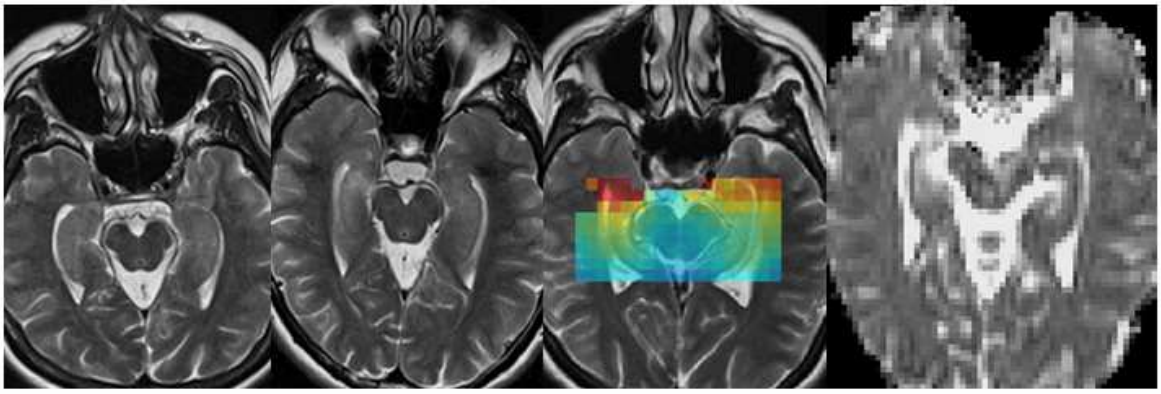

Non-lesional TLE HCsin	Hippocampal sclerosis dx	Hippocampal sclerosis dx	Hippocampal sclerosis dx
T2w MRI	T2w MRI	Cr/NAA map	MD map
(a)	(b)	(c)	(d)

Figure 3.15 T2-weighted MR images in a) a patient with non-lesional left temporal lobe epilepsy and b) a patient with right hippocampal sclerosis. c) The metabolic map and d) the map of mean diffusivity in a patient with right hippocampal sclerosis.
TLE, temporal lobe epilepsy; HC, hippocampus; sin, left; dx, right; T2w, T2-weighted image; Cr, total creatine; NAA, N-acetylaspartate + N-acetylaspartylglutamate; MD, mean diffusivity.

MR volumetry exhibited a significantly reduced hippocampal volume in patients with HS, but only minor changes in patients without HS [81]. Nevertheless, the manual and quantitative morphometrical studies revealed a widespread brain damage in the patients with TLE, especially the significant extrahippocampal atrophy which preferentially affects

the regions functionally and anatomically connected to the HC (parahippocampal gyrus, amygdala, thalamus, putamen, pallidum, middle and inferior temporal areas) [82, 83, 84, 85]. It was also noted that with a decrease of the hippocampal volume, the number of the white matter (WM) fibre tracts connecting the sclerotic HC to the rest of the brain decreases [78, 86].

Diffusion tensor imaging is based on the anisotropic water diffusion which is determined by intact membranes with an individual contribution of myelin and axonal membranes [20]. The primary lesions as well as the sclerotic HC exhibit a significantly increased MD (see Figure 3.15) and decreased FA ipsilateral to the epileptic focus without changes in the contralateral part [81, 87, 88]. On the other hand, some studies have found bilateral temporal lobe changes; nevertheless, the changes in the contralateral side have been less significant [78, 83, 85, 89]. Decreased MD has been found only postictally [90]. The non-sclerotic HC has not revealed any changes. The diffusion changes such as the increased MD and reduced FA probably reflect the neuronal loss in TLE.

T2 relaxometry is another widely used quantitative MR method for objective assessment of the tissue signal abnormalities [91, 92]. T2 relaxation times increase with a higher concentration of the intracellular free water in the brain tissue [53]. More than a 15% increase of the T2 values has been observed in the patients with severe HS ipsilateral to the seizure focus, a lower increase has been found in the mild HS cases [92]. These changes are attributed to the increased proportion of the glial cells [85]. Higher T2 values in the anterior than posterior HC have been also reported [93, 94].

MR spectroscopy reflecting metabolic changes has been regarded as a promising tool for the lateralisation of the epileptogenic zone in bilateral TLE cases or in TLE without HS. The majority of the studies have used spectra with a long echo time where three main signals are analysed: NAA, Cr and Cho. Lower NAA concentration, increased Cr and Cho and thus the abnormal NAA/Cr and NAA/(Cho+Cr) ratios have been found in the ipsilateral and sometimes in the contralateral temporal lobe in the TLE patients [77, 95] (see Figure 3.16). The NAA reduction has been attributed to the neuronal cell loss, the Cr changes to the reactive astrogliosis and the increased Cho to the dysplastic cortical lesion. However, it has been revealed that the spectroscopic changes reflect the neuronal and glial dysfunction rather than the neuronal cell loss, which means that the pathological basis underlying spectroscopic and volumetric changes is different [77, 96]. This suggestion is in line with the findings that the NAA and Cr level normalise in the peri-ictal or in the contralateral regions in the seizure-free patients after the epilepsy surgery [97, 98].

Therefore NAA/Cr or NAA/(Cho+Cr) ratios have been found the most useful parameters for lateralisation of epileptogenic zone (EZ).

Many studies have indicated that a combination of different diagnostic methods can help in the lateralisation of the epileptogenic zone in difficult cases. The factors predicting worse postsurgical outcomes in patients with the bilateral spectroscopic changes in temporal lobes included the negative MRI findings, the lower MD asymmetry index or lower MD ipsilaterally to the surgical side [99, 100]. Whereas some studies have revealed a significant correlation between ADC and the corresponding volume in the ipsilateral HC and amygdala in patients with TLE [85], others had not [81]. A significant correlation between NAA/(Cho+Cr) and ADC, and between ADC and T2 (ADC-T2) in the ipsilateral HC has been observed [81, 85, 101]. The ADC-T2 correlation has been also noted in the temporal lobe in the control subjects [85]. A negative correlation has been found between NAA/(Cho+Cr) and the T2 values in the sclerotic HC, while they have been uncorrelated in non-sclerotic HC [102].

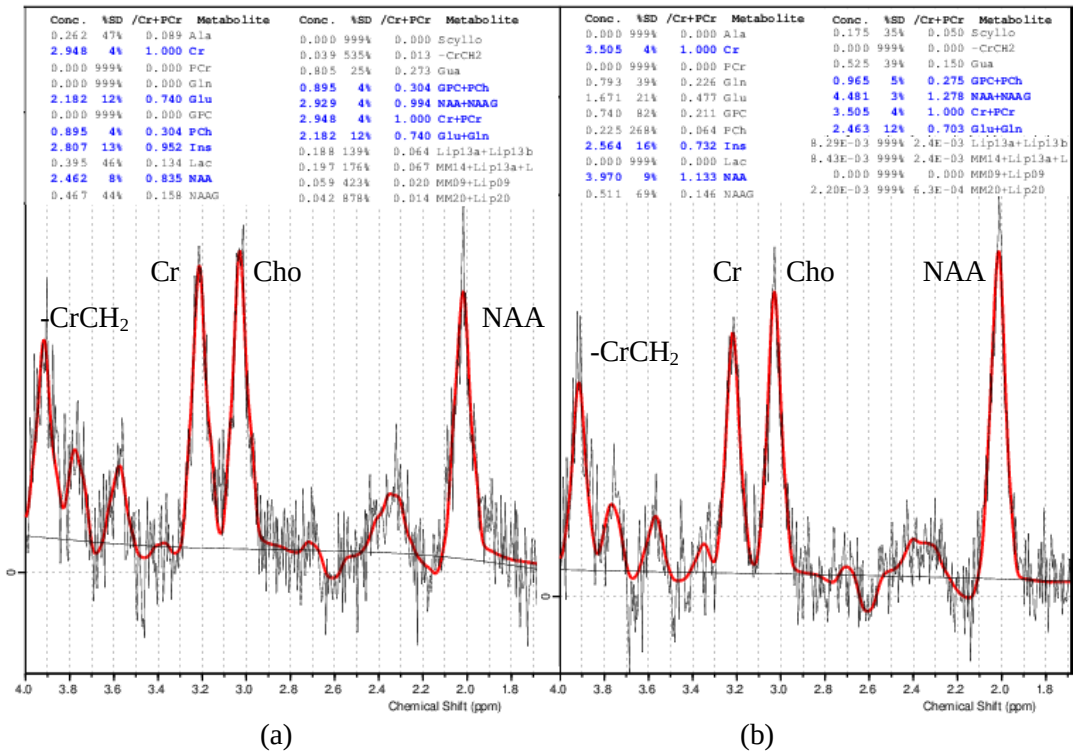

Figure 3.16 a) The example of spectra of pathologic hippocampus and b) of healthy hippocampus from a patient with temporal lobe epilepsy. The black line represents a phased spectrum, the red one fitted spectrum. Metabolite concentrations calculated by LCModel. NAA, N-acetylaspartate together with N-acetylaspartylglutamate; Cho, choline-containing compounds; Cr, total creatine; -$CrCH_2$, ethyl group of creatine.

4 Experimental Part

The demographic and clinical data of examined subjects, measurement protocols, sequences and their parameters used for MR data acquisition and processing techniques for data evaluation are described in this section.

4.1 Subjects

Both patients and healthy subjects were informed about the examination protocol and provided informed consent approved by the ethical committee of the Institute for Clinical and Experimental Medicine. Clinical protocols are certificated according to the ISO 9001:2008 norm.

4.1.1 Healthy Controls

Fifty-nine healthy subjects (twenty-nine men and thirty women) were included in the following studies as controls. The mean age of the subjects was 34.3 ± 13.4 years (ranged from 15 to 73 years). All healthy controls were carefully interviewed to exclude neurologic, psychiatric or other diseases affecting the obtained data.

In both hemispheres, the data were evaluated from the following regions: the centrum semiovale, parietal, occipital, periventricular region, cerebellum, temporal lobes, hippocampus, thalamus, basal ganglia, and cerebrospinal fluid (CSF).

Since metabolite concentrations, MD, T2 and T1 values are age related and significant differences were found in different parts of human brain, the control group for the study of brain lesions was divided into several subgroups according to their age (five age subgroups: 15-17; 18-34; 35-49; 50-62; 63-73 years) and examined region. Each subgroup consisted of 4-14 subjects.

Fifteen subjects (eight males, seven females, mean age 24.0 ± 2.2 years) in which the hippocampi were measured were used as a control group for the epilepsy study.

4.1.2 Patients with Tumours

Fifty-two patients (twenty-nine men and twenty-three women) were involved in this study. All patients were divided into two groups. Group 1 consisted of 30 patients with a new diagnosed lesion. Group 2 consisted of 22 patients with suspicion of a tumour recurrence

and/or radiation necrosis. Demographic and clinical data of all patients are summarised in Table 5.3. The mean age was 49.1 ± 15.3 years (ranged from 13 to 77 years).

Group 1:

None of the patients underwent any tumour treatment before the exam. The group of 30 patients was subdivided into low grade gliomas (LGG; 1 WHO grade I, 13 WHO grade II), high grade gliomas (HGG; 1 WHO grade III, 7 WHO grade IV), lymphomas (LYM; 4 cases) and other lesions (4 cases). An image-guided stereotactic biopsy of 26 patients was performed to assess the diagnosis, in 22 cases within 5 days after the MRS examination. Localisation of the biopsy specimen was determined by the treating neurosurgeon according to his or her judgement. The diagnosis of six patients was assessed from the MRI navigated open-frame biopsy during subtotal or total lesion resection. The diagnosis of the 4 remaining patients was assessed by a radiologist (see Table 5.3).

Group 2:

Patients who previously underwent at least one tumour resection and especially those with HGG were also treated with a suitable combined regimen of chemotherapy and/or radiotherapy (see Table 5.3). Several patients were examined repeatedly. This group consisted of 28 cases and was subdivided into a group of peri-cavity tumour recurrence (TRpc; 14 cases), tumour recurrence in new lesions (TRnl; 3 cases) and postradiation changes without tumour recurrence (RCh; 11 cases). All patients were regularly monitored by MRI and MRS measurements after the first suspicion of tumour recurrence. The image-guided stereotactic biopsy or tumour resection was performed in seven patients, the spectroscopy image-guided in four of them.

4.1.3 Patients with Temporal Lobe Epilepsy

Twenty TLE patients (ten males, ten females, mean age 29.6 ± 12.4 years) considered for resective surgery for intractable epilepsy were involved in the study. Demographic and clinical data are summarised in Table 5.5. Fifteen patients had abnormal radiological findings classified as lesional, remaining five patients were non-lesional. Besides MRI/MRS all the patients underwent the video-EEG monitoring, neuropsychological assessment and the ^{18}FDG-PET. The surgical side was determined according to the electro-clinical correlation and the results of all preoperative investigations.

Fifteen patients underwent temporal lobe resections, therefore their histopathological findings were available (see Table 5.5).

4.2 MR Measurements

The measurement protocols used in patients with tumours and in patients with TLE are described separately in two first subsections. Detailed information about the sequences and measurement parameters are stated in the third subsection.

4.2.1 Measurement Protocol in Patients with Tumours

The patients underwent standard clinical MRI examinations including contrast-enhanced (CE) MRI at 1.5T Siemens Symphony or Avanto tomograph (Siemens Medical Systems, Erlangen, Germany) in Na Homolce Hospital. These images were not included in the quantitative analysis. Consequently, they were examined on a 3T TrioTim scanner (Siemens Medical Systems) equipped with a transmit-receive head coil in Institute for Clinical and Experimental Medicine. The examination protocol included MRI, diffusion tensor imaging, 2D and/or 3D spectroscopic imaging and T2 and/or T1 relaxometry. The total scan-time was about 1 hour. Detailed information about the measurement parameters is described in Section 4.2.3.

4.2.2 Measurement Protocol in Patients with Temporal Lobe Epilepsy

The patients underwent a standard clinical MRI at 1.5T (Gyroscan Intera, Philips). These images were not included in the quantitative analysis. Consequently, they were examined on a 3T TrioTim scanner equipped with a transmit-receive head coil. The examination protocol included MRI, diffusion tensor imaging, spectroscopic imaging and T2 relaxometry. The total scan-time was about 1 hour. The whole protocol was performed in twelve patients, T2 relaxometry was omitted in four patients, DTI also in four patients, and in two patients the MRS data were available only from one HC for technical reasons. Detailed information about the measurement parameters is described in Section 4.2.3.

4.2.3 Measurement Parameters

MR Imaging: The protocol included T2-weighted sagittal, frontal and transversal images (T2W) and T1-weighted (T1W) sagittal images used for a visual lesion inspection and for the localisation of the spectroscopic volume of interest.

T2W images were obtained using a turbo spin echo sequence with parameters stated in Table 4.1. Field of view (FOV) was adjusted according to patient’s head size with constant

in-plane resolution. Slices were positioned without slice gap. In the case of tumourous patients, transversal images were positioned individually according to the lesion position with special attention to symmetric positioning over both hemispheres. In the case of epileptic patients, the transversal images were positioned in parallel to the long hippocampal axis and special attention was paid to the symmetric positioning over both HC.

T1W images were measured using a three-dimensional magnetisation prepared rapid acquired gradient echo sequence (MPRAGE) with parameters stated in Table 4.1.

T1W images with intravenous application of paramagnetic contrast agent were measured at 1.5T in collaborated hospitals (Na Homolce Hospital and Masaryk Hospital in Ústí nad Labem). Measurement parameters are stated in Table 4.1. Doses of applied contrast agent were under the local hospital policy.

	T2W; 3T; IKEM	**T1W; 3T; IKEM**	**T1W; 1.5T; NH**	**T1W; 1.5T; MH**
Sequence	TSE	MPRAGE	MPRAGE	MPRAGE
Orientation	Sagittal Frontal Transversal	Sagittal	Sagittal	Transversal
Number of slices	26	160	144	176
TR (ms)	4400	2300	2030	1900
TE (ms)	99	4.43	3.53	3.37
NA	1	1	1	1
FOV (mm^2)	260xHS 260xHS 230xHS	256xHS	256x208	256x192
Resolution (mm^3)	0.45x0.45x4.00	1.0x1.0x1.0	1.0x1.0x1.0	1.0x1.0x1.0
PAT factor	1	1	2	2
Measurement time (min)	~ 1	~ 6	4:08	3:55

Table 4.1 MRI measurement parameters.
T2W, T2-weighted images; T1W, T1-weighted images, 3T; magnetic field 3T; 1.T, magnetic field 1.5T; IKEM, Institute for Clinical and Experimental Medicine; NH, Na Homolce Hospital; MH, Masaryk Hospital; TR, repetition time; TE, echo time; NA, number of acquisitions; FOV, field of view; PAT, parallel acquisition technique; TSE, turbo spin echo; MPRAGE, three-dimensional magnetization prepared rapid acquired gradient echo; HS, head size. FOV was adjusted according to patient's head size with constant in-plane resolution.

2D and 3D 1H MR Spectroscopy: SI data were obtained using a Point Resolved Spectroscopy - Chemical Shift Imaging (PRESS-CSI) sequence with parameters stated in Table 4.2.

In the case of patients with tumour, the spectroscopic slice was positioned according to a supposed biopsy target and to be in parallel orientation to the conventional MRI, diffusion and T2 relaxation images. A manually assessed large excitation volume (VOI) was used for minimising the influence of the chemical shift artefact. Excitation VOI was always at least 1.5 cm smaller than FOV in each side. The shim volume used as the desired region of interest (ROI) was at least 1 cm smaller than VOI in the right-left direction on both sides and 1.5 cm smaller in the anteroposterior direction on both sides because the CSA is stronger in the anteroposterior direction (Figure 4.1). The spectroscopic ROI was as large as possible to include the different tissue types.

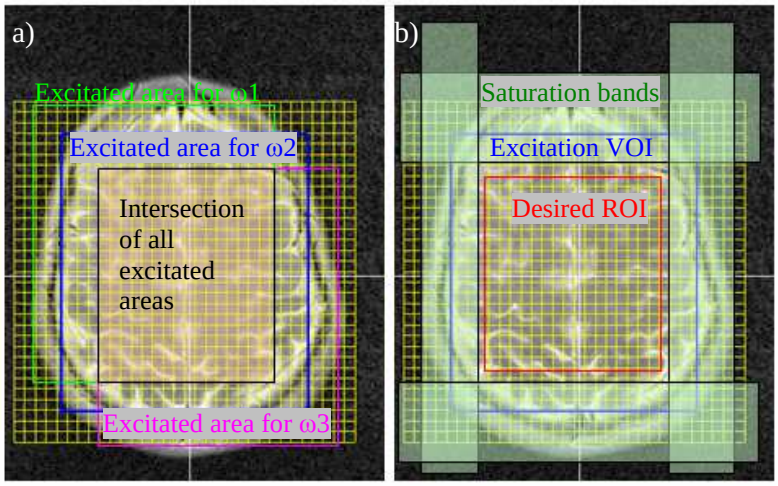

Figure 4.1 The schematic demonstration of differences in excitation areas according to selected frequency (a) and assessment of excitation and shim volumes and saturation bands (b).
ω, frequency

In the case of patients with temporal lobe epilepsy, the spectroscopic slice was positioned so as to cover both hippocampi and to be in parallel orientation with respect to the conventional MRI, diffusion and T2 relaxation images. In order to reduce the signal bias owing to the chemical shift artefact, the excitation volume was manually adjusted to the maximum extent possible. The excitation VOI was always at least 1.5 cm smaller than FOV in every side. The shim volume used as the desired spectroscopic ROI was at least 1.5 cm smaller than VOI in the right-left direction in every side and 2 cm smaller in the

anteroposterior direction in every side. It was adjusted symmetrically over both temporal lobes and manual shimming was used to achieve the best spectra quality.

The SI slices in healthy subjects were positioned in various parts of the brain to obtain control data for all brain parenchyma.

Special attention was paid to the positioning of saturation bands used for the effective suppression of the subcutaneous lipid signals.

T2 Relaxometry: For T2 measurement a modified 32-echo CPMG sequence was used with parameters stated in Table 4.3. FOV was adjusted according to the patient´s head size with a constant in-plane resolution. Relaxation slices were placed to the same position as the spectroscopic slice.

3T	**2D SI**	**3D SI**
Sequence	2D PRESS-CSI	3D PRESS-CSI
Orientation	Transversal	Transversal
TR (ms)	1510	1200
TE (ms)	30, 135	30, 135
NA	4	1
FOV (mm^3)	160x160x15	160x160x90
Phase encoding matrix	16x16x1	14x14x12
Interpolated phased encoding matrix	16x16x1	16x16x16
Resolution (mm^3)	10x10x15	10x10x5.625
Vector size	1024	512
Water suppression	With and without	With
Measurement time (min)	7:15	14:52

Table 4.2 Measurement parameters of spectroscopic imaging sequence
3T; magnetic field 3T; SI, spectroscopic imaging; TR, repetition time; TE, echo time; NA, number of acquisitions; FOV, field of view; PRESS-SI, point resolved spectroscopy imaging - chemical shift imaging.

T1 Relaxometry: T1 relaxation data were obtained using a series of SE sequences with parameters stated in Table 4.3. FOV was adjusted according to the patient´s head size with a constant in-plane resolution. Relaxation slices were placed in the same position as the spectroscopic slice.

Diffusion Tensor Imaging: DTI data were acquired using an echo planar spin echo diffusion tensor imaging pulse sequence with parameters stated in Table 4.3. FOV was adjusted according to the patient's head size with a constant in-plane resolution. Diffusion images covering a whole brain were positioned in the same orientation as transversal T2W images.

Neuropathology: All specimens were fixed in the 10% neutral buffered formalin and embedded in paraffin. Routine hematoxylin-eosin and cresyl violet staining were performed. A significant loss of pyramidal neurons in both the CA1 and CA4 hippocampal sector accompanied by gliosis was interpreted as HS. To assess the degree of gliosis in both the HC and the resected neocortex, standard immunoperoxidase staining was performed using antibodies against the glial fibrillary acidic protein (clone 6F2, DakoCytomation).

3T	T2 relaxometry	T1 relaxometry	DTI
Sequence	CPMG	SE	EPI-SE
Orientation	Transversal	Transversal	Transversal
Number of slices	3	1	44
Slice gap	No	No	No
TR (ms)	3000	3200, 1600, 800, 400, 200, 100, 50	7100
TE (ms)	ΔTE=13.2	6.9	98
NA	1	1,1,1 2,4,8,16	3
Echoes number	32	7	-
Directions	-	-	20
FOV (mm^3)	200xHS	210xHS	256xHS
b value (s/mm^2)	-	-	0, 1000
Phase encoding direction	RL	RL	AP
Resolution (mm^3)	0.78x0.78x5	0.78x0.78x15	2.0x2.0x2.5
Measurement time (min)	~ 7	~ 12	~ 7

Table 4.3 Measurement parameters of relaxation and diffusion sequences
3T; magnetic field 3T; DTI, diffusion tensor imaging; TR, repetition time; TE, echo time; NA, number of acquisitions; FOV, field of view; CPMG, Carr-Purcell-Meiboom-Gill multiecho sequence; SE, spin echo; EPI-SE, echo planar imaging spin echo diffusion tensor pulse sequence; ΔTE, echo spacing; HS, head size; RL, right-left; AP, anterior-posterior. FOV was adjusted according to patient's head size with constant in-plane resolution

4.3 Data Processing

Software and techniques used for data processing and evaluation are briefly described in this section. Detailed information about used programs can be found in the Theoretical part or in stated references.

4.3.1 MR Imaging and 1H MR Spectroscopic Imaging

The conventional MR images were visually assessed by neuroradiologists and epileptologists which were independent and blinded to clinical data.

SI data were analysed using the jSIPRO program, with a graphical LCModel-SI data interface [15, 103]. Data processing included mild k-space filtering (Hamming filter) to reduce point-spread function effects and zero filling to a 32x32 matrix size. Water signal was used as an internal standard for the calculation of metabolic concentration in laboratory units. No corrections either for relaxation times or for content of cerebrospinal fluid were performed.

4.3.2 Diffusion Tensor Imaging

DTI data were converted from the DICOM format to the NIFTI format using the dcm2nii tool and processed with FSL 4.1.5 [31] on a Linux workstation. FSL tools for eddy current and motion corrections were used. Brain extraction using the FSL BET tool with the fractional intensity threshold equal 0.3 was done. Mean diffusivity and fractional anisotropy were calculated in each voxel from brain-extracted data using the FSL DTIfit tool.

4.3.3 T1/T2 Relaxometry

T1/T2 relaxation maps were calculated using the ViDi program [35]. Image pre-processing included the reduction of the original image matrix to in-plane resolution to 1.56x1.56 mm to better match the spectroscopic resolution (this procedure also increases SNR), and exclusion of points with a low SNR prior to the fitting.

In the T2 images, areas where the fitting algorithm failed to converge due to too long relaxation time (usually T2 higher than 300 ms, such as in cerebrospinal fluid (CSF)) were filled in with white colour. Similarly, areas where it failed due to low SNR were replaced with black colour.

4.3.4 EEG Evaluation

The interictal EEG was assessed in terms of the ipsilateral or bilateral occurrence of spikes/sharp waves over the anterotemporal regions and/or in the sphenoidal electrode. The spikes were considered bilateral if more than 10% of the total spike count was observed contralaterally. On the basis of seizures recorded during the preoperative video-EEG monitoring ictal EEG was reviewed to classify the seizure onset as unilateral or bilateral. The seizure pattern was considered “bilateral” if rhythmic theta was seen over both temporal regions at the onset of the seizure or if independent seizures arising from both temporal lobes were recorded.

4.3.5 Neuropathologic Evaluation

The Palmini’s classification [104] was used for evaluating malformations of cortical development.

4.3.6 Correlation Analysis

Correlations and regression analysis were performed using the CORIMA interactive program developed as a part of this work [2, 105, 106]. It uses specific correlation patterns for tissue differentiation and control data for automatic identification of pixels corresponding to normal tissue. Therefore, it facilitates identifying regions with parameter abnormalities and assessement of pathology extent. A schema of the program is presented in Figure 4.2. The correlations are based on pixel-by-pixel evaluation of two different images, a metabolic, diffusion or relaxation map. There are two possible image combinations:

1. the metabolic map as the first image and the diffusion or relaxation map as the second one,
2. the diffusion map as the first image and the relaxation map as the second one.

The software allows the manual selection of the region of interest in the first image (Figure 4.2, item no. 2) and automatically finds the corresponding region in the second one (Figure 4.2, item no. 3). Each point in the correlation plot corresponds to one pixel in MR images. The correlations are then calculated from this selected ROI (item no. 4). To identify the position of particular points from the correlation plot in the examined tissue, the possibility to select a set of points in the correlation plot (item no. 5) and to highlight corresponding voxels in the first and second image was implemented in the program (item no. 6).

Several ROIs were examined in each subject. Assuming the tumour properties change from the tumour core towards its margins [3] the ROIs were selected as narrow strips oriented radially from the tumour core. Therefore, the ROIs include tumour tissue as well as a possible oedematous, tumour infiltrated and healthy tissue [106]. In the case of epileptic patients, regions of both hippocampi were evaluated separately in each subject.
The metabolic maps as well as the maps of metabolic ratios were used (NAA, Cr, Cho, Ins, Lac+Lip, Glu+Gln, Lac+Lip/Cr, Cho/Cr, Ins/Cr, Cr/NAA, Cho/NAA).

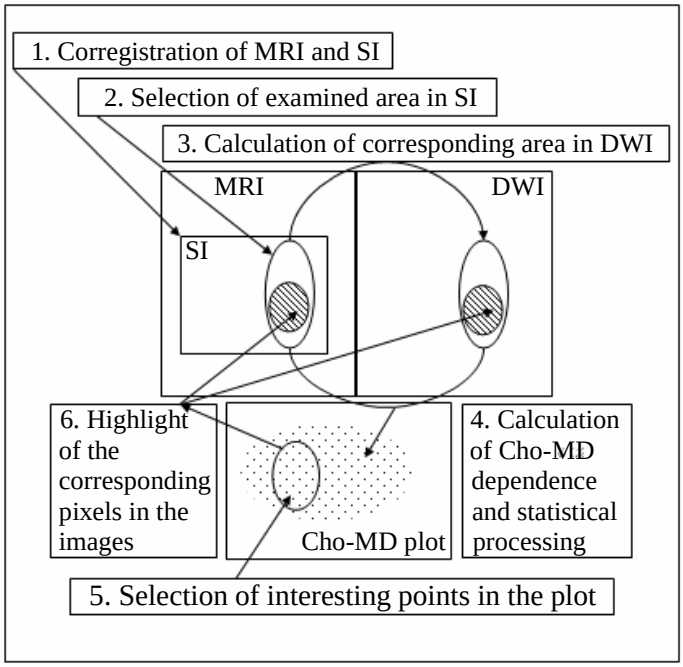

Figure 4.2 The schema of the CORIMA program
The program enables evaluating MR images (MRI, SI, DWI, T1 and T2 maps), create correlations between different MR parameters (i.e. Cho-MD correlation) and highlight the tissue region corresponding to the selected region on the plot. Adapted from [2].
MRI, MR image; SI, spectroscopic image; DWI, diffusion-weighted image; Cho, choline-containing compounds; MD, mean diffusivity.

The different slice thickness of spectroscopic, diffusion and relaxation data sets was accounted by the automatic averaging of a set of parallel diffusion or relaxation images obtained in the same volume corresponding to the spectroscopic slice. To account for different image resolution, the metabolic maps were interpolated to 128x128 pixels [105]. Detailed information about each processing step is described in the supplemented original paper [2, Appendix 1].

To exclude areas with low spectra quality only voxels with an error (Cramer-Rao bound) of the calculated metabolic concentrations lower than 40% in patients or 15% in healthy controls were included in the analysis [107]. The error boundary for the patients' spectroscopic data was increased because the Cramer–Rao is derived from the concentration of the appropriate metabolite and if there is low concentration of any metabolite in the ROI (the case of necrotic tissue) there must be a high value for Cramer–Rao. For a proposed hypothesis, it is necessary to develop the correlation from various types of pathology in each patient, necrotic tissue included [2].

Areas in which the relaxation times were not calculated due to low SNR or the failure of fitting algorithm (especially CSF and cavities) were excluded from correlations between mtabolites and relaxation times.

All control data were divided into several groups according to the subjects' age and measured regions. The brain was separated according to the following algorithm: Firstly, evaluated slice was classified according to its transversal positions (see Figure 4.3). Then each slice was automatically divided into eight or ten regions according to their left-right and anteroposterior positions. Control data sets for each group, i.e. for parietal, occipital and periventricular regions, the centrum semiovale and the cerebellum predominantly contained the data of the corresponding white matter. For each region, 15 MR parameters were evaluated.

The minimum (MIN) and maximum (MAX) values for each MR parameter and each region were assessed as a mean - standard deviation (SD) of each control data set, resp. mean + SD. These intervals represented control data used later for the semiautomatic evaluation of the patients' data for each image modality [2, 106]. These confidence intervals were highlighted in the controls' and patients' correlation plots by shading and bordered by blue lines (the MAX and MIN values) (see Figs. 5.1, 5.2, 5.4, 5.5). Every pixel falling inside this interval was highlighted automatically in the evaluating images and was interpreted as representing healthy tissue. The regions out of this confidence interval were considered as pathologic. Linear regression of the correlation plot, the calculation of the slope and the assessment of the 95% confidence interval of the regression line were performed in all subjects only from points outside the control data area. For the correlation analysis, a linear fit was used.

In the case of patients with tumour, for the correlation and regression evaluation, the data were divided into two intervals by the highest metabolic value or the highest MD (T2 resp.). Based on the biopsies and conclusions of previous studies [3, 5, 37, 56, 108]

different clusters were then interpreted as representing healthy tissue, oedema infiltrated by tumour, oedema or necrosis.

In the case of epileptic patients, the hippocampus with at least one of the metabolic, MD or T2 value above the corresponding MAX value was set as pathologic (Table 5.5, columns MRS-MD and MRS-T2). Significant changes in both HC were interpreted as bilateral pathology. Bilateral changes with significant asymmetry in at least one MR parameter were interpreted as bilateral pathology with one side predominance. The predominance cannot be assessed when the same parameter revealed comparable changes in both HC.

The influence of partial volume effects on the results of the studied correlation was examined by the simulations of the correlation analysis using model data and it is described in detail in [2].

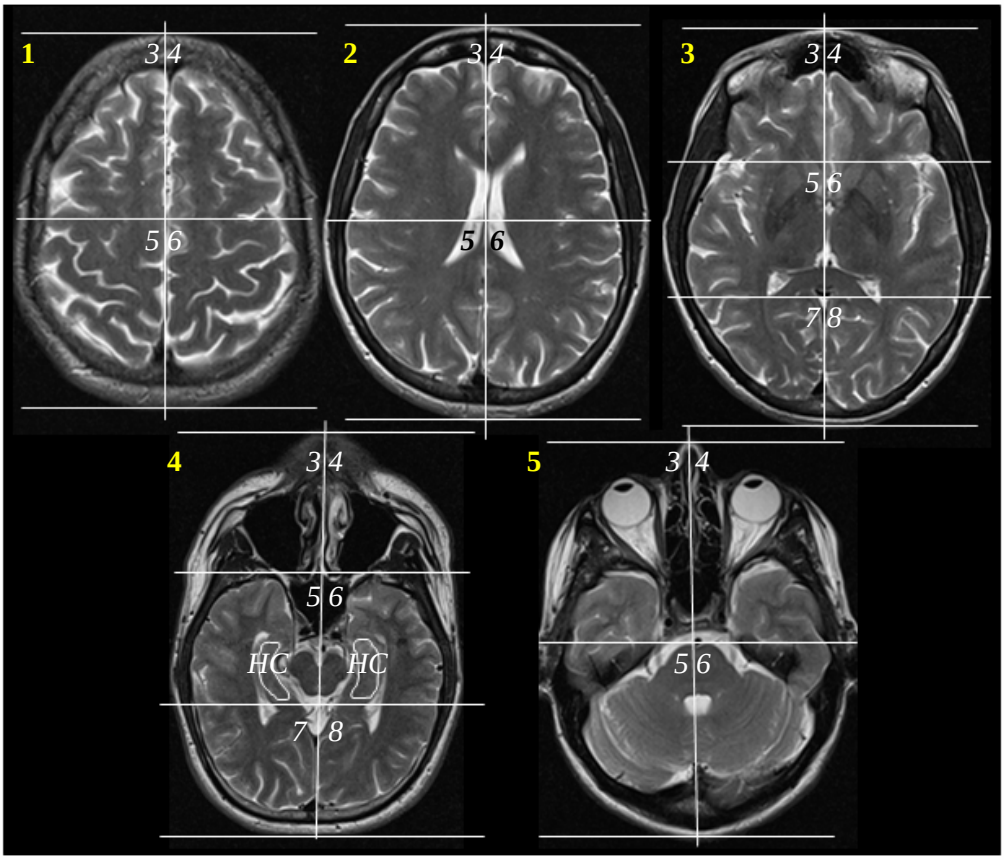

Figure 4.3 The brain separation in different transversal positions.
The transversal position must be specified manually by an operator (yellow). The separation within the slice is made automatically by CORIMA program (white numbers). Areas of hippocampi (HC) must be selected manually.

5 Results

The main results of each study are introduced in this section. It is divided into four subsections, the first one deals with healthy controls, the second one with untreated brain lesions, the third one with treated brain lesions and the fourth one with temporal lobe epilepsy. Already published results are shortly described in each section, the details can be found in the original papers supplemented in Appendix or in stated references.

5.1 Healthy Controls

Significant differences of metabolite concentrations, MD, T2 and T1 values were found in different parts of the brain. The parameter values, especially metabolite concentrations, were also age dependant. NAA, Cr, Glu+Gln decreased with age, while Cho increased. The whole control group was therefore divided into several subgroups according to age and the examined region. Mean values and their standard deviations for selected parameters in selected regions are shown in Tables 5.1 and 5.2. No significant differences were found between the corresponding regions in the right and left hemisphere. If the regions were examined separately, no significant correlations between metabolite concentrations and MD, T2 or T1 were found in any control subgroups in any region except the hippocampus. Examination of all regions of interest at once either invoked significant correlations or created separated clusters in correlation plots (see Figure 5.1). However, the correlation slopes did not reach the values found in the respective ROIs in patients.

In the hippocampi, NAA-T2 and NAA-MD showed a negative correlation. A positive correlation was found between T2 (or MD) and the following metabolites (or metabolite ratios): Cho, Cr/NAA, Cho/Cr, Cho/NAA. Cr-T2 and Cr-MD did not correlate (see Table 5.6). The examples of Cr/NAA-T2 correlations are shown in Figure 5.2 images 1a-1e. Mean value of the Cr/NAA-T2 slope in the control group was 0.006±0.004 and reached a maximum value of 0.011. MD, T2, Cho, Cr/NAA, Cho/Cr, Cho/NAA gradually decreased and NAA gradually increased in the anteroposterior direction of the hippocampus.

The correlation patterns for echo times TE=30 and 135 ms were similar in all subgroups. The maximal (MAX) and minimal (MIN) control values of each metabolite, MD, T2 and T1 were calculated for each subgroup (see Tables 5.1 and 5.2). These reference values were used for automatic separation of healthy tissue in each patient using the CORIMA program (see Figures 5.1, 5.2, 5.4 and 5.5).

TE=135 ms	Control group with age 18-34 years								
	NAA [a.u.]	**Cr [a.u.]**	**Cho [a.u.]**	**Ins [a.u.]**	**Cr/NAA**	**Cho/Cr**	**T1 [ms]**	**T2 [ms]**	**MD [.10^{-4} mm^2/s]**
Hippocampus									
Mean	4.05	2.93	1.00	1.99	0.72	0.34	1111	82.6	8.88
SD	0.31	0.35	0.12	0.47	0.15	0.08	42	9.5	0.64
MIN	3.74	2.58	0.88	1.52	0.57	0.26	1069	73.1	8.24
MAX	4.36	3.28	1.12	2.46	0.87	0.42	1153	92.1	9.52
Frontal WM in a centrum semiovale, right hemisphere; region 1-3									
Mean	6.36	3.30	1.04	2.32	0.52	0.32	795	75.8	6.88
SD	0.60	0.15	0.08	0.35	0.06	0.04	57	2.5	0.29
MIN	5.76	3.15	0.96	1.97	0.46	0.28	738	73.3	6.59
MAX	6.96	3.45	1.12	2.67	0.58	0.36	852	78.3	7.17
Frontal WM in a centrum semiovale, left hemisphere; region 1-4									
Mean	6.34	3.20	1.01	2.06	0.50	0.32	816	75.3	6.95
SD	0.73	0.21	0.15	0.55	0.08	0.06	57	2.1	0.25
MIN	5.61	2.99	0.86	1.51	0.42	0.26	759	73.2	6.70
MAX	7.07	3.41	1.16	2.61	0.58	0.38	873	77.4	7.20
Periventricular WM, right hemisphere; region 2-5									
Mean	6.39	2.45	0.84	1.61	0.38	0.34	860	75.9	7.91
SD	0.63	0.33	0.08	0.29	0.08	0.07	67	1.3	0.14
MIN	5.76	2.12	0.76	1.32	0.30	0.27	793	74.6	7.77
MAX	7.02	2.78	0.92	1.90	0.46	0.41	927	77.2	8.05
Periventricular WM, left hemisphere; region 2-6									
Mean	6.63	2.66	0.90	1.63	0.40	0.34	910	76.4	7.98
SD	1.31	0.59	0.16	0.30	0.11	0.09	69	1.8	0.23
MIN	5.32	2.07	0.74	1.33	0.29	0.25	841	74.6	7.75
MAX	7.94	3.25	1.06	1.93	0.51	0.45	979	78.2	8.21

Table 5.1 Control data in selected regions for subject' age between 18 and 34 years.
Mean, control mean value of the parameter; SD, standard deviation, MAX, maximal value, MIN, minimal value; NAA, N-acetylaspartate+N-acetylaspartylglutamate; Cr, total creatine; Cho, choline-containing compounds; MD, mean diffusivity; T1, T1 relaxation time; T2, T2 relaxation time; WM, white matter. MIN and MAX values define the control data intervals. MAX values correspond to blue lines in correlation plots.

TE=135 ms			Control group with age 35-49 years						
	NAA [a.u.]	**Cr [a.u.]**	**Cho [a.u.]**	**Ins [a.u.]**	**Cr/NAA**	**Cho/Cr**	**T1 [ms]**	**T2 [ms]**	**MD [.10^{-4} mm^2/s]**
Parietal WM, right hemisphere; region 1-5									
Mean	5.81	2.80	0.95	2.09	0.48	0.34	863	75.7	7.07
SD	0.30	0.09	0.03	0.13	0.04	0.02	67	3.1	0.41
MIN	5.51	2.71	0.92	1.96	0.44	0.32	796	72.6	6.66
MAX	6.11	2.89	0.98	2.22	0.52	0.36	930	78.9	7.48
Frontal WM in a centrum semiovale, right hemisphere; region 1-3									
Mean	5.63	2.98	1.08	2.32	0.53	0.36	811	72.1	7.01
SD	0.58	0.12	0.03	0.15	0.08	0.03	63	4.2	0.35
MIN	5.05	2.86	1.05	2.17	0.45	0.33	748	67.9	6.66
MAX	6.21	3.10	1.11	2.47	0.61	0.39	874	76.3	7.36
Frontal WM in a centrum semiovale, left hemisphere; region 1-4									
Mean	5.35	2.81	1.06	2.39	0.53	0.38	817	72.4	7.05
SD	0.45	0.13	0.03	0.35	0.07	0.03	69	4.7	0.35
MIN	4.90	2.68	1.03	2.04	0.46	0.35	748	67.7	6.70
MAX	5.80	2.94	1.09	2.74	0.60	0.41	886	77.1	7.40
Periventricular WM, right hemisphere; region 2-5									
Mean	5.65	2.50	0.87	1.76	0.44	0.35	867	73.4	7.81
SD	0.51	0.15	0.05	0.21	0.07	0.04	69	4.9	0.21
MIN	5.14	2.35	0.82	1.55	0.37	0.31	798	68.5	7.60
MAX	6.16	2.65	0.92	1.97	0.51	0.39	936	78.3	8.02
Periventricular WM, left hemisphere; region 2-6									
Mean	5.63	2.42	0.92	1.37	0.43	0.38	892	74.6	7.84
SD	0.47	0.16	0.07	0.35	0.06	0.05	75	5.5	0.24
MIN	5.16	2.26	0.85	1.02	0.37	0.33	817	69.1	7.60
MAX	6.10	2.58	0.99	1.72	0.49	0.43	967	80.1	8.08

Table 5.2 Control data in selected regions for subject' age between 34 and 49 years.
Mean, control mean value of the parameter; SD, standard deviation, MAX, maximal value, MIN, minimal value; NAA, N-acetylaspartate+N-acetylaspartylglutamate; Cr, total creatine; Cho, choline-containing compounds; MD, mean diffusivity; T1, T1 relaxation time; T2, T2 relaxation time; WM, white matter. MIN and MAX values define the control data intervals. MAX values correspond to blue lines in correlation plots.

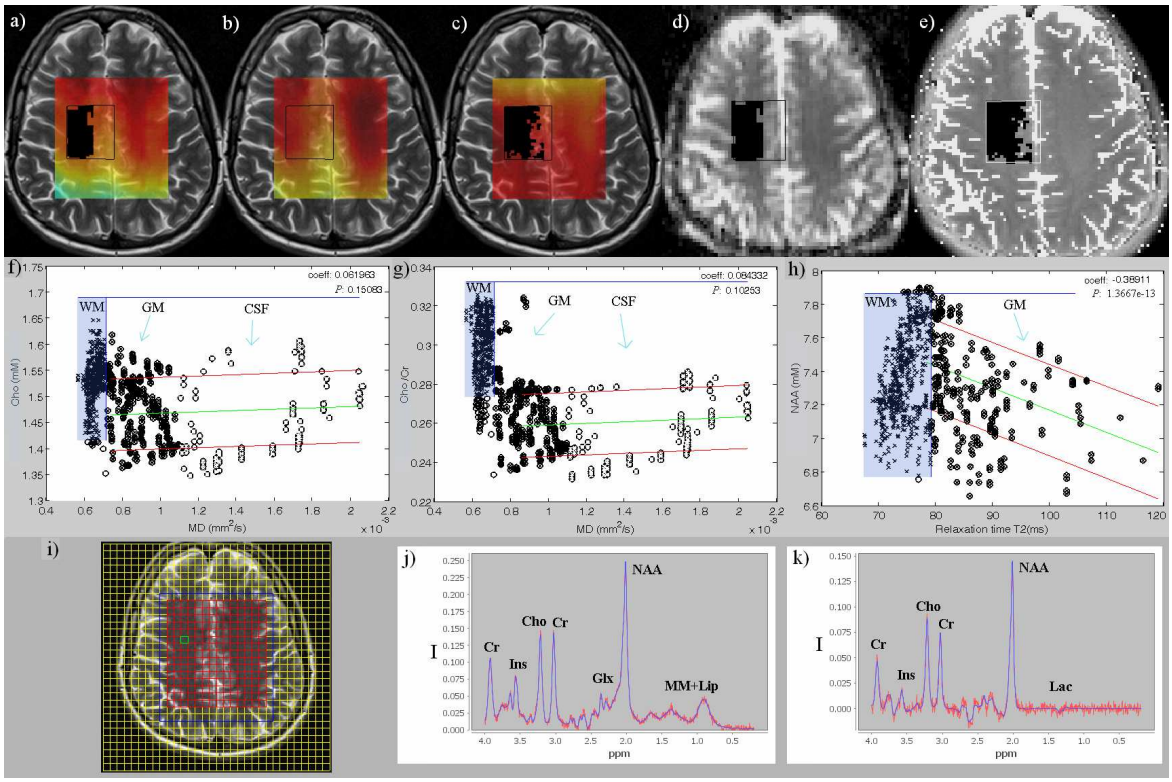

Figure 5.1 The example of data evaluation in a centrum semiovale of a healthy control (42-years old female).
a) A T2-weighted image merged with a Cho map. b) Cho/Cr map. c) NAA map. d) Mean diffusivity map. e) T2 relaxation map. f) Cho-MD correlation. g) Cho/Cr-MD correlation. h) NAA-T2 correlation. i) Spectroscopic grid on MR image. j) Short TE spectrum. k) Long TE spectrum. Both spectra were evaluated from the green voxel marked in the image. a)-c) Used metabolic maps were measured with TE=30ms. i) Data points indicated by a cross in the correlation plots represent an ordered pair of parameter values corresponding to one pixel in the analysed area. Blue lines determine the borders of control data assessed predominantly from WM (i.e., MAX values used for automatic patients' evaluation). Values corresponding to control values are visible as crosses inside the blue area and correspond to black pixels in images a), c), d), e). In healthy controls, crosses in circles correspond to the gray matter and open circles to cerebrospinal fluid. The green lines represent the best linear fit of the data. The red lines indicate the 95% confidence interval for the linear regression fit. Adapted from [106].
GM, gray matter; WM, white matter; CSF, cerebrospinal fluid; Cho, choline-containing compounds; NAA, total N-acetylaspartate; Cr, total creatine; Glx, glutamine and glutamate; Ins, myo-inositol; Lac, lactate; MM+Lip, macromolecules and lipids; T2, T2 relaxation time; MD, mean diffusivity; I, signal intensity.

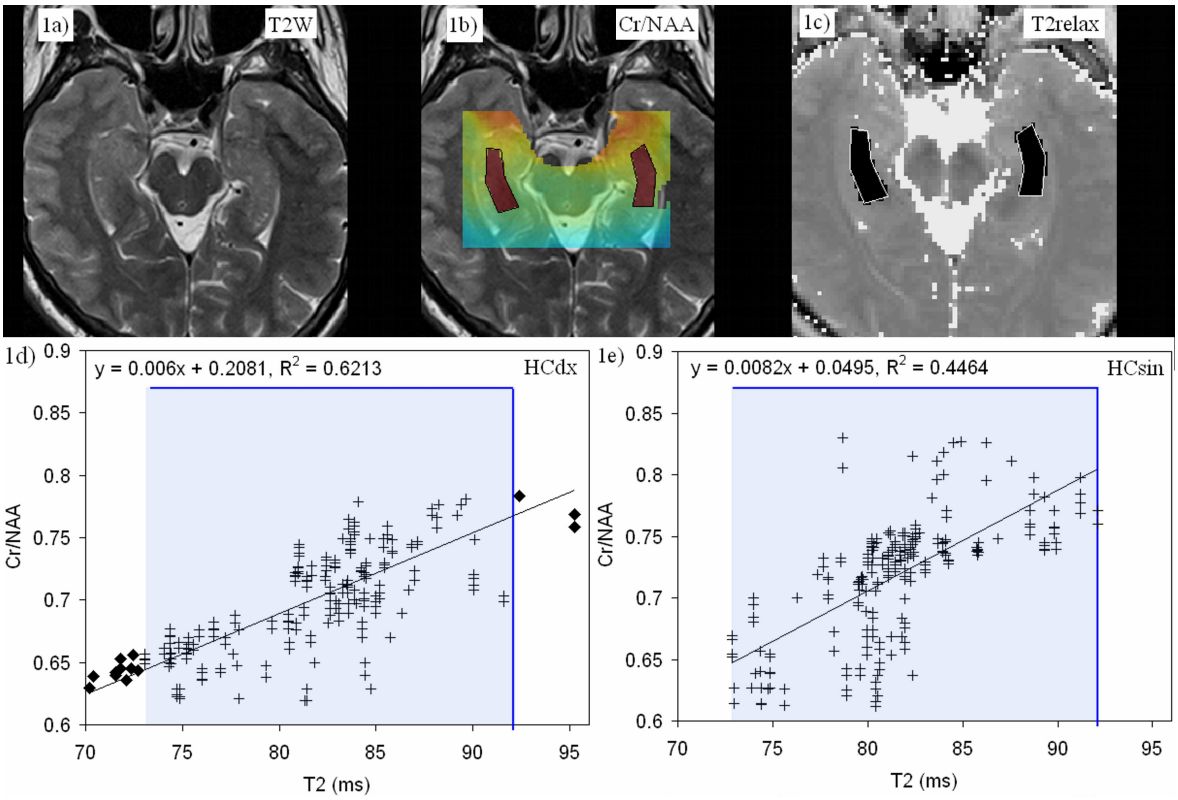

Figure 5.2 The Cr/NAA-T2 correlations in hippocampi in a 24 year-old healthy control (male).
a) A T2-weighted image parallel to the long HC axis. b) Cr/NAA maps positioned on T2W images with the maximal value of the Cramer-Rao bound of total Cr/NAA ratios set to 15%. Measured with TE=135ms. c) T2 relaxation map. b)-c) Red pixels inside the selected area in the hippocampus on Cr/NAA maps (b) and black pixels on T2 relaxation (c) correspond to the healthy tissue according to control data. d)-e) Correlation plots. Each cross represents an ordered pair of Cr/NAA and T2 values corresponding to one pixel in the analysed area. The borders of controls data in hippocampi (see Table 5.1) are visible in correlation plots as blue lines. All the values outside the control interval are visible as diamonds. According to automatic evaluation both hippocampi have normal findings.
T2W, T2-weighted image; Cr, total creatine; NAA, total N-acetylspartate; T2, T2 relaxation time; HCdx, right hippocampus; Hcsin, left hippocampus.

5.2 Patients with Untreated Brain Lesions

Different correlations between metabolic concentrations and mean diffusivity and T2 relaxation times were found at 3T for different lesion localisation as well as for different tumour type. Low grade gliomas, high grade gliomas and lymphomas therefore revealed specific correlation patterns characterising structural and metabolic changes in each tumour type. These patterns are schematically shown in Figure 5.3. The existence of the inverse correlation between Cho and MD in patients with glioblastoma multiforme found at 1.5T were confirmed also at 3T, however, it represented only part of the observed correlation pattern (see Figure 5.3, pattern E). The positive linear MD-T2 correlation was found in

LGG and LYM (Figure 5.3, patterns D, L), not in HGG containing a dense non-enhancing tissue (pattern H). The dense non-enhancing tissue revealed low MD and high T2, meanwhile LGG revealed high MD and high T2 and lymphomas low MD and low T2. More heterogeneous regions such as the basal ganglia, hippocampi, etc. invoked more complicated correlations with the similar correlation trends as in other regions, but with the additional clusters among the standard correlations. The origin of these correlation patterns is based on a different tissue state involved in an examined area, i.e. healthy tissue (region 1), tissue infiltrated by tumourous cells (region 2), active tumour (region 3), tumour infiltrated oedema (region 4), oedema (region 5), etc. Differences of correlation patterns in different directions within one lesion were found. It therefore provided information about the tissue state in selected direction and enabled detection of the direction of primary tumour growing. The correlation patterns for echo times TE=30 and 135 ms were similar. Correlations of the following MR parameters are suitable for tissue differentiation: MD, T2, Cho, N-acetylaspartate, creatine, inositol, lactate, macromolecules and lipids and metabolite ratios. Detailed information about the specific correlation patterns in each tumour type as well as authentic figures and plots drawn by the CORIMA program can be found in the corresponding original papers supplemented in Appendices 1 and 2 and in [2, 106].

Correlations in other lesions differed from those in LGG, HGG and LYM. The following correlation patterns were observed in dysembryoplastic neuroepithelial tumour (DNET): pattern B for NAA-T2 correlation (NAA values below MIN value), the pattern A for Cho/Cr-T2, Cr/NAA-T2, Cho/NAA-T2, Lac/Cr-T2, Ins-T2 (with metabolic values slightly above MAX values). A modified pattern A was observed for Cr-T2 and for Cho-T2, as DNET exhibited decreased Cho values compared to control data.

MD, T2 and all examined metabolites, but NAA and Lac, did not correlate in a patient with leukoencephalopathy. The inverse NAA-MD and NAA-T2 correlations (with NAA values below MIN value) and the positive ones for Lac-MD and Lac-T2 (with Lac values above MAX value) were observed.

Patient no.22 exhibited the same correlation patterns as non-enhancing HGG but without high Cho values. Very low MD and increased T2 were found in the outer part of the lesion, while increased both MD and T2 values in the inner part. It was diagnosed as atypical multiple sclerosis.

Detailed patient information, included results of biopsy or histology, is summarised in Table 5.3.

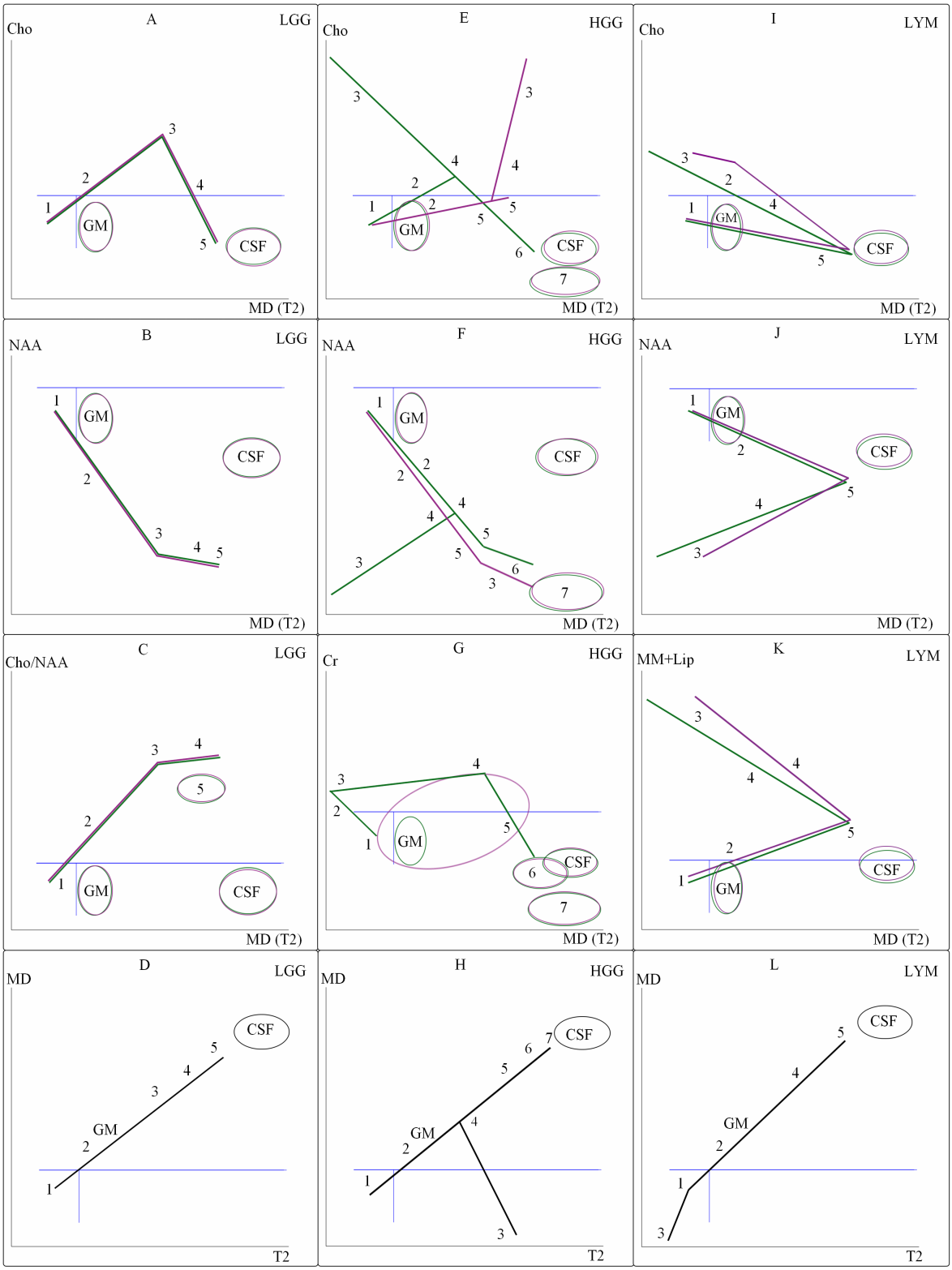

Figure 5.3 Schematic correlations in low grade gliomas (LGG), high grade gliomas (HGG) and lymphomas (LYM). Adapted from [106].
The patterns correspond to correlations in primary brain lesions in individual patients, LGG in the first column, HGG in the second column and LYM in the last column. x-axis represents MD or T2 values, y-axis metabolite values. Blue lines determine the hypothetic borders of the control data (i.e., MAX values used for automatic patients' evaluation). Cho-MD (green), Cho-T2 (violet) correlations are in the first row, NAA-MD (green), NAA-T2 (violet) in the second row. The third row shows correlations Cho/NAA-MD (green) and Cho/NAA-T2 (violet) for LGG, Cr-MD (green)

and Cr-T2 (violet) for HGG, MM+Lip-MD (green) and MM+Lip-T2 (violet) for LYM. MD-T2 correlation for all tumour types is in the last row. Region 1 corresponds to the healthy tissue, region 2 to the transition zone (infiltrative tumour), region 3 to the active tumour, region 4 to the oedema infiltrated by tumour, region 5 to the oedema, 6 to the tumour/necrosis and 7 to the necrosis.
GM - gray matter; CSF - cerebrospinal fluid; Cho - choline-containing compounds; NAA - total N-acetylaspartate; Cr - total creatine; MM+Lip - macromolecules and lipids; T2 - T2 relaxation time; MD - mean diffusivity.

Patients´ number, sex, age	**Treatment before MR**	**Histo patho logical findings**	**Time of MR (months)**	**Time of biopsy after MR (days)**	**Treatment after MR**	**Histopatho logical findings**	**Final lesion classification**
LESIONS WITHOUT TREATMENT							
LGG							
10,m,46	-	-	0	14**	-	PA I	primary
14,f,54	-	-	0	56*	-	FA II	primary
23,f,53	-	-	0	2*	-	FA II	primary
29,f,23	-	-	0	4	ChT	FA II/AA III	primary
30,m,59	-	-	0	1	-	ODG II	primary
31,m,40	-	-	0	2	-	DFA II	primary
32,f,62	1 (biopsy)/-	clear	0	1	-	DFA II	primary
33,f,32	-	-	0	1	-	FA II	primary
34,m,49	-	-	0	1	-	FA II	primary
35,m,60	-	-	0	0	-	GCA II	primary
36,m,39			0	12*	-	ODG II	primary
37,f,21			0	1	-	FA II	primary
38,m,36	-	-	0	1	-	DGCA II	primary
39,m,66	1 (biopsy)/-	FA II	0	-	-	-	primary
HGG							
3,f,52	-	-	0,3,6	5**	RT+ChTp	GBM IV	primary
8,m,53	-	-	0	3*	RT+ChT	GBM IV	primary
20,m,71	-	-	0	-	-	NA	primary
40,f,50	-	-	0	0	-	GBM IV	primary
41,m,46	-	-	0	2	-	GBM IV	primary
42,f,31	-	-	0	1	-	AA III	primary
43,m,46			0	1	-	GBM IV	primary
44,f,59			0	1	-	GBM IV	primary
LYM							
45,f,77	-	-	0	1	-	CLBCML III	primary
46,m,67	corticoids		0	1	-	LBCL	primary
47,m,73			0	1	-	CLBCML III	primary
48,f,67	-	-	0	1	-	ML III	primary
OTHERS							
9,f,67	-	-	0	-	-	DNET	primary
22,m,17	-	-	0	-	-	aMS	primary
27,f,41	-	-	0,3	-	-	PTG	primary
49,m,63	-	-	0	1	-	LEP	primary

TREATED LESIONS - RECURRENCE							
PERI-CAVITY							
3,f,52	15*/RT+ChT	GBM IV	0,3	2*	RT+ChT	GBM IV	recurrence
4,f,60	4**/AT	GBM IV	0,3	82*	ChT	GBM IV	recurrence
6,f,47	31*/-	ODG II	0,6,16	55	RT+ChT	ODG III	upgrading
7,f,45	38*/-	OA II	0,12	7*	-	FA II	residuum
11,f,31	18*/RT+ChT	DG II-III	0,8	-	-	-	residuum
12,f,37	7*/RT+ChT	ODG III	0	-	-	-	residuum
16,f,31	21*/-	OA II	0	-	RT+ChT	-	recurrence
19,m,49	2**/RT	GBM IV	0,7	42*	ChT	GBM IV	recurrence
23,f,53	5*/-	FA II	0	8**	RT+ChT	GBM IV	recurrence
24,m,52	7*/RT+ChT	GBM IV	0	-	ChT	-	recurrence
26,m,46	19**/RT+ChT	GBM IV	0	11**	ChT	GBM IV	recurrence
28,m,68	13**/-	ODG II	0	-	-	-	recurrence
50,m,68	3/RT+ChT	GBM IV	0	-	-	GBM IV	recurrence
51,f,32	4/RT+ChT	GBM IV	0	-	ChT	GBM IV	recurrence
NEW LESIONS							
2,m,65	23**/RT+ChT	GBM IV	0,3	29	ChT	GBM IV	recurrence
13,f,43	7*/RT	AA II	0,4	20	-	GBM IV	recurrence
24,m,52	7*/RT+ChT	GBM IV	0	-	ChT	-	recurrence
TREATED LESIONS - RADIATION CHANGES							
1,m,50	7**/ChT+RT	GBM IV	0,3,6	-	ChT	-	radiation changes
2,m,65	23**/RT+ChT	GBM IV	0,3	-	ChT	-	radiation changes
5,m,55	4/RT+ChT	GBM	0,3	-	-	-	radiation changes
13,f,43	7*/RT	AA II	0,3	-	-	-	radionecrosis
15,m,29	25**/RT+ChT	AA II/III	0,5	1	-	Regressed AA II	radionecrosis
17,m,57	GK 32G	MET	0	-	-	-	radiation changes
18,m,62	1/AT+ChT-T	GBM IV	0	-	-	-	radionecrosis
19,m,49	2**/RT	GBM IV	0,7	-	-	-	radionecrosis
21,m,26	27*/RT	FA II	0	-	-	-	radionecrosis
25,m,48	9**/RT+ChT	GBM IV	0	-		-	radionecrosis
52,f,13	24*/RT+ChT	FA II	0	-	-	-	radiation changes

Table 5.3 Clinical, radiological and oncological characteristics and histopathological results of patients in the tumour study.
MR, magnetic resonance examination; m, male;f, female; LGG, low grade glioma; HGG, high grade glioma; LYM, lymphomas; OTHERS, other lesion type; PA, pilocytic astrocytoma; (D)FA, (diffusion) fibrilar astrocytoma; (D)GCA, (diffusion) gemitocytic astrocytoma; AA, anaplastic astrocytoma; OA, oligoastrocytoma; ODG, oligodendroglioma; DG, diffusion glioma; GBM, glioblastoma multiforme; LBCL, large B-cell lymphoma; CLBCML, centrocytic large B-cell malignant lymphoma; ML, malignant lymphoma; DNET, dysembryoplastic neuroepithelial tumour; aMS, atypical multiple sclerosis; PTG, posttraumatic gliosis; LEP, leukoencephalopathy; MET, metastasis; I, grade I; II, grade II; III, grade III; IV, grade IV; AT, actinotherapy; RT, radiotherapy; ChT, chemotherapy, ChTp, partial chemotherapy, Temozolomide; GK, Gamma knife; *, subtotal resection; **, total resection

5.3 Patients with Treated Brain Lesions

No significant differences in correlation patterns between untreated and recurrent tumour were found. Treated patients exhibited changes in metabolic values with respect to untreated ones, especially significantly lower NAA values. As in untreated brain lesions, more heterogeneous regions such as the basal ganglia, hippocampi, etc. invoked more complicated correlations with the similar correlation trends as in other regions, but with the additional clusters among the standard correlations. Detailed patients' information, included results of biopsy or histology, is summarised in Table 5.3.

5.3.1 Correlations in Tumour Recurrence

The recurrent LGG exhibited the same patterns as untreated LGG (see Figure 5.4). Cho-MD and Cho-T2 correlations showed pattern A (Figures 5.3, 5.4) in the case when the examined region contained recurrent tumour and inverse correlation (with Cho values below MIN) in other cases. Cho values in recurrent LGG tumour were lower than values in untreated LGG. The difference varied between patients and reached a maximum of 30%. Cho values in healthy tissue in peri-cavity region were slightly increased in comparison with control data. The inverse Cr-MD, Cr-T2, NAA-MD and NAA-T2 correlations (with metabolic values below MIN values) and positive one for Cr/NAA-MD, Cr/NAA-T2, Cho/NAA-MD, Cho/NAA-T2, Cho/Cr-MD and Cho/Cr-T2 (with metabolic values above MAX values) were observed. Ins and T2 or MD revealed either pattern A (Figure 5.3) or did not correlate. The positive Lac/Cr-MD and Lac/Cr-T2 correlations (with Lac values above MAX value) were characteristic for directions with tumour recurrence, whereas the other regions did not exhibit any correlation.

Recurrent HGG revealed the same patterns as untreated ones. The patterns E and F (see Figure 5.3) corresponding to a region with a solid tumour were found in certain directions of patient no. 36 only. In other cases Cho, Cr, NAA in combination with T2 or MD exhibited the inverse correlations (with metabolic values below MIN values). Cho/Cr, Cho/NAA, Cr/NAA and Lac/Cr (with metabolic values above MAX values) correlated with T2 or MD positively. Ins and T2 or MD revealed either inverse correlation or did not correlate. No parameter reached the control values in any region.

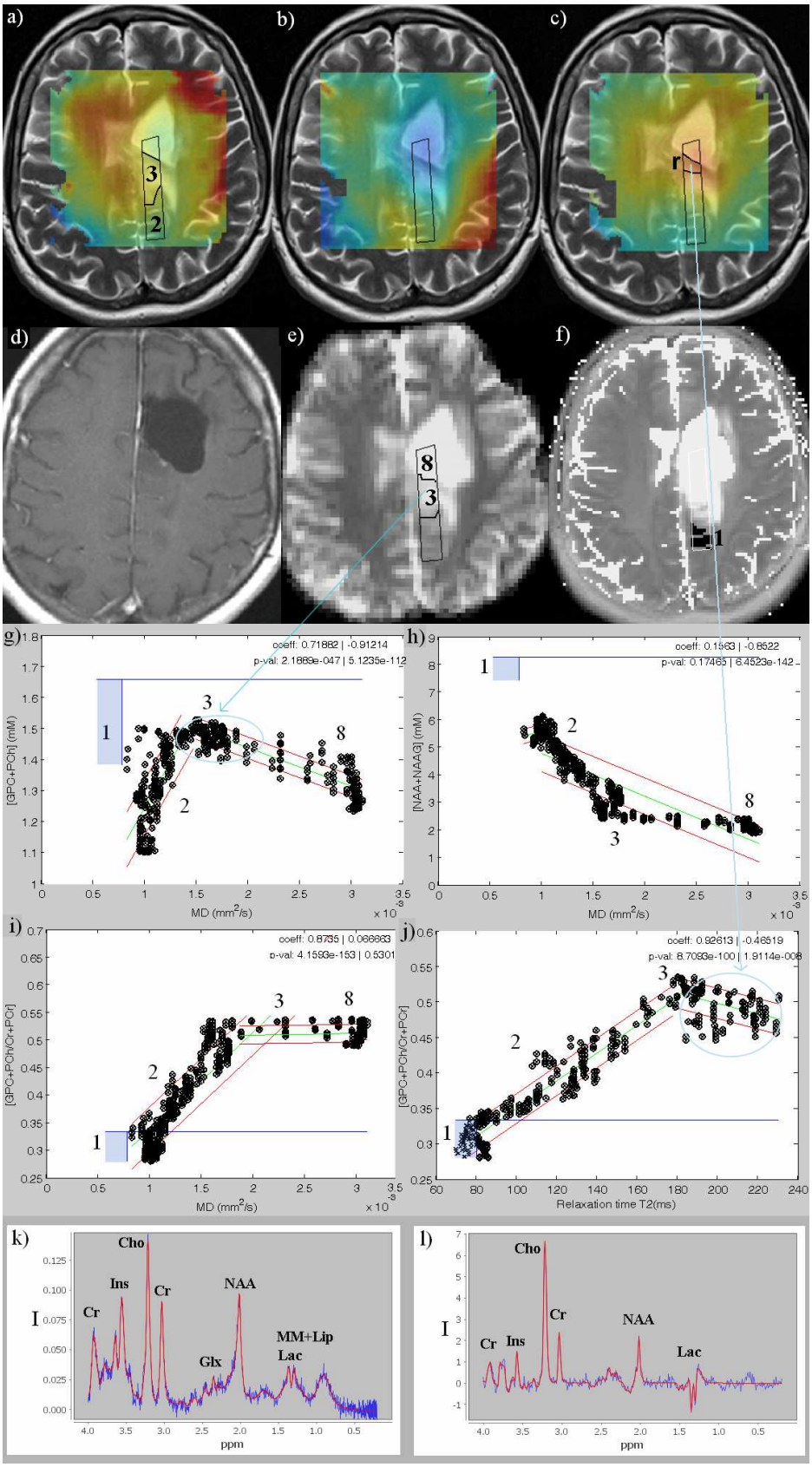

Figure 5.4 The example of correlation patterns in recurrent LGG (patient no.7)
a) Cho map parallelly positioned on the T2-weighted image with a maximum value of the Cramer–Rao bound of Cho set to 15%. b) NAA map. c) Cho/Cr map. d) Contrast-enhanced T1W image. e) Mean diffusivity map. f) T2 relaxation map. g) Cho-MD correlation. h) NAA-MD correlation. i)

Cho/Cr-MD correlation. j) Cho/Cr-T2 correlation. k)-l) Short TE spectrum (k) and long TE spectrum (l) from the resected region. a)-c) Used metabolic maps were measured with TE=30ms. c) Region "r" on the Cho/Cr map show the region consequently resected during the second partial resection of tumour. f) Black pixels inside the selected area on the T2 relaxation map correspond to the healthy tissue according to control data. Data points indicated by a cross in the correlation plots represent an ordered pair of parameter values corresponding to one pixel in the analysed area. Blue lines determine the borders of control data (i.e., MAX values used for automatic patients' evaluation). Values corresponding to control values are visible as crosses inside the blue area and correspond to region 1 on the images. All values outside the blue area visible as crosses in circles correspond to tissue abnormalities. Region 2 represents the transition zone (the infiltrative tumour to the healthy tissue), region the 3 active tumour, region 8 the cavity after the first tumour resection. The findings in region 3 were in agreement with histopathological results. The green lines represent the best linear fit of the data. The red lines indicate the 95% confidence interval for the linear regression fit.
Cho, GPC+PCh, choline-containing compounds; NAA, NAA+NAAG, total N-acetylaspartate; Cr, total creatine; Glx, glutamine and glutamate; Ins, myo-inositol; Lac, lactate; MM+Lip, macromolecules and lipids; T2, T2 relaxation map; MD, mean diffusivity; Cho/Cr, metabolic ratio; r, the resected region during second tumour resection; I, signal intensity.

5.3.2 Correlations in the Tissue Changed by Radio/Chemotherapy

No specific correlation patterns were found in this group. All types of Cho-MD, Cho-T2, Cho/NAA, Cho/NAA-T2, Cr/NAA-MD, Cr-NAA-T2 correlations (positive, inverse or no correlation) were observed, with high Cho/NAA and Cr/NAA values and different Cho levels. Cho values were always lower than in recurrent tumours. Low Cho values were found in radiation necrosis (see Figure 5.5). If apparently healthy tissue and radiation necrosis were involved in the examined region, inverse correlation for Cho-MD, Cho-T2 and positive one for Cho/NAA-MD(T2), Cr/NAA-MD(T2), Lac-MD(T2), Lac/Cr-MD(T2) and MM+Lip-MD(T2) were observed. Cho/Cr-MD and Cho/Cr-T2 exhibited modified pattern C (Figures 5.3, 5.4) with normal or slightly increased metabolic values. Cr, Ins, NAA and MD or T2 either exhibited inverse correlations (with metabolic values below MIN values) or did not correlate.

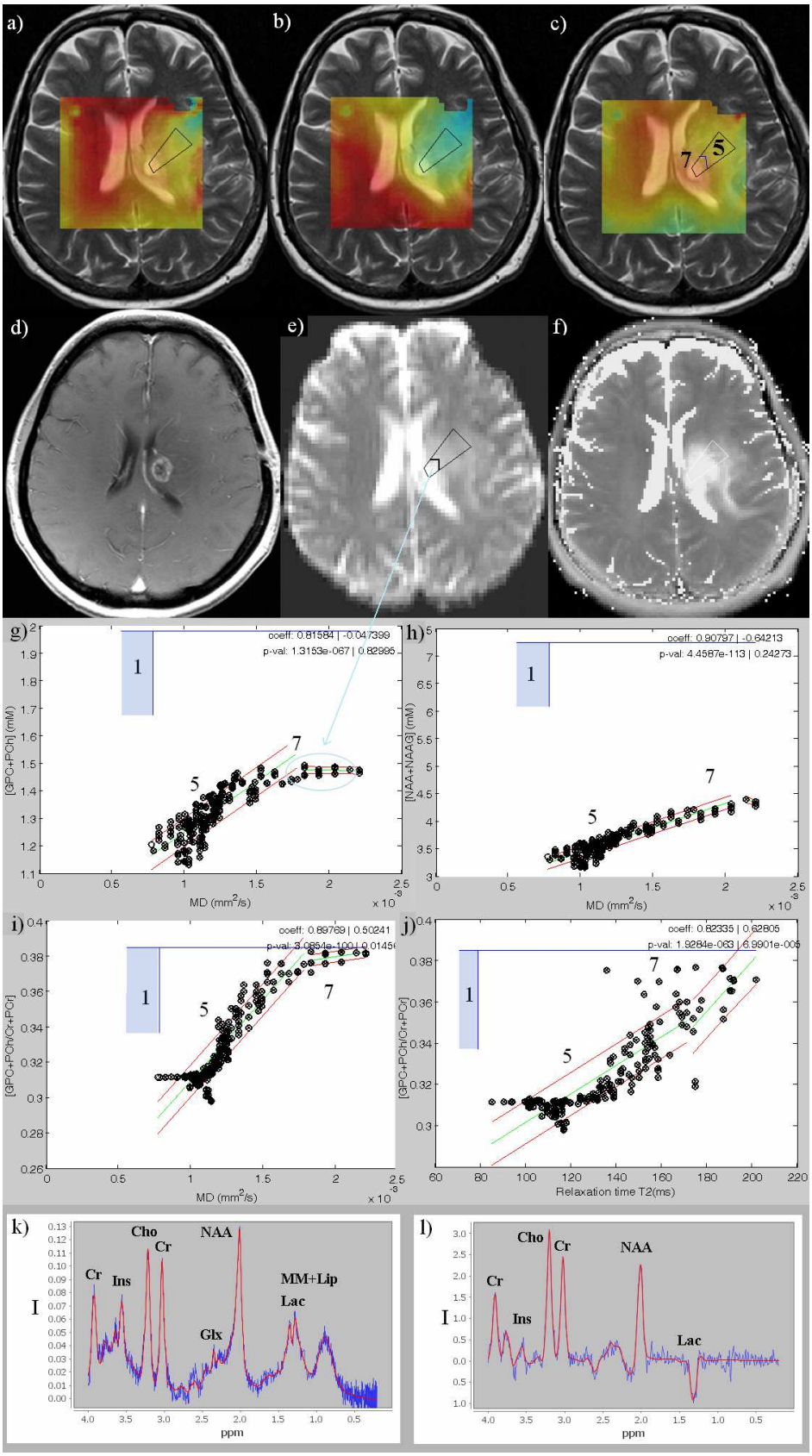

Figure 5.5 The example of correlation patterns in radiation necrosis (patient no.13)
a) Cho map parallelly positioned on the T2-weighted image with a maximum value of the Cramer–Rao bound of Cho set to 15%. b) NAA map. c) Cho/Cr map. d) Contrast-enhanced T1W image. e) Mean diffusivity map. f) T2 relaxation map. g) Cho-MD correlation. h) NAA-MD correlation. i) Cho/Cr-MD correlation. j) Cho/Cr-T2 correlation. k)-l) Short TE spectrum (k) and long TE

spectrum (l) from the lesion. a)-c) Used metabolic maps were measured with TE=30ms. f) Black pixels inside the selected area on the T2 relaxation map correspond to the healthy tissue according to control data. Data points indicated by a cross in the correlation plots represent an ordered pair of parameter values corresponding to one pixel in the analysed area. Blue lines determine the borders of control data (i.e., MAX values used for automatic patients' evaluation). MR parameters did not reach the control values in the selected area. All values outside the blue area visible as crosses in circles correspond to tissue abnormalities. Region 5 represents the oedema, region 7 the radiation necrosis. The green lines represent the best linear fit of the data. The red lines indicate the 95% confidence interval for the linear regression fit. Radionecrosis was confirmed by radiological follow-up.
Cho, GPC+PCh, choline containing compounds; NAA, NAA+NAAG, total N-acetylaspartate; Cr, total creatine; Glx, glutamine and glutamate; Ins, myo-inositol; Lac, lactate; MM+Lip, macromolecules and lipids; T2, T2 relaxation map; MD, mean diffusivity; Cho/Cr, metabolic ratio; I, signal intensity.

5.3.3 MR Spectroscopy Imaging in Neurooncological Practice

Standard voxel based MRS evaluation was used for differential diagnostics between tumour recurrence and radionecrosis. The recurrent tissue always exhibited high Cho and Cho/Cr. Cho and Cho/Cr values were higher in HGG than in LGG. The radionecrosis revealed lower Cho and Cho/Cr values and higher Lac compared to tumour recurrence. Different Cr levels, low NAA and high Cho/NAA were observed in both types of lesions. Spectra from four patients are shown in Figures 5.4 k,l), 5.5 k,l) and 5.6. The Cho/Cr ratio was found the most useful parameter for differential diagnosis between both lesion types. The diagnosis based on MRSI was in agreement with final neuroradiological diagnosis in 83 % of cases. However, in one case the histopathological results confirmed the MRSI diagnosis. Therefore, the sensitivity of MRS reached 85 % and the specificity 91 %. To get the MRSI and histopathological data from the corresponding localisation, the MR images fused with spectroscopic images were used in the neurosurgical navigated systems during stereotactic or open-frame biopsies. The methodology was successfully implemented into the neurosurgical protocol (see Figure 5.7). The comparison between MRSI, oncological and histopathoogical results is shown in Table 5.4.

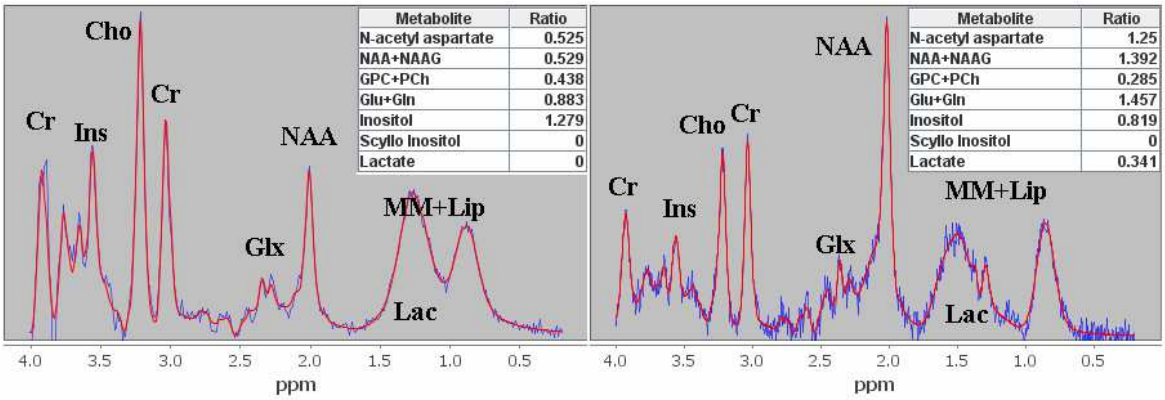

(a) (b)

Figure 5.6 Short echo time spectra a) from recurrent tumour (patient no. 6, ODG III) and b) from the tissue changed by radiation (patient no.2). Tables contain ratios between stated metabolites and total creatine.
Cho, GPC+PCh, choline-containing compounds; NAA, NAA+NAAG, total N-acetylaspartate; Cr, total creatine; Glx, Glu+Gln, glutamine and glutamate; Ins, myo-inositol; Lac, lactate; MM+Lip, macromolecules and lipids; T2, T2 relaxation map; MD, mean diffusivity; Cho/Cr, metabolic ratio.

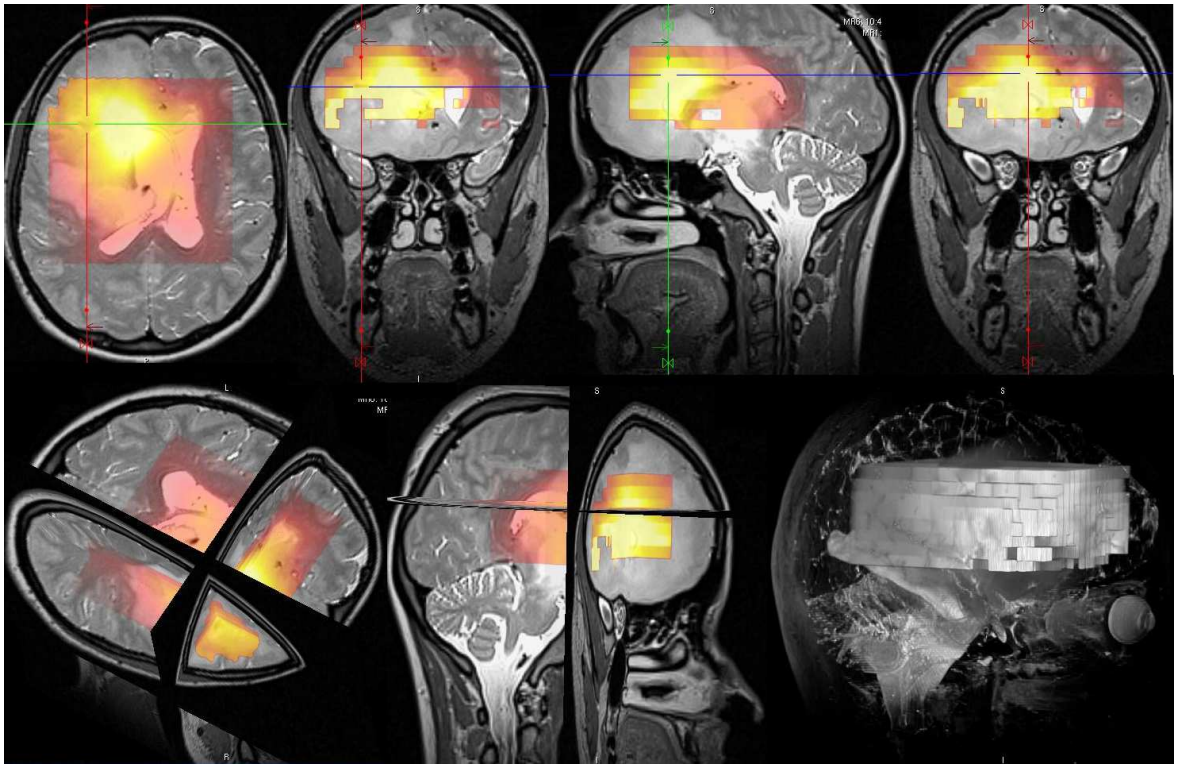

Figure 5.7 The example of 3D MR images merged with 3D metabolic map (N-acetylaspartate) in a navigated system used for a stereotactic biopsy.

Patients´ number, sex, age	MRS diagnosis	Final neuroradiologic diagnosis	Histopatho logical findings
1,m,50	radionecrosis	radionecrosis	-
2,m,65	radionecrosis	radionecrosis	-
2,m,65,*	radionecrosis	recurrence	GBM IV
3,f,52	recurrence	recurrence	GBM IV
4,f,60	radionecrosis	recurrence	GBM IV
5,m,55	radionecrosis	radionecrosis	-
6,f,47	recurrence	recurrence	ODG III
11,f,31	recurrence	residuum	-
12,f,37	recurrence	residuum	-
13,f,43	radionecrosis	radionecrosis	-
13,f,43,*	recurrence	recurrence	GBM IV
15,m,29	radionecrosis	recurrence	Regressed AA II
17,m,57	radionecrosis	radionecrosis	-
18,m,62	radionecrosis	radionecrosis	-
19,m,49	radionecrosis	radionecrosis	-
19,m,49,*	recurrence	recurrence	GBM IV
21,m,26	recurrence	radionecrosis	-
23,f,53	recurrence	recurrence	GBM IV
24,m,52	recurrence	recurrence	-
25,m,48	radionecrosis $^{+}$	radionecrosis	-
26,m,46	recurrence^{++}	recurrence	GBM IV
50,m,68	recurrence	recurrence	GBM IV
51,f,32	recurrence	recurrence	GBM IV
52,f,13	radionecrosis	radionecrosis	-

Table 5.4 The comparison of diagnosis based on MR spectroscopy and neuroradiology. If available, the histopathological results are stated.
MRS, MR spectroscopy; GBM, glioblastoma multiforme; ODG, oligodendroglioma; AA, anaplastic astrocytoma; II, grade II; III, grade III; IV, grade IV; *, patient examined repeatedly; +, incomplete MRS protocol; ++, bad spectra quality

5.4 Patients with Temporal Lobe Epilepsy

EEG, electro-clinical, correlation and histopathological features for each patient are listed in Table 5.5.

Correlations of metabolic data with MD and T2 were calculated for both the control and patient groups. In both groups MD and T2 revealed positive correlation. MD, T2, Cho, Cr/NAA, Cho/Cr, Cho/NAA gradually decreased and NAA gradually increased in the anteroposterior direction of the hippocampus in all subjects (see Figure 5.8), although the slopes differed between patients and controls.

Patient No., sex	Age/ epilepsy duration (years)	EEG	Electro-clinical diagnosis	MRI finding	MRS-MD lateralisation	MRS-T2 lateralisation	Histo pathological findings
1,m	32/14	T sin	TLE sin	non-lesional	HC sin	HC sin	no surgery
2,f	34/19	T sin	TLE sin	non-lesional	HC sin	NA	no surgery
3,f	35/21	T bilat (sin)	TLE sin	non-lesional	HC bilat (sin)	NA	no surgery
4,m	20/6	T sin	TLE sin	non-lesional	NA	HC bilat (sin)	normal
5,f	19/12	T dx	MTLE dx	non-lesional	HC dx	HC dx	FCD 1B
6,m	40/14	T sin	MTLE sin	T2W increased signal in left T pole	HC bilat (sin)	HC bilat (sin)	FCD 2A, HC non-specific gliosis
7,f	41/23	T bilat (sin)	MTLE sin	T2W increased signal in left PHG	NA	normal HCdx*	FCD 1B, HC non-specific gliosis
8,f	18/8	T dx	MTLE dx	HS dx	HC bilat (sin)	HC bilat (dx)	isolated HS
9,m	20/7	T dx	MTLE dx	HS dx	HC dx	HC dx	isolated HS
10,f	20/15	T bilat (sin)	MTLE sin	HS sin	HC bilat (sin)	HC sin	isolated HS
11,f	18/14	T bilat (sin)	MTLE sin	HS sin, T2W increased signal and atrophy in T pole	HC sin	HC bilat (sin)	HS, FCD 1A
12,m	41/9	T dx	MTLE dx	HS dx	HC bilat	HC bilat (dx)	HS, FCD 1A
13,f	15/11	T sin	MTLE sin	HS sin, T2W increased signal and atrophy in T pole	HC sin	HC sin	HS, FCD 1B
14,m	32/3	T bilat (sin)	MTLE sin	HS sin	HC bilat (sin)	NA	HS, FCD 1B
15,m	18/6	T sin	MTLE sin	HS sin, T2W increased signal and atrophy in T pole	HC sin	HC sin	HS, post-inflammation gliosis
16,m	57/10	T bilat (dx)	MTLE dx	HS dx	HC bilat (dx)	HC bilat	HS, post-inflammation gliosis
17,m	53/37	T sin	MTLE dx	HS dx	HC bilat (dx)	HC bilat (dx)	no surgery
18,f	34/34	T bilat (dx)	TLE dx	HS dx	NA	HCdx	no surgery
19,m	27/20	T dx	MTLE dx	T2W increased signal in right amygdala, PHG and HC	NA	HC bilat (dx)	complex malformation of HC, FCD 2B
20,f	18/1	T dx	TLE dx	right basal posterior temporal tumour	HC dx*	NA	ganglioglioma, FCD 1A

Table 5.5 Demographic, clinical, radiological, correlation and histopathological data of all patients. Only hippocampi were examined in the MRS-MD and MRS-T2 correlations. MRS, magnetic resonance spectroscopy; MD, mean diffusivity; T2, T2 relaxation time; m, male; f, female; dx, right; sin, left; T, temporal lobe; PHG, parahippocampal gyrus; T bilat, bilateral interictal discharges (more than 10%); bilat (dx), bilateral pathology with the right side predominance; bilat (sin), bilateral pathology with the left side predominance; (M)TLE, (mesial) temporal lobe epilepsy; T2W, T2-weighted images; HS, hippocampal sclerosis; HC, hippocampus; WM, white

matter; MCD, malformation of cortical development; FCD, focal cortical dysplasia (classification according to Palmini et al.); NA, not available; *, data from HC sin not available.

5.4.1 Correlations in Non-lesional Epilepsy

Correlations found in HC with normal metabolic values corresponded to those in controls. Correlations in the HC with abnormal metabolic values are listed in Table 5.6. In contrast to controls, Cr and T2 (or MD) correlated positively, whereas Cho/Cr with T2 (or MD) did not correlate. The others correlations were similar to those in controls, but the slopes of MRS-T2 dependence were significantly higher in patients than in the controls ($p<0.05$). The difference is caused by substantial metabolic changes in patients, as the T2 and MD values are within the control intervals.

The semiautomatic evaluation based on control data lateralised all the cases in accordance with the electro-clinical results or histopathologic ones, provided the data were available (see Table 5.5).

Detailed information and the examples of Cr/NAA-T2 correlations can be found in Manuscript supplemented in Appendix 3.

5.4.2 Correlations in Lesional Epilepsy

HC with normal metabolic values and normal MRI findings revealed the same correlations as those in controls. Correlation patterns found in the HC with abnormal values are listed in Table 5.6. In contrast to controls, Cr and T2 (or MD) correlated positively. Although we found no correlation of Cho/Cr and T2 (or MD) in patients with non-lesional TLE, lesional TLE patients revealed positive correlation similar to that found in controls. Other correlation patterns were similar to the non-lesional TLE patient group and control group. The slopes of the MRS-T2 correlations differed significantly from the controls ($p<0.05$), but not from the non-lesional patients.

Histologically proven HS and gliosis exhibited increased T2 values compared to healthy controls; however, other lesions exhibited even more T2 increment.

Electro-clinical diagnosis (4^{th} column in Table 5.5) and the semiautomatic evaluation based on control MRS-T2 data (7^{th} column) lateralised EZ identically in all unilateral cases and the predominance in all bilateral cases. The results were confirmed by histopathology. MRS-T2 combination revealed bilateral changes in seven cases compared to five assessed by EEG (3^{rd} column). However, they concurred only in two cases.

The results of the semiautomatic evaluation based on control MRS-MD data (6th column) corresponded to electro-clinical diagnosis (4th column) in all unilateral cases and the predominance in five out of the seven bilateral cases. Histopathology confirmed these findings. MRS-MD data determined seven bilateral cases compared to four assessed by EEG (3rd column). However, they agreed only in three cases.

Detailed information can be found in Manuscript supplemented in Appendix 3.

	Controls	Non-les HC	Les HC
MD-T2	P	P	P
Cho-T2 (MD)	P	P	P
Cr/NAA-T2 (MD)	P	P	P
Cho/Cr-T2 (MD)	P	Ø	P
Cho/NAA-T2 (MD)	P	P	P
NAA-T2 (MD)	N	N	N
Cr-T2 (MD)	Ø	P	P

Table 5.6 Correlations between selected parameters in controls and abnormal hippocampi.
Correlations with T2 and MD revealed the same patterns.
Non-les HC, non-lesional hippocampus; Les HC, lesional hippocampus; MD, mean diffusivity; T2, T2 relaxation times; Cho, choline containing compounds; Cr, total creatine; NAA, total N-acetylaspartate; P, positive correlation; N- negative correlation; Ø, no correlation.

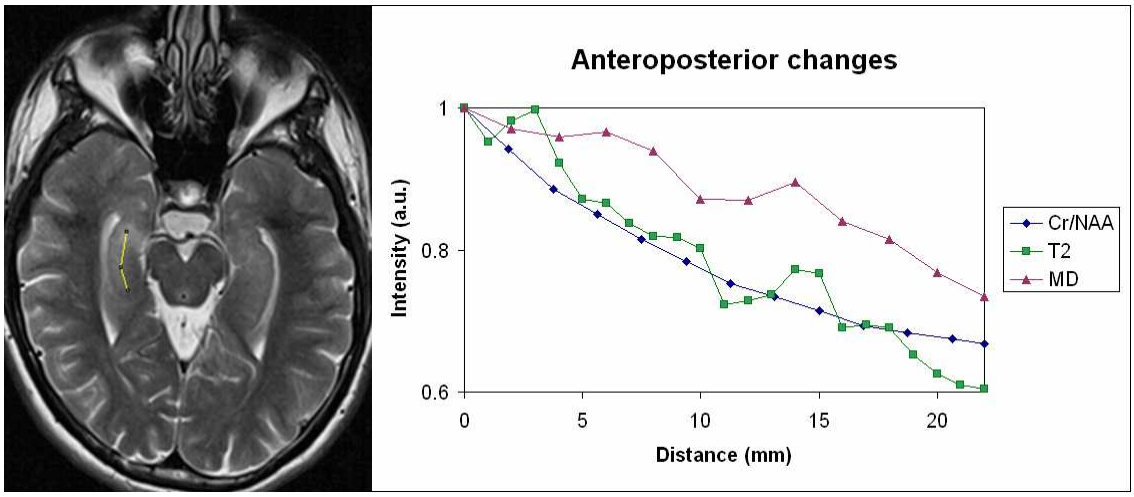

Figure 5.8 MR parameter changes in anteroposterior direction of right hippocampus in a patient with right hipppocampal sclerosis.
Changes of Cr/NAA, T2 and MD are shown along a yellow line highlighted in the T2-weighted MR image. Intensities were normalised to the highest value of each parameter.
Cr, total creatine; NAA, total N-acetylaspartate; T2, T2 relaxation time; MD, mean diffusivity.

6 Discussion

The results of each study and technical issues are discussed in this section. It is divided into three subsections. The first subsection analyses the main technical effects influencing the data evaluation by the proposed correlation method. The second subsection then discusses the main findings in the studies of brain lesions and the third one those in the study of temporal lobe epilepsy. The text concerning the studies of brain lesions is an extended version of the discussion in a published original paper [106, Appendix 2], namely "*Quantitative MR imaging and spectroscopy of brain tumours: a step forward*?" written by the author of the thesis. The text concerning the study of temporal lobe epilepsy is a modified version of the discussion in manuscript entitled "*The use of correlations between quantitative MR parameters for assessment of hippocampal involvement in temporal lobe epilepsy*" supplemented in Appendix 3.

6.1 Technical Effects Influencing the Results

Although quantitative data analysis seems to be a promising tool, a collection of data from different MR methods is linked to a series of difficulties which may influence the results (chemical shift artefact, partial volume effect, diffusion image distortions, bad spectra quality, etc.).

The major problem at 3T represents an unavoidable chemical shift artefact affecting the metabolic images. We tried to reduce its influence by changes in dimensions of the excitation volume. Firstly, a sequence with "Fully Excited VOI" was used for automatic extension of the excited VOI, but it suffered from several problems which caused very low spectra quality. The first was that VOI was larger or almost the same as FOV, so the folding artefact affected the spectra, the second was that the automatic suppression of signal of scalp subcutaneous lipids implemented in the sequence was insufficient. Consequently, this functionality was omitted and a manual assessment of larger VOI was tested (described in Section 4.2.3 and shown in Figure 4.1). Although special attention was paid to the positioning of saturation bands to effectively suppress the signal of scalp subcutaneous lipids, the lipid signal in short TE was always higher in comparison with the normal excitation VOI size. Despite the fact that the CSA did not fully diminish in anteroposterior direction, the good spectra quality and significant CSA suppression was achieved by using these modifications and the manual shimming. Moreover, voxels with

bad spectra quality were omitted from the correlation analysis by a special function in CORIMA program enabling it to exclude all voxels with corresponding Cramer-Rao bounds greater than the assigned threshold.

Another source of bias in the calculated correlations was an inherent sensitivity of echo planar imaging sequences (used for the acquisition of diffusion images) to inhomogeneities of the static magnetic field manifesting as distortions in the image. With respect to this, the use of a multi-channel head coil allowing the reduction of the echo planar imaging readout period using parallel imaging techniques would be beneficial. Unfortunately, since the spectroscopy measurements were designed for a transmitter-receiver head coil, parallel techniques could not be used in this study. Increased image distortions in the image plane containing both temporal and facial regions could be corrected during images post-processing using the additional B0 map [29]. However, the acquisition of the B0 map was not feasible due to time constraints.

The correlations with relaxation times were affected by artificial high relaxation values in pixels corresponding to CSF, cavities after tumour resection or cysts. In these areas the fitting algorithm in processing ViDi program [35] failed to converge due to an excessively long relaxation time (usually T2 higher than 300 ms) and therefore artificial relaxation values were set to these pixels. Therefore, a special function was incorporated in the CORIMA program enabling manual exclusion of these pixels. 32 echoes used in T2 relaxation measurements represented the best compromise between data quality and measurement time for the given study purposes. It should be noted that if the relaxation times of CSF, cavities or cysts were matter of interest, a longer TE should be adjusted or more than 32 echoes acquired.

Correlations were tested in both long and short TEs. The metabolite quantification in short TE spectra was difficult in some cases because of the complicated baseline shape, especially in the peri-cranium regions containing high lipid signals. On the other hand, relaxed metabolites such as Ins, Gln and Glu represent the major disadvantage of the acquisition of long TE spectra. Therefore, several different TE were tested to find optimal TE value, but neither TE = 70 ms nor 80 ms solved the problem. Finally, either TE = 30 or 135 ms represented the best choice according to the examined region. The metabolite concentrations were not corrected for relaxation because it was not necessary for the proposed semiautomatic evaluation and the assessment of exact absolute concentrations was not the aim of the study. Moreover, as Weis et al [109] previously pointed out, a more significant source of quantification errors is the concentration of water reference. Proton

density in tumours can be increased by 25% compared to the healthy brain tissue which may result in underestimation of metabolite concentrations.

The mathematical simulations on model images [2, 105] revealed that the partial volume effect can influence the slope of estimated correlations, but cannot artificially create them.

6.2 Brain Lesions Studies

The combination of different MR methods and their quantification has the potential to increase the specificity of diagnosing of tumourous tissue and tumour grading as each MR parameter represents distinct phenomena [3, 56]. The existence of a significant inverse correlation between Cho and MD calculated from measurements on different subjects at 1.5T [5, 37, 108] was confirmed in individual patients analysed on a pixel-by-pixel basis at 1.5T [2, 3, 56, 105]. These studies further proved that the combination of parameters helps to distinguish the different states of pathologic tissue in individual patients with glioblastoma. The results of patients with LGG were not so uniform. The positive, but also, the inverse Cho-MD correlations were found in LGG. The present tumourous study summarises and compares the mutual relationships between MR parameters based on a pixel-by-pixel image evaluation in patients with primary LGG, HGG, LYM, recurrent lesions and radiation necrosis in the magnetic field 3T.

The presented semiautomatic method was based on a correlation analysis [2] which presumed that there is no correlation between different parameters in healthy controls at 1.5T. Contrary to this, we found (at 3T) that correlations depended on the examined region. This discrepancy is caused by lower metabolite values and higher MD and T2 in GM and CSF compared to WM at 3T, whereas the previous study [2] revealed the same metabolite values in GM, WM, and CSF. However, neither MR parameter dispersion nor the correlation slopes in a healthy area reached the values found in pathologic tissue. The discrimination of the tissue based on the MAX and MIN values derived predominantly from white matter may fail even in healthy controls in other tissues (see Figure 5.1). The method is therefore reliable in WM; however, the possible contribution of GM and CSF needs to be verified by a radiologist and the method should be considered as semiautomatic only [106].

The correlations patterns between metabolite values and T1 relaxation times corresponded to those with T2. Therefore T1 relaxometry was consequently left out from the measurement protocol and only T2 relaxometry was performed.

The set of different correlations described above should be considered as a whole. Metabolite maps with short and long TE were used in correlation analysis, however, no significant differences in correlation patterns were found. The results showed that the absolute metabolic concentrations are not necessary for the proposed method. Although the combination of MR parameters often creates complicated correlation patterns, their analysis provides unique information about the abnormal tissue and the pathology extent. Our method is based on the fact that although tissues in different conditions may reveal similar values in individual parameters, they create separated characteristic clusters in the correlation plot which consequently enables their differentiation [106]. For example, oedema infiltrated by tumour exhibits the same MD as oedematous tissue, but it is located in a different part of the correlation plot due to increased choline values caused by tumour proliferation. Conversely, tumour infiltration has the same Cho values as oedema infiltrated by tumour, but as both exhibit a different tissue structure revealed by MD, they belong to different clusters. Previous studies reported the use of Cho-MD correlations for tissue differentiation; however, we found that even a combination of these two parameters was insufficient. The differentiation of healthy GM, CSF, tumour and oedematous tissues fails as long as only Cho-MD correlations are used [106]. They show similar patterns, especially in LGG and LYM. This uncertainty can be overcome by using the NAA-MD, NAA-T2 correlations as NAA is significantly higher in GM than in lesions (see schematic Figure 5.3, patterns B, F, J or authentic ones in the original paper supplemented in Appendix 2). Areas surrounding HGG may exhibit increased or unchanged Cr and the same MD and T2 values compared to healthy GM and/or CSF. We, as well as Oh [4], hypothesise that it could be oedema infiltrated by tumour which shows the same patterns as healthy GM, but it could be also the influence of the partial volume effect which changes metabolite values in pure oedema.

The oedematous regions were characterised by a positive MD-T2 correlation. Oedema exhibited higher relaxation values than tumourous regions (region 3 vs. 4 vs. 5 in Figure 5.3 and Figures 1-4 in the original paper in Appendix 2 or in [106]). The increased water content in the extracellular space in those regions is the result of reactive changes of the normal brain tissue in response to the tumour. Oh [4] concluded that quantitative T2 values may distinguish pure vasogenic oedema from infiltrative tumour, which is in agreement with our results. Only moderately increased MD and T2 values in region 2 may be caused by an emerging vasogenic oedema in response to the presence of tumourous cells (proved by increased Cho). This explanation corresponds to [54], which found normal levels of

anisotropic diffusion, but abnormally high isotropic diffusion (MD) in the region between the tumour mass and normal brain.

The results proved uneven tumour growth (see numbered paragraphs in Results of the original paper [106] enclosed in Appendix 2). Correlation patterns reflect the heterogeneity of the tissue in the ROI, so the ROI should be placed to cover the tissue from the tumour centre across its vicinity as well as the distant healthy tissue. If all tissue subtypes are incorporated in the selected ROI, correlation patterns correspond to the patterns in Figure 5.3. When the ROI has different size or is placed in different direction, only part of the patterns of Figure 5.3 may be observed according to the tissues involved (see Figures 1-3 in the published original paper [106] enclosed in Appendix 2).

Specific metabolic profiles characterising tumour types are known [19, 40, 43], nevertheless, the possibility of tumour grade prediction was controversial. We discovered that different tumour types exhibit specific correlation patterns (Figure 5.3). Although individual correlations cannot predict the grade of the tumour, we hypothesise that the following combinations enable their grading: Cho-MD, Cho-T2, Cho/Cr-MD, Cho/Cr-T2, Ins-MD, Ins-T2, Lac/Cr-MD, Lac/Cr-T2 for long TE, or Cho-MD, Cho-T2, Cho/Cr-MD, Cho/Cr-T2, Ins-MD, Ins-T2, MM+Lip/Cr-MD, MM+Lip/Cr-T2 for short TE.

LGG showed positive MD-T2 correlations which mean an increased extracellular space and subsequently an increased amount of free water [4, 43, 110]. A similar behaviour (increase of MD and T2) was observed in the contrast-enhanced HGG; however, in this case, we suppose that an increase of MD and T2 might be caused by necrotic changes in the tissue (i.e., increased water mobility), which would correspond to the observed contrast enhancing [111].

A dense non-enhancing tissue in the proximity of HGG exhibited low MD and high T2 values, so it is characterised by different correlation patterns. We therefore hypothesise that the high cellular tumour shrinks extracellular space (leading to low MD) because of an increase in tumour cellularity and causes a cellular swelling leading to increased water content in intracellular space (and increase of T2) [58, 112, 113]. However, if an oedema occurs, decreased MD caused by putative high tumour cellularity is not observable [112].

MD lower than the MIN values and normal T2 observed in LYM could be a sign of a shrunk extracellular space and a small amount of free water [114]. Although Guo [115] observed significantly lower MD and higher cellularity in LYM compared to HGG, we found no significant differences in MD. However, they differ in Cho: the more aggressive HGG exhibited high Cho values, while LYM revealed values similar to the healthy tissue.

Stereotactic biopsy independently localised in region 3 and 6 confirmed the automatic assessment of these regions as a tumourous tissue and a necrotic tumour respectively in each patient (Figures 1-3 in the published original paper [106] supplemented in Appendix 2). Stereotactic biopsy (SB) navigated by merged spectroscopy and MR images enabled aiming at the regions with the most significantly changed parameters and precisely compared correlation and histopathologic results. Moreover, spectroscopy navigated SB played an important role in cases with multiple lesions. It helped to localise the most proliferative lesions and therefore prevented patients from the multiple biopsies.

Different tumour types also revealed characteristic spectroscopic profiles. High Cho, Lac and low NAA in HGG is caused by aggressive tumour proliferation and cell and neuronal disruption, whereas slightly increased Cho and Ins and moderate NAA are signs of tumour proliferation, glial changes and decreased neuronal activity [39, 40, 43]. The LYM reveals high MM+Lip produced by free fatty acids caused by cell membrane degradation and moderately increased Cho and low NAA, which are signs of tumour proliferation and neuronal damage.

The parameter values found in DNET corresponded to previously reported studies, however, no study dealt with correlations in patients with DNET. Similar to our study, Bulakbasi et al [116] reported high MD values in DNET. Reduced NAA and elevated Lac in leukoencephalopathy are features of neuronal and mitochondrial dysfunction of any aetiology [117]. The special parameter values in patient no.22 were attributed to atypical multiple sclerosis; however, at present the histopathologic results are not available.

The correlation patterns found in patients treated by chemo/radiotherapy were similar to those found in untreated brain lesions, but the MR parameter values were changed, especially the spectroscopic ones. Normal appearing healthy tissue (NAHT) in the peri-cavity region always exhibited very low NAA values. Most probably it may be attributed to chemo/radiotherapy as well as PVE from the resected cavity. Therefore, neither NAA values nor ratios with NAA are reliable predictors of pathologies in these patients, as Kamada et al [68] also pointed out. As Cr is not as sensitive to therapy as NAA, we agree with other studies [64, 66] that Cho/Cr, Lac/Cr and/or MM+Lip/Cr are more specific in cases of treated brain lesions. Furthermore, it should be noted that correlations with MM+Lip/Cr depends on the examined area. As we have already discussed in Section 5.2, lesions close to cranium exhibited high MM+Lip values caused by PVE of subcutaneous lipids. Therefore, we recommend using the sequence with long TE and using only Cho/Cr and Lac/Cr ratios for reliable differential between tumour recurrence and radiation

necrosis. Negative Cho-MD, Cho-T2 correlations were signs of radiation necrosis due to moderately increased Cho without MD or T2 changes and decreased Cho with increased MD and T2 values. Moderately increased Cho values found in NAHT could be explained by Cho release from membranes damaged by radiation [67]. The positive correlations in tumour recurrence were caused by high Cho and Cho/Cr values in regions with high MD and T2 values. High proliferation in tumour recurrence was characterised by high Cho and Cho/Cr values, whereas we suppose that decreased Cho in radiation necrosis reflects a reduced cellular population.

As standard voxel-based spectroscopic evaluation is not so time consuming, it was found to be the method of choice in differential diagnosis between radiation necrosis and tumour recurrence. However, if the pathology extent is a matter of interest, the correlations represent a unique method for tissue differentiation. In this study, three cases out of 24 were poorly diagnosed. Patient no.4 had been examined repeatedly by MRS and the results were in accordance to long-term radiological monitoring and a good patient outcome. However, the deterioration of the patient's health 3 months later lead to an additional MR examination showing rapid tumour progression compared to the examinations at 3 and 6 months before. Unfortunately, the MRSI examination was not executed this time and an exact comparison with histopathological results was not possible. Therefore, the long-term difference between MRSI and histopathoogical result can explain the different diagnosis. However, we do not have an explanation for the normal metabolite values in patient no.2 confirmed as GBM IV. Histopathological results in patient no.21 are not at our disposal at the moment. Therefore, our results show that MRS is not always sufficiently sensitive for a differential diagnosis between tumour recurrence and radiation necrosis.

Although quantitative data analysis seems to be a promising tool, a proposed method cannot be used completely routinely. Correlation patterns can be influenced by phenomena mentioned in Section 5.1. Diffusion image distortions as well as bad spectra quality can significantly change the mutual relationships. Therefore, this method should be used only in a semiautomatic mode.

6.3 Study of Temporal Lobe Epilepsy

MR spectroscopy and other quantitative MR techniques are widely used in the lateralisation of temporal lobe epilepsy and their clinical value has been recognised. However, their potential is much bigger. This study tested the mutual relationships

between MR parameters based on a pixel-by-pixel image evaluation in patients with TLE and the use of the technique in the assessment of hippocampal involvement.

Evaluation of quantitative MR parameters is extensively used for confirmation of TLE lateralisation before possible surgical planning. Lateralisation using standard EEG is not sufficient and often contradicts results of both electro-clinical diagnosis and results based on MRS-MD MRS-T2 correlations (see Table 5.5). However, correctness of the approach using quantitative MR parameters is validated by agreement of MRS-T2 (MD) data and electro-clinical diagnosis and, if available, by histology.

Single voxel spectroscopy over the larger volume of the hippocampus may be sufficient for basic lateralisation [95, 118]. Nevertheless, the existence of correlation requires comparing the patients' data and controls in the same part of HC [119]. As the values of metabolite concentration or T2 and MD gradually change in the anteroposterior direction, standard statistical methods based on a comparison of average values of measured parameters fail in a more detailed description of the hippocampus which leads to a substantial data dispersion related to physiological properties of the tissue. Therefore, the correlations may better describe the relation between the parameters and physiology and provide important additional information related to pathology extent [81, 85, 102] which also confirmed this study.

In fact, the slopes of the correlations are crucial for assessment of the changes in the tissue and differentiation between patients and controls. Statistically significant differences of MRS-T2 slopes between patient and control groups were found, although the correlation slopes did not differ between non-lesional and lesional TLE. The higher slopes in the case of positive correlations and smaller in negative ones were found in hippocampi which revealed distinctive metabolic changes while the T2 values did not differ from the control data, especially in TLE patients with no MRI finding.

The hippocampi in the case of lesional TLE often showed distinctive T2 changes together with small metabolic changes resulting in small slopes in positive correlations and high in negative ones. Therefore, we suppose that the slope provides information about the significance of metabolic and structural changes in the pathologic tissue.

Mutual relationships between studied parameters in healthy HC in controls revealed gradual changes in individual parameters in the anteroposterior direction of the hippocampus providing additional information about spatial distribution of these parameters across the hippocampus (see Figure 5.8). The relationships followed linear dependence. However, the positive correlations in patients with non-lesional TLE seem to

contain more than one component or a non-linear one (see Figure 1 image 2d in Appendix 3), demonstrating distinctive metabolic changes in the anterior portion of hippocampus. Pixel-by-pixel image analysis therefore represents useful technique for presurgical planning, especially in those patients with negative MRI findings.

Different metabolic concentrations found in anteroposterior direction are in agreement with previously reported studies performed at 1.5T [119, 120]. Unfortunately, we cannot distinguish the contribution of CSA and hippocampal morphology (i.e., tissue changes in anteroposterior direction) to the correlations found in healthy controls. Although CSA may be negligible at 1.5T, it represents a significant contribution to correlations at 3T (even after its minimisation described in Section 4.2.3 and shown in Figure 4.1). However, although CSA represents a possible systematic error, both control and patients' data are affected in the same direction. Therefore, in mutual comparisons, CSA has no relevant effect on the results. Consequently, we assume that the correlations with diverse slopes found in patients are caused by pathological hippocampal changes which was proven by histopathology in patients after surgery.

Significant MD-T2 correlations have been found in all studied groups, in accord with the previous results [85]. We suggest that these modalities do not represent independent parameters, which is not surprising because the two phenomena are mutually related. The diffusion measurements are weighted by relaxations and vice versa. Then again, the correlations with relaxation times were found more precise for assessment of hippocampal involvement, especially because of distortions in diffusion images (discussed in Section 6.1).

Higher T2 relaxation times found in the anterior compared to the posterior portion of the control hippocampus reflect different morphology in each part which is in accord with the previously reported studies [93, 94, 121]. The T2 relaxation times on 3T in healthy controls corresponded to T2 values reported in [121], although they were significantly lower than values reported in [93, 94]. Nevertheless, von Oertzen pointed out that their method (dual-echo TSE sequence) resulted in higher T2 values than those measured by conventional relaxometry.

HS was characterised by increased T2 relaxation times reflecting hippocampal gliosis. Complex hippocampal malformation associated with FCD 2B exhibited even higher T2 (>115ms). Moderately increased T2 (100ms<T2<115ms) was found in all cases of hippocampal non-specific gliosis and HS (histopathologically confirmed), hence it is not possible to distinguish these two pathologies by correlation methods. No changes in T2

values were found in HC in patients with non-lesional epilepsy which is in agreement with the MRI findings.

Among lesional epilepsy cases, two discrepancies between standard MRI and quantitative evaluation were found. Although MRI revealed no change in the left HC of the patient No.6, increased T2 values were observed and histology confirmed a hippocampal gliosis. Patient No.12 revealed increased T2 values in both HC, although radiologists reported only unilateral pathology.

Physiological changes of MR parameters in anteroposterior direction of HC complicate statistically relevant assessment of control intervals alongside the hippocampus. This dependence on voxel positioning represents a systematic error leading to a failure of standard statistical evaluations in hippocampal regions. As the CORIMA program enables reciprocally highlight pixels corresponding to control data, we needed to find the best threshold for semi-automatic assessment of hippocampal involvement. Several tests on the control group empirically proved (data not shown) that the mean values±standard deviations represented the best thresholds. As the thresholds were determined empirically, small number of values exceeding the control interval of corresponding MR parameters may occur also in the data sets of the control group (see Figure 5.2). These values did not exceed the control interval by more than 5% in T2 values and metabolic concentration; however, MD values in the vicinity of the brain stem may exceed the MAX value by more than 20%. Inclusion or exclusion of high MD values in the vicinity of the brain stem from the volunteers' statistics strongly affects the control interval and therefore may underestimate or overestimate the pathology extent in patients (see Electronic Supplementary Material 3 in Manuscript enclosed in Appendix 3). The analysis alongside the diffusion distortions may lead to the failure of the semi-automatic MRS-MD assessment.

The combination of Cr, NAA, Cho and their ratios with T2 assessed the epileptic zone in all cases identically with the electro-clinical diagnosis whereas the lateralisation based on EEG only may differ. The comparison emphasises the significance of quantitative MR parameter analysis for confirmation of lateralisation in ambiguous cases.

7 Conclusions

Progress in MR techniques and computer technology has enabled new possibilities in the examination of human brain pathologies and has revealed that a combination of different diagnostic methods may provide more precise information of the nature and extent of a pathology. In particular, a combination of MRSI, DWI, perfusion and T1 or T2 relaxation measurements is very promising, since they provide complementary pieces of information. However, patient outcomes after neurosurgeries have shown that qualitative image evaluation is not always precise enough in the assessment of pathology extent. Therefore, it is necessary to search for more sophisticated methods. At present, no study has involved diffusion, relaxation, spectroscopic and histological data based on a pixel-by-pixel image processing at 3T in individual patients. Therefore, the aim of this thesis was to develop a new quantitative method combining these image modalities and to perform a prospective quantitative MR study of patients suffering from brain tumours and temporal lobe epilepsy to validate these techniques and to demonstrate their potential use in the clinical routine.

The CORIMA program has been developed to enable studying of mutual relationships between different MR parameters based on quantitative pixel-by-pixel image evaluation. The program has been used in two different studies, the study of patients with human brain tumour and the study concerning to drug-resistant temporal lobe epilepsy. The experience with the program shows that it is valuable for tissue differentiation and assessment of pathology extent using automatic identification of pixels corresponding to healthy controls. However, the current version programmed in MATLAB is useful only for 2D data evaluation as the processing rate of huge amount of 3D spectroscopic data has been found unacceptable in the clinical routine.

This study summarises the MR parameters as metabolite levels, diffusion coefficients and relaxation times in different tumour and tissue types. It proves that a combination of different MR parameters based on pixel-by-pixel image analysis and their correlations in individual patients may help in better identification of the tumour type, examination of the tumour extent, direction of proliferation and also in better understanding of the biochemical processes inside the tumour. The origin of special correlation patterns found in each tumour type is based on the different tissue states involved in an examined area, i.e. healthy tissue, tissue infiltrated by tumourous cells, active, tumour infiltrated oedema,

oedema, etc. The positive linear MD-T2 correlation was found in LGG, enhancing HGG and LYM, but not in non-enhancing HGG. Recurrent tumours exhibit the same correlation patterns as untreated ones, but with changed metabolic values caused by chemo/radiotherapy. Metabolic values do not correlate with MD and T2 in the tissue with radiation changes only. Correlations of the following MR parameters are suitable for tissue differentiation: MD, T2, Cho, N-acetylaspartate, creatine, myo-inositol, lactate, macromolecules and lipids and metabolite ratios.

Standard voxel-based evaluation of MRSI data has been found suitable for differential diagnosis between tumour recurrence and radiation necrosis. The MRSI diagnosis assessed mainly on the evaluation of Cho/Cr level was in agreement with the final diagnosis in 88 % of cases. MRSI-navigated stereotactic or open-frame biopsies have been successfully implemented into the neurooncological navigated systems and the developed procedure is used in the clinical practice at present.

This study further proves that the description of extent and character of hippocampal pathology in patients with drug-resistant temporal lobe epilepsy can be substantially improved by a detailed analysis of multiple MR parameters. Mutual relationships between studied parameters in the hippocampus revealed gradual changes in individual parameters in the anteroposterior direction of the hippocampus providing additional information about spatial distribution of these parameters across the hippocampus. Correlations with different slopes (positive, negative or no correlations) were recognised. The slope provides information about the significance of metabolic or structural changes. The correlations with relaxation times were found more accurate for assessment of hippocampal involvement, especially because of distortions in diffusion images. Correlations of the following MR parameters are suitable for correct EZ lateralisation: T2, Cho/NAA, Cr/NAA, Cr/Cho, Cho and NAA. This study confirmed the value of combining different neuroimaging methods in surgical planning in cases with an inconsistent EZ lateralisation.

Although the technique can be used only in the semiautomatic mode due to an unavoidable chemical shift artefact in MRSI and image distortions in DTI, we proved that the combination of different MR parameters is able to describe the complexity of a highly heterogeneous tissue in various pathologies and in their vicinity.

8 List of Publications

8.1 Publications and Manuscripts the Thesis Is Based on

1. **Wagnerova D**, Herynek V, Malucelli A, Dezortova M, Vymazal J, Urgosik D, Syrucek M, Jiru F, Skoch A, Bartos R, Sames M, Hajek M. Quantitative MR imaging and spectroscopy of brain tumours: a step forward? Eur Radiol 2012; 22(11):2307-2318. IF2011: 3.222
2. **Wagnerova D**, Jiru F, Dezortova M, Vargova L, Sykova E, Hajek M. The correlation between 1H MRS Choline concentrations and MR diffusion trace values in human brain tumours, Magn Reson Mater Phy 2009; 22(1):19-31. IF: 1.859
3. **Wagnerová D**, Urgošík D, Syrůček M, Hájek M. Využití kombinace metod magnetické rezonance pro diagnostiku tumourů, Cesk Slov Neurol N 2011;74/107(2):150-156. IF: 0.279
4. **Wagnerová D**, Herynek V, Dezortová M, Marusič P, Kršek P, Zámečník J, Jírů F, Škoch A, Hájek M. The use of correlations between quantitative MR parameters for assessment of hippocampal involvement in temporal lobe epilepsy. Submitted to Eur Radiol.

8.2 Other Publications

1. Herynek V, **Wagnerova D**, Hejlova I, Dezortova M, Hajek M. Changes in the brain during long-term follow-up after liver transplantation. J Magn Reson Imaging 2012; 35:1332-1337. IF2011: 2.698
2. Hajek M, Dezortova M, **Wagnerova D**, Skoch A, Voska L, Hejlova I, Trunecka P. MR spectroscopy as a tool for in vivo determination of steatosis in liver transplant recipients. Magn Reson Mater Phy 2011;24(5):297-304. IF2011: 1.883
3. Hájek M, Dezortová M, **Wagnerová D**, Voska L, Hejlová I, Trunečka P. Stanovení obsahu jaterního tuku metodou 1H MR spektroskopie. Čas Lék čes 2011; 150:68-71
4. Saudek E, Novak D, **Wagnerova D**, Hajek M. Analysis of Human Brain NMR Spectra in Vivo Using Artificial Neural Networks, Lect Notes Comp Sc 2008; 5164:517-526

Total IF: 9.941

9 References

[1] Edelman RR, Hesselink JR, Zlatkin MB. Clinical magnetic resonance imaging. W.B. Saunders Company 1996.

[2] Wagnerova D, Jiru F, Dezortova M, Vargova L, Sykova E, Hajek M. The correlation between 1H MRS choline concentrations and MR diffusion trace values in human brain tumours. Magn Reson Mater Phy 2009; 22(1):19-31.

[3] Khayal IS, Ceawford FW, Saraswathy S, Lamborn KR, Chany SM, Cha S, McKnight TR, Nelson SJ. Relationship between choline and apparent diffusion coefficient in patients with gliomas. J Magn Reson Imaging 2008; 27:718–725.

[4] Oh J, Cha S, Aiken AH, Han ET, Crane JC, Stainsby JA, Wright GA, Dillon WP, Nelson SJ. Quantitative apparent diffusion coefficients and T2 relaxation times in characterising contrast enhancing brain tumours and regions of peritumoural oedema. J Magn Reson Imaging 2005; 21(6):701-708.

[5] Yang D, Korogi Y, Sugahara T, Kitajima M, Shigematsu Y, Liang L, Ushio Y, Takahashi M. Cerebral gliomas: prospective comparison of multivoxel 2D chemical-shift imaging proton MR spectroscopy, echoplanar perfusion and diffusion-weighted MRI. Neuroradiology 2002; 44:656–666.

[6] Jiru F. Doctoral Thesis. 1.LF UK, Praha, 2006.

[7] Klose U. Measurement sequences for single voxel proton MR spectroscopy. Eur J Radiol 2008; 67(2):194-201.

[8] Klose U, Jiru F: Principles of MR Spectroscopy and Chemical Shift Imaging. In: Advanced Image Processing in Magnetic Resonance Imaging. Edited by Luigi Landini. CRC Press, 2005.

[9] Posse S, Schuknecht B, Smith ME, van Zijl PC, Herschkowitz N and Moonen CT. Short echo time proton MR spectroscopic imaging. J Comput Assist Tomogr 1993; 17:1-14.

[10] Duyn JH, Gillen J, Sobering G, van Zijl PC, Moonen CT: Multisection Proton MR Spectroscopy Imaging of the Brain. Radiology 1993; 188:277-282.

[11] de Graaf RA. In vivo NMR spectroscopy: Principles and techniques. John Wiley & Sons, Chichester, 1998

[12] Jiru F. Introduction to post-processing techniques. Eur J Radiol 2008; 67(2): 202-217.

[13] Bracewill R. The Fourier Transform and its Applications. McGraw-Hill, New York, 1978.

[14] Prowencher SW. Estimation of metabolite concentrations from localised in vivo proton NMR spectra. Magn Reson Med 1993; 30(6):672-679.

[15] Available via http://www.sites.google.com/site/jsiprotool/

[16] Hajek M, Dezortova M. Introduction to clinical in vivo MR spectroscopy. Eur J Radiol 2008; 67(2):185-193.

[17] Chang L, Mc Bride D, Miller BL, Cornford M, Booth RA, Buchthal SD, Ernst TM, Jenden D. Localised in vivo 1H magnetic resonance spectroscopy and in vitro analyses of heterogeneous brain tumours. J Neuroimaging 1995; 5:157–163.

[18] Miller BL, Chang L, Booth R, Ernst T, Cornford M, Nikas D, McBrideD, JendenDJ. In vivo 1HMRS choline: correlation with in vitro chemistry/histology. Life Sci 1996; 58:1929–1935.

[19] Wagnerova D, Urgosik D, Syrucek M, Hajek M. Using a combination of magnetic resonance techniques for tumour diagnosis. Cesk Slov Neurol N 2011; 74/107(2):150-156.

[20] Beaulieu Ch. The basis of anisotropic water diffusion in the nervous system – a technical review. NMR Biomed 2002; 15:435-455.

[21] Stejskal EO, Tanner JE. Spin diffusion measurements: spin echoes in the presence of a time-dependent field gradient. J Chem Phys 1965; 42:288-292.

[22] O'Donnel L, Haker S, Westin CF. image Processing of Diffusion Tensor MRI data. In: Advanced Image Processing in Magnetic Resonance Imaging. Edited by Luigi Landini. CRC Press, 2005.

[23] Ibrahim I. Doctoral Thesis. 1.LF UK, Praha, 2012.

[24] Latour LL, Svoboda K, Mitra PP, Sotak CH. Time-dependent diffusion of water in a biological model system. Proc Natl Acad Sci U S A. 1994; 91(4):1229-33.

[25] Timothy PL, Roberts TP, Schwartz ES. Principles and implementation of diffusion-weighted and diffusion tensor imaging. Pediatr Radiol. 2007; 37(8):739-48.

[26] Pierpaoli C, Jezzard P, Basser PJ, Barnett A, Di Chiro G. Diffusion tensor MR imaging of the human brain. Radiology 1996; 201(3):637-48.

[27] Melhem ER, Mori S, Mukundan G, Kraut MA, Pomper MG, van Zijl PCM. Diffusion Tenzor MR Imaging of the Brain and White Matter Tractography. AJR Am J Roentgenol 2002; 178(1):3-16.

[28] Nitz WR. MR imaging: acronyms and clinical application. Eur Radiol 1999; 9:979-997.

[29] Jezzard P, Balaban RS. Correction for geometric distortion in echo planar images from Bo field variations. Magn. Reson. Med. 1995; 34: 65–73.

[30] Bodammer N, Kaufmann J, Kanowski M, Tempelmann C. Eddy current correction in diffusion-weighted imaging using pairs of images acquired with opposite diffusion gradient polarity. Magn Reson Med. 2004; 51(1):188-93.

[31] Available via http://www.fmrib.ox.ac.uk/fsl/

[32] Levitt MH. Spin dynamics: Basics of Nuclear Magnetic Resonance. John Wiley& Sons, Chichester, 2001.

[33] Meiboom S, Gill D. Modified spin-echo method for measuring nuclear relaxation times. Rev Sci Instr 1958; 29(8):688-691.

[34] MacFall JR, Wehrli FW, Breger RK, Johnson GA. Methodology for the measurement and analysis of relaxation times in proton imaging. Magn Reson Imaging 1987; 5:209-220.

[35] Herynek V, Wagnerová D, Hejlová I, Dezortová M, Hájek M. Changes in the brain during long-term follow-up after liver transplantation. J Magn Reson Imaging 2012; 35:1332-1337.

[36] Kohler BA, Ward E, McCarthy BJ, Schymura MJ, Ries LAG, Eheman Ch, Jemal A, Anderson RN, Ajani UA, Edwards BK. Annual Report to the Nation on the Status of Cancer, 1975–2007, Featuring Tumours of the Brain and Other Nervous System. J Natl Cancer Inst 2011; 103(9): 714–736.

[37] Gupta RK, Sinha U, Cloughesy TF, Alger JR. Inverse correlation between choline magnetic resonance spectroscopy signal intensity and the apparent diffusion coefficient in human glioma. Magn Reson Med 1999; 41:2–7.

[38] Kaba SE, Kyritsis AP. Recognition andmanagement of gliomas. Drugs 1997; 53:235–244.

[39] Di Costanzo A, Scarabino T, Trojsi F, Popolizio T, Catapano D, Giannatempo GM, Bonavita S, Portaluri M, Tosetti M, d'Angelo VA, Salvolini U, Tedeschi G. Proton MR spectroscopy of cerebral gliomas at 3 T: spatial heterogeneity, and tumour grade and extent. Eur Radiol 2008; 18(8):1727-1735.

[40] Sibtain NA, Howe FA, Saunders DE. The clinical value of proton magnetic resonance spectroscopy in adult brain tumours. Clin Radiol 2007; 62(2):109-119.

[41] Stadlbauer A, Gruber S, Nimsky C, Fahlbusch R, Hammen T, Buslei R, Tomandl B, Moser E, Ganslandt O. Preoperative grading of gliomas by using metabolite quantification with high-spatial-resolution proton MR spectroscopic imaging. Radiology 2006; 238(3):958-969.

[42] Majos C, Alonso J, Aguilera C, Serrallonga M, Perez-Martin J, Acebes JJ, Arus C, Gili J. Proton magnetic resonance spectroscopy ((1)H MRS) of human brain tumours: assessment of differences between tumour types and its applicability in brain tumour categorization. Eur Radiol 2003; 13(3):582-591.
[43] Howe FA, Barton SJ, Cudlip SA, Stubbs M, Saunders DE, Murphy M, Wilkins P, Opstad KS, Doyle VL, McLean MA, Bell BA, Griffiths JR. Metabolic profiles of human brain tumours using quantitative in vivo 1H magnetic resonance spectroscopy. Magn Reson Med 2003; 49(2):223-232.
[44] Isobe T, Matsumura A, Anno I, Yoshizawa T, Nagatomo Y, Itai Y, Nose T. Quantification of cerebral metabolites in glioma patients with proton MR spectroscopy using T2 relaxation time correction. Magn Reson Imaging 2002; 20(4):343-349.
[45] Sijens PE, Oudkerk M. 1H chemical shift imaging characterisation of human brain tumour and oedema. Eur Radiol 2002; 12(8):2056-2061.
[46] Fan G, Sun B, Wu Z, Guo Q, Guo Y. In vivo single-voxel proton MR spectroscopy in the differentiation of high-grade gliomas and solitary metastases. Clin Radiol 2004; 59(1):77-85.
[47] Chernov MF, Muragaki Y, Ochiai T, Taira T, Ono Y, Usukura M, Maruyama T, Nakaya K, Nakamura R, Iseki H, Kubo O, Hori T, Takakura K. Spectroscopy-supported frame-based image-guided stereotactic biopsy of parenchymal brain lesions: comparative evaluation of diagnostic yield and diagnostic accuracy. Clin Neurol Neurosurg 2009; 111(6):527-535.
[48] Guillevin R, Menuel C, Duffau H, Kujas M, Capelle L, Aubert A, Taillibert S, Idbaih A, Pallud J, Demarco G, Costalat R, Hoang-Xuan K, Chiras J, Vallée JN. Proton magnetic resonance spectroscopy predicts proliferative activity in diffuse low-grade gliomas. J Neurooncol 2008; 87(2):181-187.
[49] McKnight TR, Lamborn KR, Love TD, Berger MS, Chang S, Dillon WP, Bollen A, Nelson SJ. Correlation of magnetic resonance spectroscopic and growth characteristics within Grades II and III gliomas. J Neurosurg 2007; 106(4):660-666.
[50] Howe FA, Opstad KS. 1H MR spectroscopy of brain tumours and massess. NMR Biomed 2003; 16(3):123-131.
[51] Rollin N, Guyotat J, Streichenberger N, Honnorat J, Tran Minh VA, Cotton F. Clinical relevance of diffusion and perfusion magnetic resonance imaging in assessing intra-axial brain tumours. Neuroradiology 2006; 48(3):150-159.

[52] Krabbe K, Gideon P, Wagn P, Hansen U, Thomsen C, Madsen F. MR diffusion imaging of human intracranial tumours. Neuroradiology 1997; 39(7):483-489.
[53] Fenrich FRE, Beaulieu C, Allen PS. Relaxation times and microstructures. NMR Biomed 2001; 14:133-139.
[54] Wright AJ, Fellows G, Byrnes TJ, Opstad KS, McIntyre DJ, Griffiths JR, Bell BA, Clark CA, Barrick TR, Howe FA. Pattern recognition of MRSI data shows regions of glioma growth that agree with DTI markers of brain tumour infiltration. Magn Reson Med 2009; 62(6):1646-1651.
[55] Rock JP, Scarpace L, Hearshen D, Gutierrez J, Fisher JL, Rosenblum M, Mikkelsen T. Associations among magnetic resonance spectroscopy, apparent diffusion coefficients, and image-guided histopathology with special attention to radiation necrosis. Neurosurgery 2004; 54(5):1111-1117.
[56] Catalaa I, Henry R, Dillon WP, Graves EE, McKnight TR, Lu Y, Vigneron DB, Nelson SJ. Perfusion, diffusion and spectroscopy values in newly diagnosed cerebral gliomas. NMR Biomed 2006; 19:463-475.
[57] Zonari P, Baraldi P, Crisi G. Multimodal MRI in the characterisation of glial neoplasms: the combined role of single-voxel MR spectroscopy, diffusion imaging and echo-planar perfusion imaging. Neuroradiology 2007; 49(10):795-803.
[58] Calvar JA, Meli FJ, Romero C, Calcagno ML, Yánez P, Martinez AR, Lambre H, Taratuto AL, Sevlever G. Characterisation of brain tumours by MRS, DWI and Ki-67 labeling index. J Neurooncol 2005; 72(3):273-780.
[59] Bobek-Billewicz B, Stasik-Pres G, Majchrzak H, Zarudzki L. Differentiation between brain tumour recurrence and radiation injury using perfusion, diffusion-weighted imaging and MR spectroscopy. Folia Neuropathol 2010; 48(2):81-92.
[60] Stupp R, Mason WP, van den Bent MJ, et al. Radiotherapy plus Concomitant and Adjuvant Temozolomide for Glioblastoma. N Engl J Med 2005; 352:987-996.
[61] Brandsma D, Stalpers L, Taal W, Sminia P, van der Bent MJ. Clinical features, mechanisms, and management of pseudoprogression in malignant gliomas. Lancet Oncol 2008; 9: 453-461.
[62] Tofilon PJ, Fike JR. The radioresponse of the central nervous system: a dynamic process. Radiat Res 2000; 153: 357-370.

[63] Siu A, Wind JJ, Iorgulescu JB, Chan TA, Yamada Y, Sherman JH. Radiation necrosis following treatment of high grade glioma - a review of the literature and current understanding. Acta Neurochir 2012; 154:191-201.
[64] Smith EA, Carlos RC, Junck LR, Tsien CI, Elias A, Sundgren PC. Developing a clinical decision model: MR spectroscopy to differentiate between recurrent tumour and radiation change in patients with new contrast-enhancing lesions. AJR Am J Roentgenol 2009; 192(2):W45-52.
[65] Chernov MF, Hayashi M, Izawa M, Usukura M, Yoshida S, Ono Y, Muragaki Y, Kubo O, Hori T, Takakura K. Multivoxel proton MRS for differentiation of radiation-induced necrosis and tumour recurrence after gamma knife radiosurgery for brain metastases. Brain Tumour Pathol 2006; 23(1):19-27.
[66] Rock JP, Hearshen D, Scarpace L, Croteau D, Gutierrez J, Fisher JL, Rosenblum ML, Mikkelsen T. Correlations between magnetic resonance spectroscopy and image-guided histopathology, with special attention to radiation necrosis. Neurosurgery 2002; 51(4):912-9.
[67] Graves EE, Nelson SJ, Vigneron DB, Verhey L, McDermott M, Larson D, Chang S, Prados MD, Dillon WP. Serial proton MR spectroscopic imaging of recurrent malignant gliomas after gamma knife radiosurgery. AJNR Am J Neuroradiol 2001; 22(4):613-24.
[68] Kamada K, Houkin K, Abe H, Sawamura Y, Kashiwaba T. Differentiation of cerebral radiation necrosis from tumour recurrence by proton magnetic resonance spectroscopy. Neurol Med Chir 1997; 37(3):250-256.
[69] Hein PA, Eskey CJ, Dunn JF, Hug EB. Diffusion-Weighted Imaging in the Follow-up of Treated High-Grade Gliomas: Tumour Recurrence versus Radiation Injury. AJNR Am J Neuroradiol 2004; 25:201 -209.
[70] Kashimura H, Inoue T, Beppu T, Ogasawara K, Ogawa A. Diffusion tensor imaging for differentiation of recurrent brain tumour and radiation necrosis after radiotherapy --Three case reports. Clin Neuro Neurosurg 2007; 109:106 -110.
[71] Sundgren PC, Fan X, Weybright P, Welsh RC, et al. Differentiation of recurrent brain tumour versus radiation injury using diffusion tensor imaging in patients with new contrast-enhancing lesions. Magn Res Ima 2006; 24:1131-1142.
[72] Dowling C, Bollen AW, Noworolski SM, et al. Preoperative Proton MR Spectroscopic Imaging of Brain Tumours: Correlation with Histopathologic Analysis of Resection Specimens. AJNR Am J Neuroradiol 2001; 22:604-612.

[73] Cersosimo R, Flesler S, Bartuluchi M, Soprano AM, Pomata H, Caraballo R. Mesial temporal lobe epilepsy with hippocampal sclerosis: Study of 42 children. Eur J Epilepsy. 2011; 20(2):131–137.
[74] Engel J Jr. Introduction to temporal lobe epilepsy. Epilepsy Res 1996; 26:141-150.
[75] Ray A, Kotagal P. Temporal lobe epilepsy in children: overview of clinical semiology. Epileptic Disord 2005; 7(4):299-307.
[76] Margerison JH, Corsellis JAN. Epilepsy and the temporal lobe. A clinical, electroencephalographic and neuropathological study of the brain in epilepsy, with particular reference to the temporal lobes. Brain 1966; 89:499-530.
[77] Kuzniecky R, Palmer Ch, Hugg J, Martin R, Sawrie S, Morawetz R, Faught E, Knowlton R. Magnetic resonance spectroscopic imaging in temporal lobe epilepsy: Neuronal dysfunction or cell loss?. Arch Neurol 2001; 58:2048-2053.
[78] Bonilha L, Edwards JC, Kinsman SL, Morgan PS, Fridriksson J, Rorden Ch, Rumboldt Zoran, Roberts DR, Eckert MA, Halford JJ. Extrahippocampal gray matter loss and hippocampal deafferentation in patients with temporal lobe epilepsy. Epilepsia 2010; 51(4):519-528.
[79] Wiebe S, Blume WT, Girvin JP, Eliasziw M; Effectiveness and Efficiency of Surgery for Temporal Lobe Epilepsy Study Group. A randomized, controlled trial of surgery for temporal-lobe epilepsy. N Engl J Med 2001; 345(5):311-318.
[80] Berkovic SF, McIntosh AM, Kalnins RM, Jackson GD, Fabinyi GCA, Brazenor GA, Bladin PF, Hopper JL. Preoperative MRI predicts outcome of temporal lobectomy. Neurology 1995; 45(7):1358-1363.
[81] Duzel E, Kaufmann J, Guderian S, Szentkuti A, Schott B, Bodammer N, Hopf M, Kanowski M, Tempelmann C, Heinze J. Measures of hippocampal volumes, diffusion and 1H MRS metabolic abnormalities in temporal lobe epilepsy provide partially complementary information. European Journal of Neurology 2004; 11:195-205.
[82] Keller SS, Roberts N. Voxel-based morphometry of temporal lobe epilepsy: an introduction and review of the literature. Epilepsia 2008; 49:741-757.
[83] Focke NK, Zogarajah M, Bonelli SB, Bartlett PA, Symms MR, Duncan JS. Voxel-based diffusion tensor imaging in patients with mesial temporal lobe epilepsy and hippocampal sclerosis. NeuroImage 2008; 40:728-737.

[84] Bonilha L, Kobayashi E, Rorden C, Cendes F, Li LM. Medial temporal lobe atrophy in patients with refractory temporal lobe epilepsy. J Neurol Neurosurg Psychiatry 2003; 74:1627-1630.

[85] Pereira PMG, Oliveira E, Rosado P. Apparent diffusion coefficient mapping of the hippocampus and the amygdala in pharmacoresistant temporal lobe epilepsy. AJNR Am J Neuroradiol 2006; 27:671-683.

[86] Ellmore TM, Pieters TA, Tandon N. Dissociation between diffusion MR tractography density and strength in epilepsy patients with hippocampal sclerosis. Epilepsy Res 2011; 93(2-3):197-203.

[87] Concha L, Beaulieu C, Collins DL, Gross DW. White-matter diffusion abnormalities in temporal-lobe epilepsy with and without mesial temporal sclerosis. J Neurol Neurosurg Psychiatry 2009; 80(3):312-319.

[88] Assaf BA, Mohamed FB, Abou-Khaled KJ, Williams JM, Yazeji MS, Haselgrove J, Faro SH. Diffusion tensor imaging of the hippocampal formation in temporal lobe epilepsy. AJNR Am J Neuroradiol 2003; 24:1857-1862.

[89] Knake S, Salat DH, Halgren E, Halko MA, Greve DN, Grant PE. Chaneges in the white matter microstructure in patients with TLE and hippocampal sclerosis. Epileptic Disord 2009;11(3):244-50

[90] Salmenpera TM, Symms MR, Boulby PA, Barker GJ, Duncan JS. Postictal diffusion-weighted imaging. Epilepsy Res 2006; 70(2-3):133-143.

[91] Jackson GD, Connelly A, Duncan JS, Grunewald RA, Gadian DG. Detection of hippocampal pathology in intractable partial epilepsy. Increased sensitivity with quantitative magnetic resonance T2 relaxometry. Neurology 1993; 43:1793-1799.

[92] Jack CR. Hippocampal T2 relaxometry in epilepsy: past, present, and future. AJNR Am J Neuroradiol 1996; 17:1811-1914.

[93] von Oertzen J, Urbach H, Blumcke I, Reuber M, Traber F, Peveling T, Menzel C, Elger CE. Time-efficient T2 relaxometry of the entire hippocampus is feasible in temporal lobe epilepsy. Neurology 2002; 58:257-264.

[94] Barlett PA, Symms MR, Free SL, Duncan JS. T2 relaxometry of the hippocampus at 3T. AJNR 2007; 28:1095-1098.

[95] Hajek M, Dezortova M, Krsek P. 1H MR spectroscopy in epilepsy. Eur J Radiol 2008;67(2):258-267.

[96] Hajek M, Krsek P, Dezortova M, Marusic P, Zamecnik J, Kyncl M et al. 1H MR spectroscopy in histopathological subgroups of mesial temporal lobe epilepsy. Eur Radiol 2009; 19(2): 400–408.

[97] Hugg JW, Kuzniecky RI, Gilliam FG, Morawetz RB, Faught RE, Hetherington HP. Normalisation of contralateral metabolic function following temporal lobectomy demonstrated by 1H magnetic resonance spectroscopic imaging. Ann Neurol 1996; 40:236-239.

[98] Simister RJ, McLean MA, Barker GJ, Duncan JS. Proton MR spectroscopy of metabolite concentrations in temporal lobe epilepsy and effect of temporal lobe resection. Epilepsy Research 2009; 83:168-176.

[99] Cendes F, Andermann F, Dubeau F, Matthews PM, Arnold DL. Normalisation of neuronal metabolic dysfunction after surgery for temporal lobe epilepsy. Evidence from proton MR spectroscopic imaging. Neurology 1997; 49:1525-1533.

[100] Kuzniecky R, Hugg J, Hetherington H, Martin R, Faught E, Morawetz R, Gilliam F. Predictive value of 1H MRSI for outcome in temporal lobectomy. Neurology 1999; 53(4):694-698.

[101] Kantarci K, Shin C, Britton JW, So EL, Cascino GD, Jack Jr CR. Comparative diagnostic utility of 1H MRS and DWI in evaluation of temporal lobe epilepsy. Neurology 2002; 58(12):1745-1753.

[102] Namer IJ, Bolo NR, Sellal F, Nguyen VH, Nedelec JF, Hirsch E, Marescaux C. Combined measurements of hippocampal N-acetyl-aspartate and T2 relaxation times in the evaluation of mesial temporal lobe epilepsy: correlation with clinical severity and memory performances. Epilepsia 1999; 40(10):1424-1432.

[103] Jiru F, Skoch A, Hajek M (2003) LCModel for quantitative single voxel spectroscopy and spectroscopic imaging: a comparison. Magn Reson Mater Phy 16:S211.

[104] Palmini A, Najm I, Avanzini G, Babb T, Guerrini R, Foldvary-Schaefer N, Jackson G, Luders HO, Prayson R, Spreafico R, Vinters HV. Terminology and classification of the cortical dysplasias. Neurology 2004; 62:S2-8.

[105] Wagnerova D. Master Thesis. MFF UK, Praha, 2007.

[106] Wagnerova D, Herynek V, Malucelli A, Dezortova M, Vymazal J, Urgosik D, Syrucek M, Jiru F, Skoch A, Bartos R, Sames M, Hajek M. Quantitative MR imaging and spectroscopy of brain tumours: a step forward? Eur Radiol 2012; 22(11):2307-2318.

[107] Jiru F, Skoch A, Klose U, Grodd W, Hajek M. Error images for spectroscopic imaging by LCModel using Cramer-Rao bounds. Magn Reson Mater Phy 2006; 19(1):1-14.
[108] Irwan R, Sijens PE, Potze JH, Oudkerk M Correlation of proton MR spectroscopy and diffusion tensor imaging. J Magn Reson Imaging 2005; 23:851–858.
[109] Weis J, Ring P, Olofsson T, Ortiz-Nieto F, Wikström J. Short echo time MR spectroscopy of brain tumours: grading of cerebral gliomas by correlation analysis of normalised spectral amplitudes. J Magn Reson Imaging 2010; 31(1):39-45.
[110] Just M, Thelen M. Tissue characterisation with T1, T2 and proton density values: results in 160 patients with brain tumours. Radiology 1988; 169:779–785.
[111] Kono K, Inoue Y, Nakayama K, Shakudo M, Morino M, Ohata K, Wakasa K, Yamada R. The role of diffusion-weighted imaging in patients with brain tumours. AJNR Am J Neuroradiol 2001;22:1081–8.
[112] Eis M, Els T, Hoehn-Berlage M, Hossman KA. Quantitative diffusion MR imaging of cerebral tumour and oedema. Acta Neurochir 1994; 60:344–346.
[113] Muti M, Aprile I, Principi M, Italiani M, Guiducci A, Giulianelli G, Ottaviano P. Study on the variations of the apparent diffusion coefficient in areas of solid tumour in high grade gliomas. Magn Reson Imaging 2002; 20(9):635-641.
[114] Maeda M, Maier SE, Sakuma H, Ishida M, Takeda K. Apparent diffusion coefficient in malignant lymphoma and carcinoma involving cavernous sinus evaluated by line scan diffusion-weighted imaging. J Magn Reson Imaging 2006; 24(3):543-548.
[115] Guo AC, Cummings TJ, Dash RC, Provenzale JM. Lymphomas and high-grade astrocytomas: comparison of water diffusibility and histologic characteristics. Radiology 2002; 224:177–183.
[116] Bulakbasi N, Kocaoglu M, Ors F, Tayfun C, Ucoz T. Combination of single-voxel proton MR spectroscopy and apparent diffusion coefficient calculation in the evaluation of common brain tumours. AJNR Am J Neuroradiol 2003; 24(2):225-33.
[117] Offiah C, Hall E. Heroin-induced leukoencephalopathy: characterisation using MRI, diffusion-weighted imaging, and MR spectroscopy. Clin Radiol 2008; 63(2):146-152
[118] Kuzniecky R. Magnetic resonance spectroscopy in focal epilepsy: 31P and 1H spectroscopy. Rev Neurol 1999; 155:495–498.
[119] Vermathen P, Laxer KD, Matson GB, Weiner MW. Hippocampal structures: anteroposterior N-acetylaspartate differences in patients with epilepsy and control subjects as shown with proton MR spectroscopic imaging. Radiology 2000; 214:403-410.

[120] Chu WJ, Kuzniecky RI, Hugg JW, Abou-Khalil B, Gilliam F, Faught E, Hetherington HP. Statistically driven identification of focal metabolic abnormalities in temporal lobe epilepsy with corrections for tissue heterogeneity using 1H spectroscopic imaging. Magn Reson Med 2000; 43:359-367.
[121] Briellmann RS, Syngeniotis A, Fleming S, Kalnins RM, Abbott DF, Jackson GD. Increased anterior temporal lobe T2 times in cases of hippocampal sclerosis: A multi-echo T2 relaxometry study at 3 T. AJNR Am J Neuroradiol 2004; 25:389–394.

10 Appendix